DEFINING ANTECEDENT TOPOGRAPHY AT CORAL PINK SAND DUNES, KANE COUNTY, UTAH: THE INFLUENCE OF STRUCTURAL CONTROLS ON DUNE-FIELD BOUNDARY CONDITIONS AND HOLOCENE LANDSCAPE EVOLUTION

by

Elizabeth Janna Rozar

A thesis

submitted in partial fulfillment

of the requirements for the degree of

Master of Science in Geology

Boise State University

August 2015

BOISE STATE UNIVERSITY GRADUATE COLLEGE

DEFENSE COMMITTEE AND FINAL READING APPROVALS

of the thesis submitted by

Elizabeth Janna Rozar

Thesis Title: Defining Antecedent Topography at Coral Pink Sand Dunes, Kane County, Utah: The Influence of Structural Controls on Dune-Field Boundary Conditions and Holocene Landscape Evolution

Date of Final Oral Examination: 10 April 2015

The following individuals read and discussed the thesis submitted by student Elizabeth Janna Rozar, and they evaluated her presentation and response to questions during the final oral examination. They found that the student passed the final oral examination.

David E. Wilkins, Ph.D.	Chair, Supervisory Committee
John Bradford, Ph.D.	Member, Supervisory Committee
Nancy Glenn, Ph.D.	Member, Supervisory Committee
Richard L. Ford, Ph.D.	Member, Supervisory Committee

The final reading approval of the thesis was granted by David Wilkins, Ph.D., Chair of the Supervisory Committee. The thesis was approved for the Graduate College by John R. Pelton, Ph.D., Dean of the Graduate College.

DEDICATION

This thesis is dedicated to my grandfathers, George Coon and Luther Rozar, for their eternal, enthusiastic support of my education and adventures.

ACKNOWLEDGEMENTS

I am sincerely grateful to all the individuals who helped me in this endeavor. A special thanks to Dr. David Wilkins for his constant support and willingness to let me explore a research problem new to him and the department. This project would not have been possible without the technical support of TLS-master Lucas Spaete, GPR-genius John Bradford, and "R"-pro Robin Trayler. I also owe huge gratitude to my field crew: Claire Ostwald, Cody Black, Amy and Shiloh Cutter, Ian and Max Privette, and to committee member Dr. Rick Ford for his hospitality as well as his guidance in the field. Thank you to the Idaho National Laboratory for the loan of the TLS, to Coral Pink Sand Dunes State Park for the use of their OHV and camping facilities, and to the Boise State Department of Geosciences Burnham Grant and GSA Farouk El-Baz Student Research Award for helping to fund this work.

ABSTRACT

Dune fields are transient features that record climate signatures through changes in mobility, morphology, and patterning. Aeolian geomorphologists are increasingly recognizing the important role that pre-existing, antecedent topography plays in controlling boundary conditions that affect changes in dune patterning. However, the dynamic relationship between antecedent topography and climate-sensitive boundary conditions is relatively unexplored. Here, I define antecedent topography for the Coral Pink Sand Dunes in southern Utah and show that structural controls play an important role in shaping antecedent geomorphic conditions of this dune field. I use ground-based terrestrial laser scanning (TLS) to produce a high-resolution digital elevation model (DEM), which is used to extract the trend of underlying topography. This detrended model is used to identify areas within the dune field where there is a high potential for structural control of the underlying topography. I validate and further resolve this antecedent-topography model using ground-penetrating radar (GPR) to image the subsurface. Results show that CPSD has a complex and heterogeneous underlying topography, with variable structural influence, that affects dune morphology and patterning by creating variability in sediment supply, moisture gradients, and wind direction, and by confining the lateral extent of the dune field.

TABLE OF CONTENTS

LIST OF TABLES

LIST OF FIGURES

LIST OF ABBREVIATIONS

AGC	Automatic Gain Correction
ALSM	Airborne Laser Swath Mapping
ASTER GDEM	Advanced Spaceborne Thermal Emission and Reflection Radiometer Global Digital Elevation Model
BCAL	Boise Center Aerospace Laboratory
CPSD	Coral Pink Sand Dunes
GPS	Global Positioning System
LIA	Little Ice Age
LiDAR	Light Detection and Ranging
NED	National Elevation Dataset
NOAA	National Oceanic and Atmospheric Administration
OPUS	Online Positioning User Service
RTK	Real Time Kinetic
Sevier	Sevier Normal Fault
SRTM	Shuttle Radar Topography Mission
TLS	Terrestrial Laser Scanning
TZ	Transition Zone
USGS	United State Geological Survey

CHAPTER ONE: INTRODUCTION

1.1 Importance

Sand dunes are transient, climate-sensitive features that can serve as an effective tool for reconstructing paleoclimatic histories (Chase and Brewer, 2009; Barchyn and Hugenholtz, 2012; Thomas, 2013). Climate records preserved in dune sediments become especially important in continental arid to semi-arid environments where organic climate proxies are limited (Chase, 2009; Thomas, 2013). Recent advancements in optically stimulated luminescence (OSL) methods, used to date the burial of detrital sediments, have increased the value of dunes as a climate proxy by allowing more precise dating of aeolian landforms (Derickson et al., 2008; Ford et al., 2010; Ellwein et al., 2011; Lancaster and McCarley-Holder, 2013); however, dune response to climate change is a complex process, and understanding the meaning of these ages requires careful interpretation of paleo-landforms and the geomorphic processes and factors that shape them (Thomas and Wiggs, 2008; Chase, 2009; Thomas, 2013).

1.2 Dunes and Climate

Dunes have been recognized as predictable, self-organizing systems that are controlled primarily through internal, dune-dune interactions (Werner, 1995; Werner and Kocurek, 1999; Kocurek and Ewing, 2005). However, external boundary conditions, many of which are imposed by climate, influence this internal system in complex ways that result in the vast variety of morphologies and patterns seen in natural dune fields (Ewing and Kocurek, 2010; Barchyn and Hugenholtz, 2013; Thomas, 2013). Because

dunes are largely depositional landforms that accumulate over time, they record changes in erodibility and activity caused by changes in climate that have occurred since their inception (Thomas, 2013). These records are not necessarily recorded equally across the dune field, however, since variability arises where there are local differences in wind direction, vegetative cover, and moisture gradients (Ewing, 2009; Thomas, 2013). These heterogeneities can result in different dune morphologies and patterning that may respond differently to the same climate change event (Thomas, 2013).

Throughout their existence, dune fields may transition multiple times between an active and a stabilized state (Chase, 2009; Barchyn and Hugenholtz, 2012). Stabilization is typically characterized by increased vegetative cover, whereas reactivation occurs when aeolian transport capacity is increased due to changes in aridity, wind speed, or sediment availability (Barchyn and Hugenholtz, 2013). Many studies have linked dune activity to periods of drought (Ford et al., 2001; Forman et al., 2008; Wright et al., 2011). However, Chase (2009) shows that dune activity is not necessarily an indication of increased aridity, but instead reactivation of stabilized dunes can result from a variety of factors including disturbances due to fire, human activities, or biogenic processes (Barchyn and Hugenholtz, 2013). In addition to recording complex responses in the form of activity versus inactivity, dune forms also have the potential to record wind direction and thus give insight into past states of regional atmospheric circulation (Thomas, 2013).

1.3 Boundary Conditions

In addition to those imposed by climate, other boundary conditions can also affect dune types and patterning. For example, increased sediment supply is shown to facilitate the transition in form from barchans to crescentic ridges (Werner, 1995), and the

periodicity, intensity, and direction of wind regimes control dune forms such as star dunes (Ewing, 2009). All dune fields have at least two interacting boundary conditions — sediment supply and wind regime — but most patterns likely result from the interaction of multiple boundary conditions (Ewing, 2009). This interplay between boundary conditions throughout dune-field construction is relatively unexplored (Ewing and Kocurek, 2010).

In addition to accepted boundary conditions, newly recognized antecedent boundary conditions, such as areal limits, are being addressed (Ewing and Kocurek, 2010). Areal limits are defined by the geomorphic "container" in which the dune pattern develops, and are essentially equivalent to the antecedent topography of the basin in which the dunes are housed. These areal limits can also represent host dunes from a previous constructional period on which an active dune pattern formed (Ewing, 2009; Ewing and Kocurek, 2010). Ewing and Kocurek (2010) show that areal limits affect patterning by limiting dune-dune interactions that can occur in a given area, and that there is a strong correlation between dune-field area and dune-crest spacing and between dune-field width/length ratio and dune-crest spacing. These relationships indicate that small-scale dune fields (on the order of 10 km^2) are more affected by areal limits than are large-scale dune fields (10^2 km^2 – 10^6 km^2), and that maximum dune-crest spacing corresponds to a dune-field width to length ratio of 1:5. This relationship between dune-field dimensions and dune-crest spacing has implications for determining stages of dune-field evolution and whether or not a particular dune field has reached steady state.

1.4 Antecedent Topography

Antecedent topography is defined here as the topography present prior to a given period of dune formation (Ewing and Kocurek, 2010) and can include influences from erosional, structural, and depositional features. The Great Basin of the American Southwest contains many small-scale dune fields that formed after the last glacial maximum through aeolian reworking of sediments deposited in pluvial lakes (Jewell and Nicoll, 2011). Many of these dune fields form on these relatively flat, playa surfaces or at the lee side of broad valleys without significant topographic influence. However, even small topographic features in underlying bedrock or sedimentary substrate have been shown to affect dune types and patterning (Derickson et al., 2008; Ewing and Kocurek, 2010; Ewing, 2009) by causing local changes in wind direction (Yang et al., 2011) and the water table (Ewing and Kocurek, 2010; Bishop, 2013), which in turn affect sediment supply and vegetation potential. For example, Kocurek et al. (2007) show that the antecedent topography at White Sands National Monument in New Mexico contains subtle shoreline features of Lake Otero that control the elevation of the water table; this ultimately affects sediment supply and variability in dune spacing. In spite of these studies, the role of more complex, structurally controlled, antecedent topography has not been examined.

1.5 Research Hypothesis

This study seeks to define the antecedent topography, and specifically look for structural controls that influence this topography, at Coral Pink Sand Dunes (CPSD), a small-scale dune field in southern Utah. Previous studies of CPSD have established a late-Holocene climate chronology (Ford et al., 2010; Wilkins et al., 2005) for the dune

field; however, previous studies have not addressed the preexisting geomorphic state that existed prior to or during dune formation. The CPSD are located along the Sevier Normal Fault (Sevier), a steeply dipping normal fault that represents the eastern-most extent of Basin and Range extension. The structural complexity, related to the Sevier, of the bedrock underlying the dune field likely plays a large role in shaping the geomorphic nature of preexisting, antecedent topography.

This study seeks to test the hypothesis that the CPSD Lower Dune Field is housed in a structurally controlled graben, bounded by the Sevier scarp to the east and a series of antithetic faults to the west, and that these structural controls on antecedent topography create heterogeneity across the dune field that influences variability in dune patterning and morphology. Defining this antecedent condition allows a more informed interpretation of paleoclimate, and helps us to understand how preexisting geomorphic conditions affect boundary conditions that influence dune formation and patterning. My research questions include:

1. What does the antecedent topography on which the current period of dune activity formed look like and what is the influence of structural controls on this topography?
2. How does the antecedent topography and related geomorphic conditions vary across the dune field, and what is the effect of this variation on dune morphology?
3. How can understanding paleotopography contribute to our interpretation of paleoclimate and Holocene landscape evolution at the CPSD and along the western Colorado Plateau in general?

A second major goal of this research is to develop a cost-effective method for creating high-resolution digital-elevation models (DEMs) for small dune fields. Terrestrial laser scanning (TLS) is an active remote-sensing method that uses ground-based LiDAR (Light Detection and Ranging) to create georeferenced point clouds of the ground surface. Many studies have utilized airborne LiDAR (ASLM)-derived DEMs for dune-field-scale studies, but the use of TLS for studies of this scale has not been attempted. This study employs the use of TLS to create a high-resolution DEM in order to derive a detrended surface representing the underlying, antecedent topography.

In this research, I define and constrain antecedent topography using analysis of TLS-derived digital elevation models (DEMs) and ground-penetrating radar (GPR) geophysical techniques. I show that the antecedent topography at the CPSD includes both structurally controlled and erosional topographic features, as well as variable substrate characteristics. I propose that these features in the antecedent topography affect dune morphology and patterning by creating spatial variability in sediment supply, moisture gradients, and wind direction, and by confining the extent of the dune field. I use this new understanding of paleotopography to reinterpret paleoclimatic signals in the dune field and recommend future directions for paleoclimatic studies. I also put forward a new method for creating high-resolution DEMs for small dune fields in order to define a detrended underlying surface.

CHAPTER TWO: STUDY AREA BACKGROUND

2.1 Geography

The Coral Pink Sand Dunes dune field is located in southwestern Utah, just north of the Utah-Arizona state line and 17 km (10 miles) due west of the town of Kanab. The dune field is approximately 14 km^2 in area and can be divided into an Upper Dune Field and a Lower Dune Field (Figure 1). These two sections are approximately equal in size but are separated in elevation by offset of the Sevier Normal Fault (Sevier). The Lower Dune Field ranges in elevation from 1,730 m (5,676 ft.) at its southern most point to 1,880 m (6,168 ft.) at its northern termination against the Sevier Scarp, whereas the Upper Dune Field is relatively flat but decreases slightly in elevation from its southern reach at 1,930 m (6,332 ft.) to the northern limit of the dune field at 1,845 m (6,053 ft.). The Lower Dune Field is the primary focus of this research.

The Lower Dune Field is approximately 5 km in length by 1 km in width, and is oriented in a SW-NE direction (Figure 1). Interdune areas in the active core of the dune field are 10 to 40 meters lower in elevation than points on the edge of the dune field. On the eastern margin of the Lower Dune Field, the Sevier is present as a steep escarpment whose cliffs form the western boundary of the Moquith Mountains. The main drainage, Sand Wash, is an ephemeral stream at the base of the scarp that flows from north to south. In the northern part of the Lower Dune Field, Sand Wash is perched above the dune field, but as you move to the south it incises to below the level of adjacent interdune

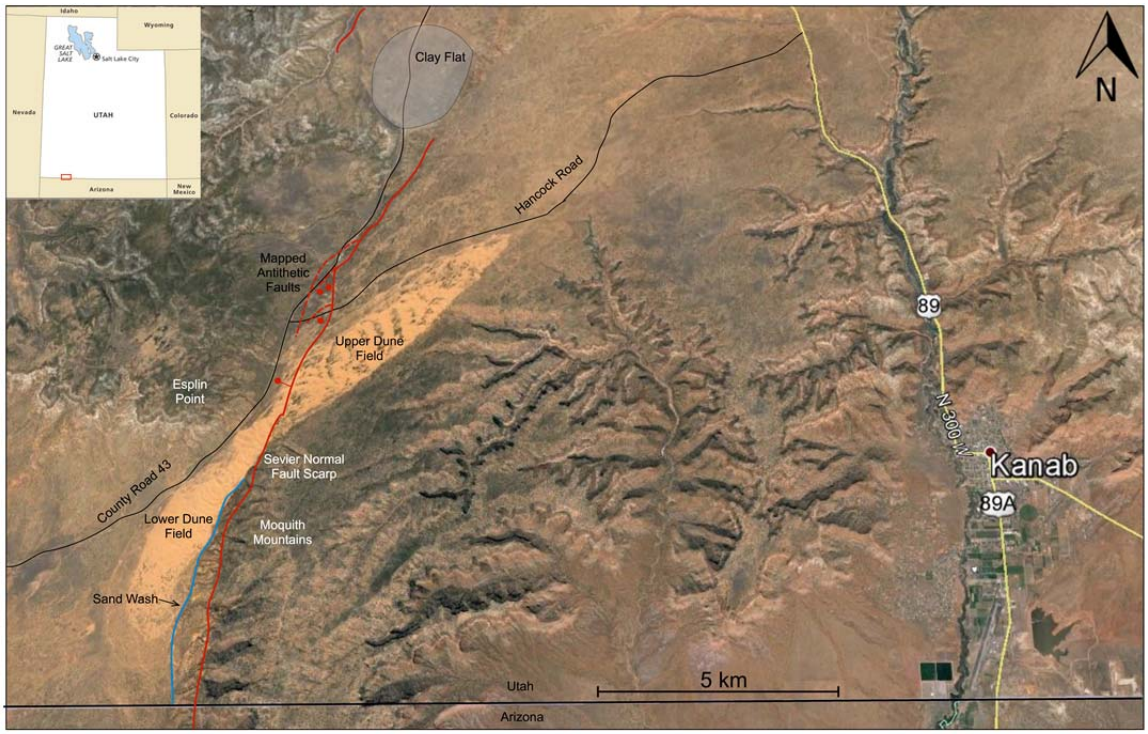

Figure 1: The Coral Pink Sand Dunes (CPSD) dune field is located in southern Utah, approximately 5 km north of the Utah-Arizona state line and 17 km west of the town of Kanab. The dune field is divided into an Upper Dune Field and a Lower Dune Field, separated by the Sevier Normal Fault (Sevier) scarp. The Lower Dune Field, the focus of this study, is approximately 5 km in length by 1 km in width and trends SW-NE. Ephemeral drainage occurs in Sand Wash along the eastern edge of the dune field at the base of the Sevier scarp. Several antithetic faults have been mapped just north of the dune field (Hayden, 2013). Clay Flat is a closed depositional basin located north of the dune field where there is a left step in the Sevier (Lund et al., 2008).

areas. The wash is fed from the east by several steep bedrock canyons that drain the Sevier escarpment. To the west of the Lower Dune Field is the prominent sandstone mesa, Esplin Point. The Lower Dune Field is contained primarily within the boundary of Coral Pink Sand Dunes State Park, and is accessed from its west side via Coral Pink Sand Dunes Road (Kane County Road 43). The state park is a popular destination for OHV (off highway vehicle) recreationists, and has facilities including a campground, visitor's center, viewing deck, and interpretive trails.

2.2 Geology

2.2.1 Bedrock Geology

The bedrock underlying and surrounding the CPSD, as with much of the Colorado Plateau province, is composed primarily of Triassic to Jurassic sandstone and limestone (Figure 2). Formations important to this research are described below.

2.2.1.1 Navajo Sandstone

The most prevalent unit that outcrops in and around the dune field is the Lower Jurassic-aged Navajo Sandstone (Figure 2A), a well-sorted quartz sandstone that formed in a large inland desert (Kocurek, 2003). The sandstone is massively cross-bedded and transitions to more thinly bedded sandstone and siltstone at its lower contact. Based on the most current geologic map by Hayden (2013), this unit underlies the entire Lower Dune Field. The Navajo Formation can be divided into three subunits of roughly equal thickness. The lowest part of the formation is the "brown" cliff-forming sandstone that caps the Moquith Mountains to the east of the dune field. The middle "pale red" sandstone is a slope-forming rock that is mostly covered by Quaternary aeolian deposits. The uppermost unit is the "white," slope-forming sandstone that forms the slope between the western edge of the dune field and Esplin Point (Hayden, 2013). The contact between the upper (white) and middle (pale red) units is visible in a bedrock wash along the western edge of the dune field. However, both white and pale red to pink sandstone outcrop in some interdune areas in the active core of the dune field.

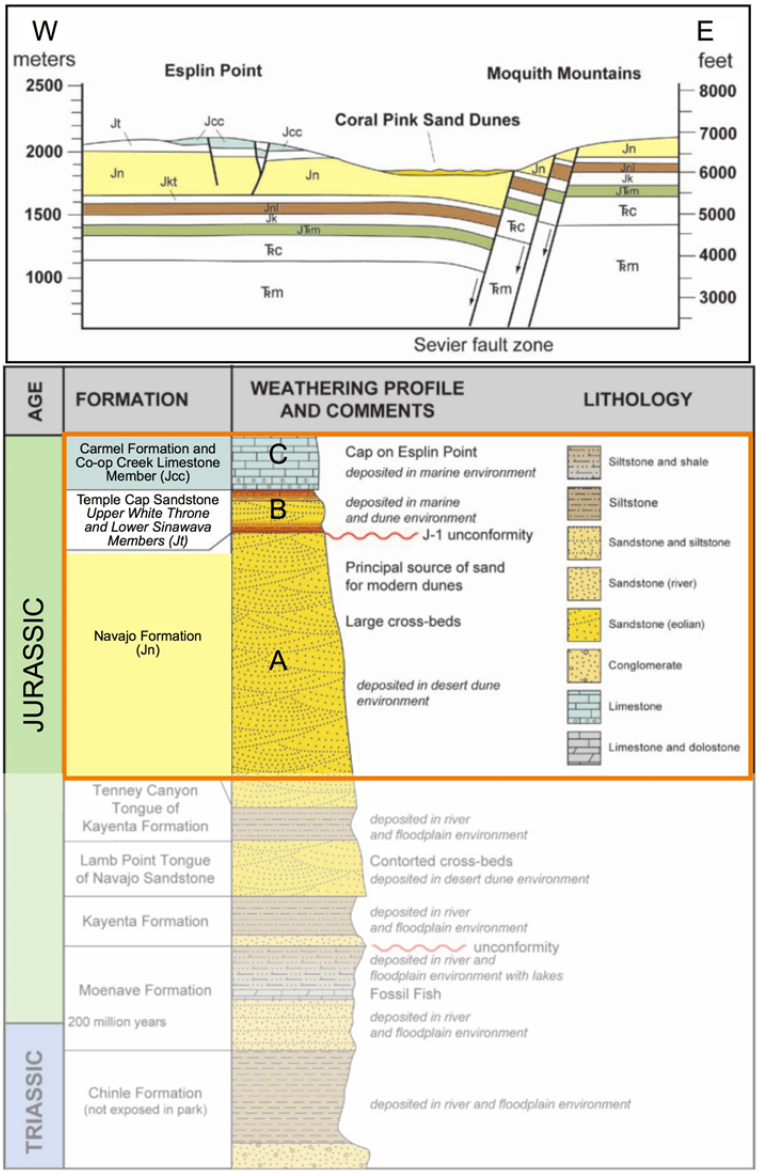

Figure 2: The bedrock surrounding and underlying the dune field is dominated by the Jurassic sedimentary rocks that characterize the Colorado Plateau. (A) The dune field is underlain by the upper part of the Navajo Formation (Jn), a well-sorted quartz sandstone that varies in color from light gray to orange and is characterized by large cross beds. The upper Navajo is generally less resistant than other sandstones in the region and forms the shallow slope that reaches from the cliffs of Esplin Point to the western edge of the dune field. The lower part of the Navajo forms the cliffs exposed in the Sevier scarp and Moquith Mountains to the east of the dune field. (B) The Temple Cap Sandstone (Jt) consists of two members and is comprised of a cliff-forming quartz sandstone and a slope-forming mudstone or siltstone that supports vegetation. This unit is present in the cliffs of Esplin Point, west of the dune field. (C) The Carmel Formation and Co-op Creek Limestone are cliff-forming units that outcrop at the top of Esplin Point to the west of the dune field. Adapted from Ford et al. (2010).

2.2.1.2 Temple Cap Formation and Co-op Creek Limestone Member of the Carmel Formation

The Middle Jurassic Temple Cap Formation and Co-op Creek Limestone form the cliffs of Esplin Point directly west of the Lower Dune Field. The Temple Cap Formation (Figure 2B) consists of the interfingering Upper White Throne Member and the Lower Sinawava Member. The Upper White Throne Member is "yellowish-gray to pale-orange, very thick bedded, well-sorted, fine-grained quartz sandstone with high-angle cross-bed sets as much as 20 feet (6 m) thick" (Hayden, 2013). The Lower Sinawava Member is a "moderate-reddish-brown mudstone, siltstone, and very fine grained, gypsiferous, silty sandstone…(W)here present, it forms a prominent, narrow, vegetated slope at the top of the Navajo Sandstone; weathered reddish-brown clay particles form vertical streaks that stain the upper, 'white' portion of the Navajo Sandstone" (Hayden, 2013). The Co-op Creek Limestone overlies the Temple Cap Formation (Figure 2C) and is described as a "light-olive-gray to light-gray, thin- to medium-bedded, micritic limestone and sandy limestone interbedded with mostly light-gray, thinly laminated to thin-bedded, calcareous shale, play limestone, and very fine to fine-grained sandstone" (Hayden, 2013).

2.2.2 Geomorphology

Hayden (2013) defines six Quaternary, aeolian geomorphic units within the lower dune field, whereas Ford et al. (2010) define five. Here I use definitions taken from both sources. Below, these units are described from south to north (Figure 3).

2.2.2.1 Stabilized Aeolian Sand Sheet (Qes)

This unit is comprised of sagebrush-stabilized aeolian deposits in the form of rolling sand hills without preserved slip-faces (Ford et al., 2010). Such sand sheets form

in low sediment supply conditions controlled by the presence of vegetation, a high water table, and/or periodic surface water cover (Lancaster, 1995). Ford et al. (2010) note the sharp boundary between the stabilized sand sheet and the partially stabilized, more sparsely vegetated dune forms to the north and east, as well as a more transitional boundary to more dense, pinyon-juniper woodland to the west and south. This dense, pinyon-juniper woodland boundary marks a transition to mixed alluvial and aeolian deposits to the west and mixed alluvial and colluvial deposits or hummocky aeolian sand to the south (Hayden, 2013).

2.2.2.2 Partially Stabilized Dunes (Qeps)

This part of the Lower Dune Field is a transitional zone between the stabilized sand sheet to the south and west and the active core of the dune field to the north (Ford et al., 2010; Hayden, 2013). Dunes in this unit range from small transverse to parabolic-like dunes, are stabilized to partially stabilized, and are somewhat chaotic in nature (Ford et al., 2010; Hayden, 2013). The most distinctive feature of this unit is the curious presence of scattered ponderosa pines, discussed in further detail in Section 2.3.3.2.

2.2.2.3 Dissected Sand Ramp (Qesr)

This unit is present along the southeast margin of the Lower Dune Field between the drainage of Sand Wash and the Sevier escarpment. Ford et al. (2010) combine this unit with the stabilized sand sheet and Hayden (2013) describes it as “sand ramps and aprons against steep-sided buttes” and groups it with hummocky aeolian sand outside the dune field. Of all the Quaternary units in the dune field, this is the most perplexing as its origin and relationship to other units is unclear.

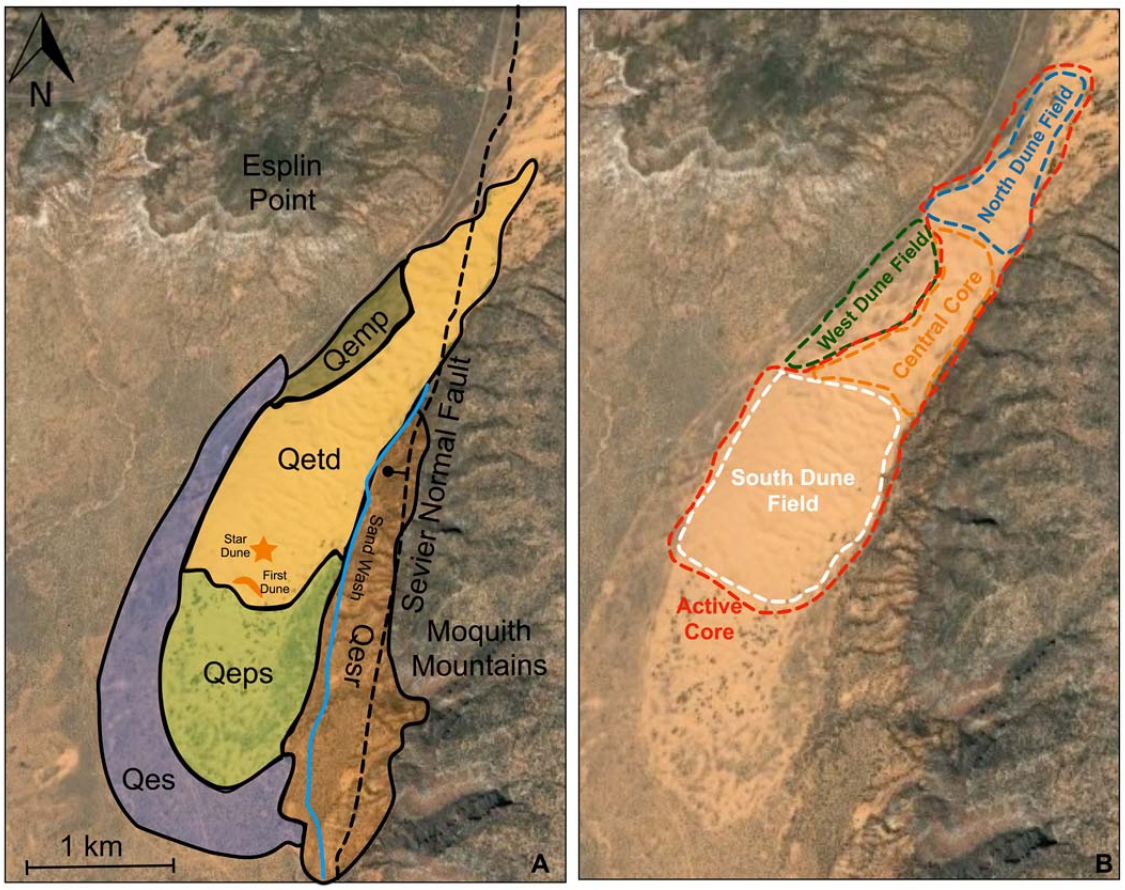

Figure 3: (A) The CPSD is comprised of five major aeolian geomorphic units as defined by Hayden (2013) and Ford et al. (2010). Described from south to north, they include: Qes, a vegetated, stabilized sand sheet; Qeps, partially stabilized dunes; Qesr, a dissected sand ramp with an unknown depositional origin; Qetd, the active dune core which is characterized by transverse to barchanoidal ridge dune forms that transition into climbing dunes that cover the Sevier scarp; and Qemp, vegetated, marginal parabolics. Note that First Dune, which contains a bedrock core, is likely responsible for the altered wind flow that results in an anomalous star dune immediately to the north. (B) The major regions of the active core, used for discussion, include the south dune field, the central core, and the north dune field. The marginal parabolics are referred to as the west dune field.

2.2.2.4 Active Core of Transverse Dunes (Qetd)

The boundary between the partially stabilized dunes to the south and the core of the active dune field to the north is marked by the abrupt termination of ponderosa and by a large, transverse dune with a bedrock core known as First Dune. This dune is unique in that Navajo Sandstone outcrops at its crest and down its northern slip face. North of First

Dune is a single star dune that has transitioned from several smaller transverse dunes into a star dune and back at least two times since 1960 (Wilkins et al., 2003; Ford et al., 2010). North of the star dune is a series of several transverse dunes, approximately 10 to 15 meters in height, with crests that trend northwest-southeast, perpendicular to the primary winds out of the southwest. As you continue north into the active core of the dune field, dunes transition from transverse to barchanoid ridges. Ford et al. (2010) report that crest spacing increases from approximately 180-215 meters at the southern part of this unit to approximately 300 meters between barchanoid ridges at the northern part. However, observations from 2014 Landsat imagery do not show this systematic increase in crest spacing. As of 2014, crest spacing ranges from approximately 80-200 meters, and does not show any obvious systematic changes throughout the dune field. At the extreme north end of the Lower Dune Field, the active core transitions into echo and climbing dunes where the dunes encounter the Sevier scarp.

2.2.2.5 Marginal Parabolic Dunes (Qemp)

Along the northwest margin of the Lower Dune Field is a unit comprised of smaller, sparsely to densely vegetated parabolic dunes (parabolics). The limbs of these parabolics are oriented approximately parallel to the dominant wind direction, and therefore likely formed in the same wind regime as did the transverse and barchanoid ridges in the active core of the dune field (Ford et al., 2010). The western boundary of this unit is defined by a linear sand ridge approximately 5 meters in height. This may be a vegetated linear dune that formed as remnant parabolic limbs merged, but solitary linear dunes are not common (Cooke et al., 1993). This raises the question as to whether this feature may be influenced by underlying topography or other processes. The western

margin of this unit is approximately 25 to 40 meters higher in elevation than is the core of the dune field. Stabilizing vegetation consists primarily of sparse to dense sagebrush scrub, but other small shrubs, grasses, as well as pinyon and oak, are also present.

2.2.3 Dune Field System State

Without external antecedent or boundary conditions, dune patterning and morphology is considered a predictable, self-organizing system that will achieve maximum organization as a result of internal dune-dune interactions (Werner and Kocurek, 1999; Kocurek and Ewing, 2005; Ewing, 2009; Ewing and Kocurek, 2010). However, a dune field's system state, or degree of organization, is a function of its response to climatic changes in the external environment. Using GIS analysis of repeat aerial photography, Wilkins and Ford (2007) show that the CPSD transitioned from a more clustered state in 1960 to a more uniform state in 1997, indicating that the dune field was likely evolving from a change in external conditions. This transition resulted in an increase in dune-crest length and spacing, as well as a net shift of sediment from the southwest (upwind) end of the dune field into the interior of the active core over this time period.

2.2.4 Structural Setting

2.2.4.1 Transition Zone

The CPSD are located in a transition zone (Figure 4) between two major regional structural provinces: the Basin and Range Province to the west and the Colorado Plateau Province to the east (Ford et al., 2010). The Transition Zone (TZ) in its simplest terms can be thought of as the margin of the Colorado Plateau where Basin and Range-type extension has occurred (Brumbaugh, 2008). The TZ shows characteristics of both

provinces; TZ heat flow, upper mantle velocities, and deep electrical conductivity are similar to Basin and Range whereas the TZ's high elevation, relatively limited block-style faulting, and high apparent elastic thickness are more similar to the Colorado Plateau (Wannamaker et al., 2001).

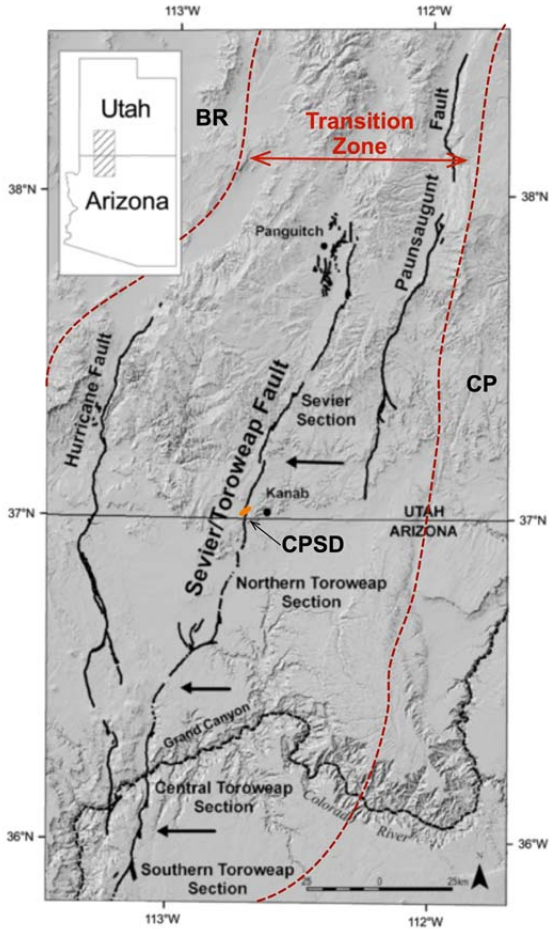

Figure 4: The CPSD dune field is located in the structural transition zone between the Basin and Range Province (BR) to the west and the Colorado Plateau Province (CP) to the east (Lund et al., 2008; Ford et al., 2010). The Transition Zone is characterized by relatively undeformed Jurassic sedimentary rocks of the Colorado Plateau that have undergone Basin and Range-style extension. It is defined by three normal faults that represent the eastern-most extent of Basin and Range Extension: The Hurricane Fault, The Sevier/Toroweap Fault, and the Paunsaugunt Fault. The Lower Dune Field of the CPSD occurs on the downthrown hanging wall of the Northern Toroweap Section of the Sevier/Toroweap Fault. Adapted from Lund et al. (2008).

2.2.4.2 Sevier Normal Fault

The Sevier stretches for approximately 250 km from Panguitch, Utah in the north to the Colorado River, Arizona in the south (Figure 4). The largely continuous, NE-SW trending fault, along with the sub-parallel Hurricane Fault to the west and the Paunsaugunt Fault to the east, is one of three major normal faults that define the TZ (Figure 4) (Lund et al., 2008; Ford et al., 2010). Vertical displacement along the Sevier generally increases to the north and ranges from 475 meters at the Utah-Arizona border to 1,500 meters in southern Sevier County (Ford et al., 2010). The fault has been divided into three sections (Figure 4) as defined by Lund et al. (2008): The Sevier Section is the northernmost section and stretches from Panguitch to Clay Flat; the Northern Toroweap Section reaches from Clay Flat south to the northern end of the Toroweap valley; and the Central/Southern Toroweap Section reaches from the northern Toroweap valley to south of the Colorado River.

The CPSD are located in the Northern Toroweap Section, approximately 6 km south of Clay Flat. The Northern Toroweap Section is comprised of a 1 km wide fault zone containing many anastomosing and braided fault strands (Lund et al., 2008; Ford et al., 2010). At the CPSD, the Sevier strikes approximately N. 30° E., dips 75° W and shows about 475 meters of displacement (Ford et al., 2010). Within a few kilometers north of the CPSD, at the transition between the Northern Toroweap Section and the Sevier Section, is Clay Flat. Clay Flat coincides with a major left step in the Sevier (Figure 4) and has been interpreted to be a small pull-apart basin (Anderson and Christenson, 1989). Clay Flat is a closed depositional basin that restricts movement of sediment to the north through the Yellowjacket and Sethys drainages (Lund et al., 2008).

Nowhere does this section of the fault show displacement of Quaternary deposits, and it is estimated that this section of the fault has a vertical slip rate of less than 0.1 mm/ year (Lund et al., 2008). Surface rupturing earthquakes are estimated to have a recurrence interval greater than 30,000 years (Lund et al., 2008; Hayden, 2013).

2.2.4.3 Mapped Antithetic Faults

Hayden (2013) maps two fault splay zones north of the Lower Dune Field (Figure 1). At least two antithetic faults are exposed in quarries north of the Lower Dune Field at the drainage divide between Sand Wash flowing to the south and Yellowjacket Canyon flowing to the north. Blocks between the Sevier and these antithetic fault splays are tilted 8° to 45° to the west (Hayden, 2013). Field inspection of these faults shows that there is no discernable fault scarp along their trace, but rather their presence is inferred by the juxtaposition of Co-op Creek Limestone against Navajo Sandstone as well as brecciation of both units. Another series of fault splays exist near the segment boundary of the Northern Toroweap Section and the Sevier Section at Clay Flat, approximately 10 km north-northeast of the Lower Dune Field.

2.3 Climate

2.3.1 Precipitation and Temperature

The CPSD are located in a steppe environment that is transitional between the arid climate of the Great Basin and the cooler, more temperate climate of the mountains to the north. The closest weather station to the dune field is in town of Kanab, 17 km to the west. Based on a record back to 1899, the region has an average mean annual precipitation of 34.91 cm, a mean annual temperature of 12.4°C, mean July temperature of 24.2°C, and mean January temperature of 1.5°C. The highest average monthly

precipitation occurs in January (4.13 cm) and the lowest in June (0.952 cm) (Utah Climate Center, available at https://climate.usurf.usu.edu/).

2.3.2 Wind Regime

The closest weather station with available long-term wind data is in Las Vegas, Nevada, 235 km southwest of the CPSD. These data show that regional winds in January through March are predominantly out of the WSW, transition to the SW for April and May, and to the S for June, July, and August, and back to WSW for the remainder of the year. The highest average wind speeds occur in June and mean annual wind speeds are 14.5 kph (9 mph) out of the WSW (NOAA, available at http://www.weather.gov/climate/). These wind directions for Las Vegas likely translate relatively well to the sand dunes, since transverse and barchanoid ridges trend NW-SE, which makes sense for this wind direction. However, field observations indicate that there may also be a strong northerly component of wind during the winter months at the CPSD that results in temporary dune crest reversal. This wind reversal is not captured by the Las Vegas record.

2.3.3 Vegetation

Vegetation plays a crucial role in affecting dune field evolution and individual dune morphologies. Vegetation can act to stabilize otherwise active dune forms creating dune types including parabolics, nebkas, coppice dunes, etc. Additionally, vegetation can cause perturbations in the local wind regime by increasing surface roughness as well as decreasing sediment supply by aiding in the creation of a protective skin for stabilized dunes (Barchyn and Hugenholtz, 2013). The vegetation surrounding the CPSD is dominated by pinyon-juniper woodlands (*Pinus monophylla* and *Juniperus osteosperma*)

and sagebrush scrub (*Artemisia filifolia* and *Artemisia tridentata*) to the west and ponderosa pine (*Pinus ponderosa)* forest in the Moquith Mountains to the east (Ford et al., 2010).

2.3.3.1 Marginal Parabolic Dunes Vegetation

Vegetation within the parabolic dunes on the northwestern margin of the Lower Dune Field likely acts to stabilize and anchor the dune limbs. In addition to parabolics in this part of the dune field, there are also many small nebkas or coppice dunes that form as sand accumulates in dense vegetation. Vegetation in this part of the dune field is predominately sagebrush, but sparse juniper and oak as well as grasses and other xeric shrubs are common. Vegetation decreases in density as you move east toward the active core of the dune field. Sagebrush is especially dense between the linear dune marking the western margin of the dune field and the road. On the west side of the road, there is a sharp transition to a pinyon-juniper dominated landscape.

2.3.3.2 Dune Field Ponderosa Pines

One of the distinguishing and interesting characteristics of the Lower Dune Field is the presence of sparse, but large ponderosa pines growing in the partially stabilized dunes at the southern extent of the dune field at elevations ranging from 1,750 – 1,785 m (5,740 – 5,855 ft.). Ponderosa typically thrive at elevations between 2,100 – 2,500 m (6,900 – 8,200 ft.) and tend to grow on mountain slopes or mesa tops (Ford et al., 2010; Betancourt, 1990). Ford et al. (2010) speculate that the presence of these trees at an anomalously low elevation may be indicative of a shallow water table, within the rooting depth of ponderosas, resulting from the southern dip of the dune field in combination with the high permeability of the dune sand. Tree cores collected from this stand by

Wilkins et al. (2005) indicate that the stand was likely established at the beginning of the Little Ice Age (LIA), around the beginning of the 15th century.

In addition to the stand of living ponderosa in the southern part of the Lower Dune Field, there are also several small stands of ponderosa snags (dead trees) in the active core of the dune field. A radiocarbon date taken from the top of one of these snags indicates that it died, presumably because of inundation and burial by dunes, approximately 200 years BP (Wilkins et al., 2005; Ford et al., 2010).

2.3.4 Late Holocene Climate

Based on radiocarbon dates of buried ponderosa snags, dates from optically stimulated luminescence (OSL), and ages of living ponderosa in the southern part of the dune field determined using dendrochronology, Ford et al. (2010) have established a Late Holocene climate chronology for the CPSD.

2.3.4.1 Pre-Little Ice Age

Prior to the LIA, there were several periods of dune activity, dating back at least 4,000 years, as evidenced by OSL ages (Ford et al., 2010). The exact timing and character of these periods of activity is uncertain.

2.3.4.2 Little Ice Age

At the onset of the LIA, a Northern Hemisphere cool period that lasted from ca. AD 1440-1860 (Grissino-Mayer and Swetnam, 2000; Hereford, 2002), the dune field transitioned to a more stabilized state, and stands of ponderosa were established both on the eastern edge of the now active core of the dune field and in the southern part of the dune field (Wilkins et al., 2005). Studies of cut-fill arroyo cycles in nearby Kanab Creek (Summa-Nelson and Rittenour, 2011), the Paria River (Hereford, 2002), and the

Escalante River (Hayden and Rittenour, 2011) all show aggradation during this period, ending with a sharp transition to arroyo cutting in the late 19th or early 20th century. This cooler, wetter period is recorded in the dune field by the presence of layers of muddy soil and forest duff in some interdune areas. Radiocarbon dates from one such layer show that these mud layers were deposited during the LIA between approximately 470 and 200 years BP (Wilkins et al., 2005). These muddy layers may be the result of flash floods from side canyons, as evidenced by sheet flood deposits and rip-up clasts.

2.3.4.3 Post-Little Ice Age

At approximately 200 years BP, an increased period of aridity likely brought on increased dune field activity, as evidenced by the inundation and death of ponderosas (determined from radiocarbon dates) along the western margin of the active dune field (Ford et al., 2010). From 1960 to 1997, the dune field evolved from a more clustered to a more uniform state, as it responded to a pulse of sediment caused by a series of late 19th century to early 20th century droughts (Wilkins and Ford, 2007).

CHAPTER THREE: METHODS

3.1 Detrending Underlying Topography

Underlying, antecedent topography has been shown to affect boundary conditions that control dune morphology and patterning (Kocurek et al., 2007; Derickson et al., 2008; Ewing and Kocurek, 2010; Ewing, 2009; Yang et al., 2011). Antecedent topography can create heterogeneities throughout the dune field by affecting dune type (depositional vs. transient) and by affecting boundary conditions such as local moisture gradients, local wind direction, and vegetation. The topography surrounding the CPSD is strongly influenced by structural controls related to the Sevier, and it is likely that there are also structural influences on the bedrock topography underlying the dune field itself (Ford et al., 2001). The first step in defining the antecedent topography of the CPSD is to look for major trends in the underlying topography and identify potential antithetic fault zones using analysis of a high-resolution DEM.

3.1.1 Creating a Topographic Data Set

Recent advances in and releases of global raster digital elevation model (DEM) datasets, in combination with advances in global positioning systems (GPS), have increased the ability of geomorphologists to study aeolian landforms and understand constructional events within a three-dimensional, topographic context (Ewing and Kocurek, 2010; Hugenholtz and Barchyn, 2010; Yang et al., 2011). In addition to large scale, relatively coarse-resolution datasets such as ASTER GDEM (Advanced Spaceborne Thermal Emission and Reflection Radiometer Global Digital Elevation

Model) (Hugenholtz and Barchyn, 2010), SRTM (Shuttle Radar Topography Mission) (Yang et al., 2011), and USGS NED (United States Geological Survey National Elevation Dataset), geomorphologists are also beginning to use high-resolution topographic data acquired using LiDAR (Light Detection and Ranging) technologies (Rango et al., 2000; Ewing and Kocurek, 2010; Nield et al., 2011; Nield and Wiggs, 2011; Montreuil et al., 2013; Feagin et al., 2014).

LiDAR is an active remote-sensing technology that works by emitting a narrow beam of energy (often in the near infrared wavelength) and recording the time it takes for the beam to return to the instrument, and the angle at which it returns. These returns, in combination with very accurate GPS systems, create a georegistered point cloud that represents the target surface. LiDAR systems can be mounted to either airborne (Airborne Laser Swath Mapping or ALSM) or terrestrial (Terrestrial Laser Scanning or TLS) apparatuses. Most dune field-scale studies utilizing LiDAR use ALSM methods (Woolard and Colby, 2002; Saye et al., 2005; Ewing and Kocurek, 2010; Stockdon et al., 2009; Wolfe and Hugenholtz, 2009), whereas smaller dune-scale studies have utilized ground-based TLS to document small-scale morphological features and changes (Rango et al., 2000; Montreuil et al., 2013) and sediment-transport mechanisms (Nield and Wiggs, 2011). ALSM data are available for very few dune fields and are very expensive to acquire. Here, I show that TLS can be used to collect high-resolution elevation data at the dune-field scale at a fraction of the cost of ALSM.

3.1.2 Terrestrial Laser Scanning

Because of the small size (less than 10 km^2) of the CPSD, a high-resolution DEM was required to detrend the modern dune surface. ALSM LiDAR data are not available for this region and are costly to acquire. The highest-resolution, publicly available elevation data for the dune field comes from the USGS National Elevation Dataset (NED) and has a horizontal resolution of 10 meters. Preliminary analysis of this dataset was completed in order to test the detrending method, but the resulting detrended surface was not at a high enough resolution to be useful for identifying potential topographic structural features (Figure 5). In order to create my own high-resolution elevation dataset, I used ground-based terrestrial laser scanning.

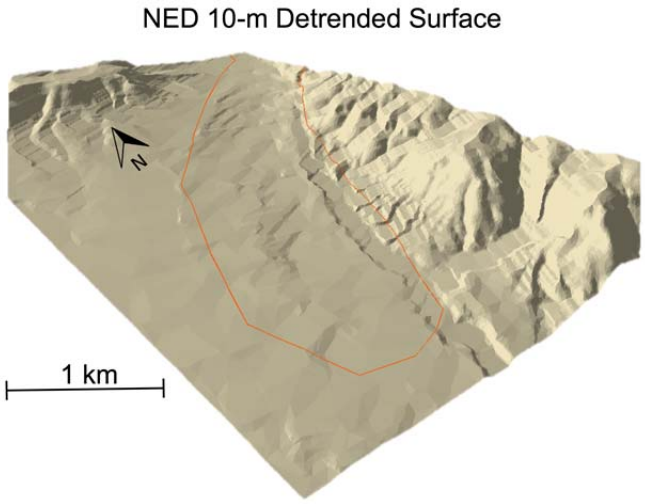

Figure 5: This detrended surface is the result of preliminary analysis of a NED-derived 10-meter resolution DEM. The orange line represents the extent of the dune field. The surface showed some evidence for scarp-like features within the dune field and on its margins, but resolution was too low to make confident interpretations.

3.1.2.1 Field Methods

I used a RIEGL VZ-1000 terrestrial laser scanner (Figure 6) to collect high-density elevation points for the entire Lower Dune Field, an area of approximately 5 km^2.

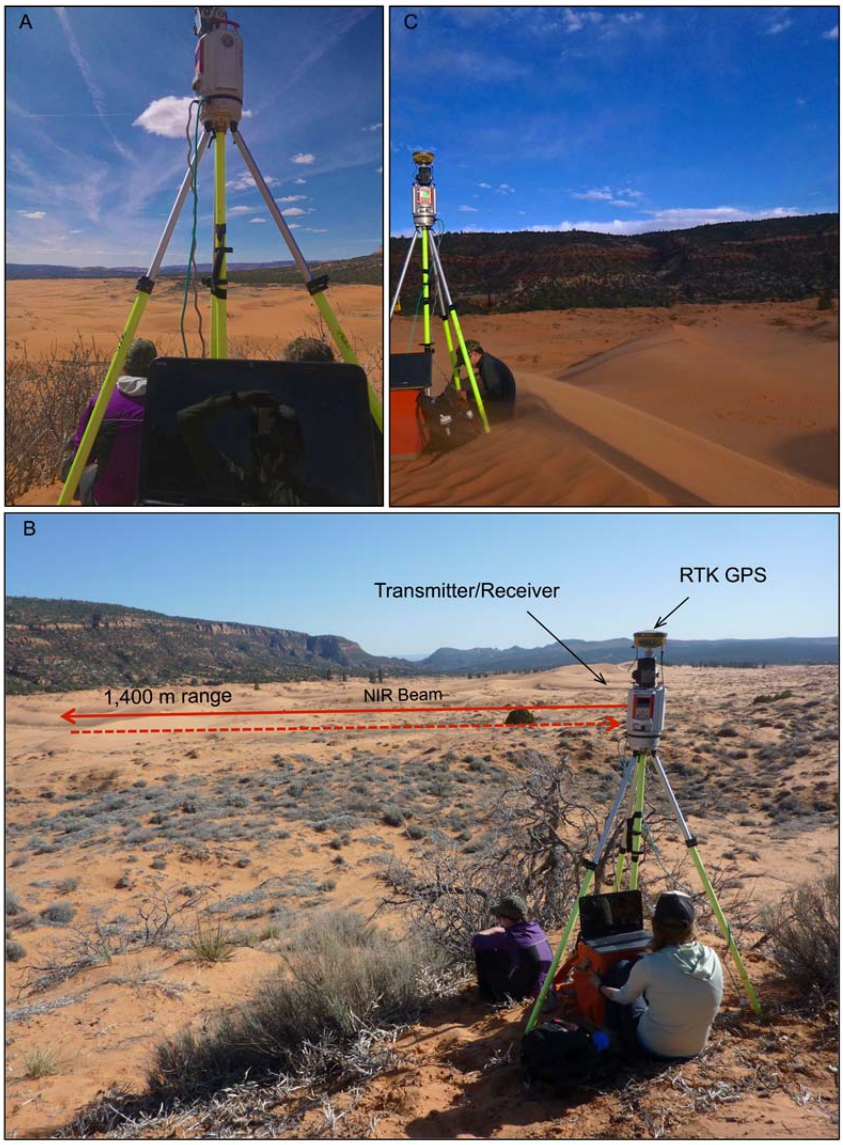

Figure 6: A terrestrial laser scanner (TLS) was used to collect dense point cloud elevation data in order to create a high-resolution DEM. The TLS was mounted on a tripod and connected to a control laptop. Scans were taken from (A) the Sevier scarp on the eastern edge of the dune field; (B) along the linear ridge that forms the western margin of the dune field; and (C) from crests of large dunes in the core of the dune field. A TLS emits a NIR beam with a 1400-meter range, and records the time it takes for reflected returns to return to the receiver (B). These returns form a georegistered point cloud that represents the target surface.

The scanner performed 360° scans at 34 scan locations (Figure 7). These scan locations were chosen to maximize coverage of interdune areas. For the northern part of the Lower Dune Field, scans were acquired from atop the Sevier escarpment (Figure 7A). Most scans were acquired from the linear ridge that forms the western boundary of the Lower Dune Field (Figure 7B). Several scans were also acquired from within the active core of the dune field from the crest of First Dune, the star dune, and other large dunes in the active core (Figure 7C).

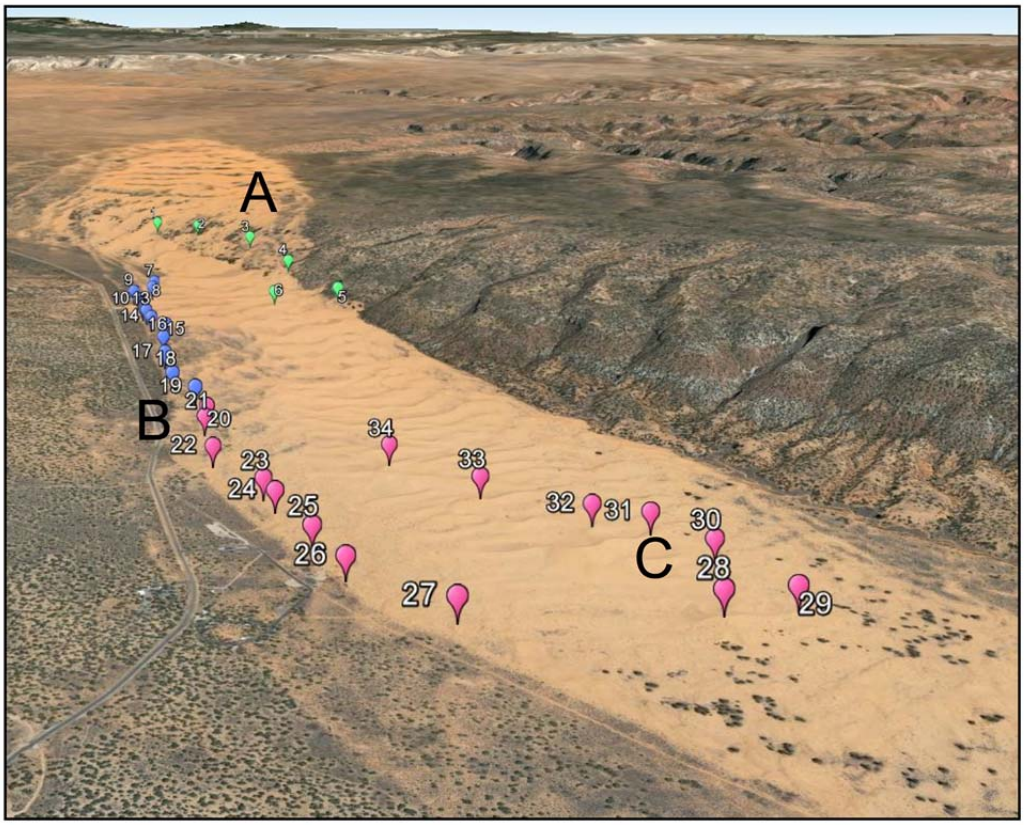

Figure 7: Terrestrial Laser Scanning (TLS) scan positions were strategically chosen to maximize the viewshed of each scan. Scans were taken from high points (A) along the Sevier scarp; (B) along the western margin of the dune field from atop the linear ridge that marks the western edge of the dune field; and (C) from the crest of large dunes in the core of the dune field. Scanning of the approximately 5 km^2 area was completed in three days. Each color pin represents a different day of scanning.

For each scan, the resolution was set to 0.04 degrees and the range was set to its maximum of 1,400 meters. At each scan location, the scanner settings were adjusted for atmospheric conditions and the camera was calibrated for changing light conditions. Six photos were taken for each scan. In order to assign real world coordinates to each data point, the scanner was linked to a Trimble, Real Time Kinetic (RTK) Global Positioning System (GPS) linked to a stationary base station. The height of the base station was measured and all GPS locations were corrected using NOAA's Online Positioning User Service (OPUS, available at http://www.ngs.noaa.gov/OPUS/).

3.1.2.2 Data Processing Methods

The corrected point cloud was imported into RIEGL's processing software, RiSCAN Pro. Using this software, I removed the least accurate points using a deviation filter. I also used an octree filter to remove any redundant points so that I was left with only one point per square centimeter. After the RiSCAN processing, I was left with a point cloud that consisted of 259,464,196 points. Using ENVI image processing software and the BCAL (Boise Center Aerospace Laboratory) LiDAR tools (available at http://bcal.boisestate.edu/tools/lidar), the point cloud was height filtered to classify returns into ground and not-ground points, and the resulting point cloud was rasterized at 5-m and 1-m resolution to create bare earth DEMs.

3.1.3 Previous Detrending Methods

The detrending method used here was adapted from those developed by Ewing, et al. (2008) and Yang et al. (2011). Ewing et al. (2008) developed a method that subtracted the modern dune surface from the underlying topography at White Sands National Monument in New Mexico. They collected ALSM LiDAR imagery of the dune field and

created a 1-meter resolution DEM from the data. In order to detrend the underlying topography, the authors developed an algorithm in MATLAB that searched for local minima in the downwind direction and smoothed the areas between these points. This detrended dune surface was sufficiently detailed to identify several previously unrecognized steps in the underlying topography.

Yang et al. (2011) used a similar method for the Earth's tallest dunes in the Badain Jaran Desert in western China. This dune field covers approximately 1,000 km^2 and is therefore a much larger scale dune field than either the CPSD (on the order of 10 km^2) or the White Sands National Monument (on the order of 40 km^2). Because of the drastic difference in scale, these authors were able to use a SRTM DEM with a much coarser resolution of 90 meters. Using this DEM, over 350 points in interdune areas were manually chosen in ArcGIS. Nearest neighbor interpolation was used to create a surface between these points, showing the trend in underlying topography.

3.1.4 ArcGIS Analysis to Detrend Surface

The DEMs created in ENVI were imported into ESRI's ArcGIS 10.2 software. I used the Focal Statistics Analysis tool to filter and detrend the elevation data. This filter works by using a moving, wedge-shaped window that points in the downwind direction. Each pixel is assigned the value of the lowest elevation found within this window, which results in high points along dune crests being reassigned elevations of the downwind interdune area. This effectively "removes" the dunes from the underlying topography (Figure 8).

I chose a wedge-shaped window that opens 10° to the northeast, that is, the downwind direction. The radius of the window was set to equal the maximum spacing

between dune crests (approximately 200 meters), so that for each dune crest the filter would be sure to reach every point in the downwind interdune area. The statistics type for the tool was set to "MINIMUM," so that the lowest elevation value found within the window was assigned to the pixel in question. I applied a hillshade to the resulting DEM with a sun angle from the northwest in order to highlight any linear features that may parallel the northeast-trending antithetic faults mapped north of the dune field.

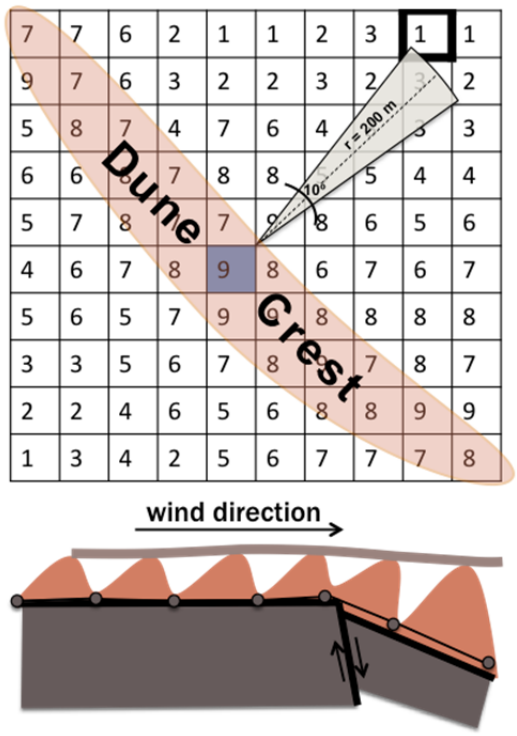

Figure 8: Conceptual illustration of the detrending method used to remove the dunes from the underlying, antecedent topography. Using the Focal Statistics tool in ArcGIS, the filter uses a moving, wedge-shaped window to search the DEM for the lowest elevation in the downwind direction. The window has a radius of 200 meters, which is the approximate maximum dune crest spacing, to ensure that the window reaches the next downwind interdune area. The filter reassigns elevations from the interdune areas to the dunes, effectively removing the dunes from the underlying surface.

3.2 Imaging the Subsurface

I used ground-penetrating radar (GPR) to better resolve the antecedent topography of the CPSD and determine whether or not topographic features are structurally controlled. The detrended dune-field surface (Figure 9) reveals three (3) zones with potential antithetic fault splays: 1) the south dune field just east of First Dune and the star dune; 2) the western margin of the dune field and into the central core; and 3) the north dune field between the Sevier scarp and the road. I used GPR surveys in these areas, with data collection transects oriented perpendicular to predicted fault splays, in order to detect offset in the bedrock surface and/or subsurface that would indicate fault activity.

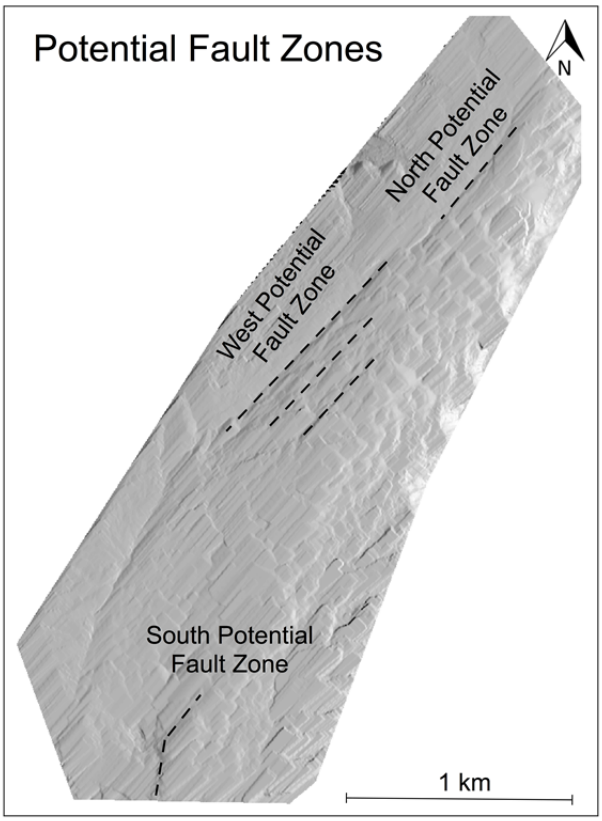

Figure 9: The detrended surface created using the filtering techniques described in Section 3.1.4 was used to identify target zones for GPR survey. These potential fault zones showed steep, scarp-like features with a similar orientation to antithetic faults mapped north of the dune field.

3.2.1 Ground Penetrating Radar

GPR has been established as an effective tool for imaging the internal structure and bounding surfaces of sand dunes (Botha et al., 2003; Havholm et al., 2003; Moller and Anthony, 2003) as well as faults in subsurface sediments and bedrock (Bristow and Jol, 2003; Reiss et al., 2003). GPR works by radiating high-frequency electromagnetic (EM) pulses into the ground, and recording energy that is reflected back to the surface (Figure 10) from interfaces or contacts between materials with contrasting relative permittivity or conductivity, resulting primarily from differences in water content (Jol and Bristow, 2003). Relative permittivity, or the ability of a substance to store and transmit EM energy, controls the velocity at which an EM wave will propagate through a substance; these velocities range from ~0.03 m/ns for water to 0.15 m/ns for some soils and igneous rocks to 0.3 m/ns for air (Baker et al., 2007). Substrate materials with high electrical conductivity can easily attenuate EM signals, and therefore sediments with low conductivity, such as sand, will allow good EM penetration, whereas sediments with high conductivity, such as clay, will cause attenuation of an EM signal (Baker et al., 2007).

GPR surveys employ antennas that emit EM energy at frequencies that typically range from 50-1000 MHz. Frequency selection is important because lower frequencies with longer wavelengths increase penetration depth, whereas higher frequencies with shorter wavelengths allow greater spatial resolution (Jol and Bristow, 2003). Vertical resolution for GPR data is ¼ the wavelength; therefore, higher frequencies are able to resolve smaller changes in stratigraphy, whereas lower frequencies allow for greater penetration into the substrate (Jol and Bristow, 2003).

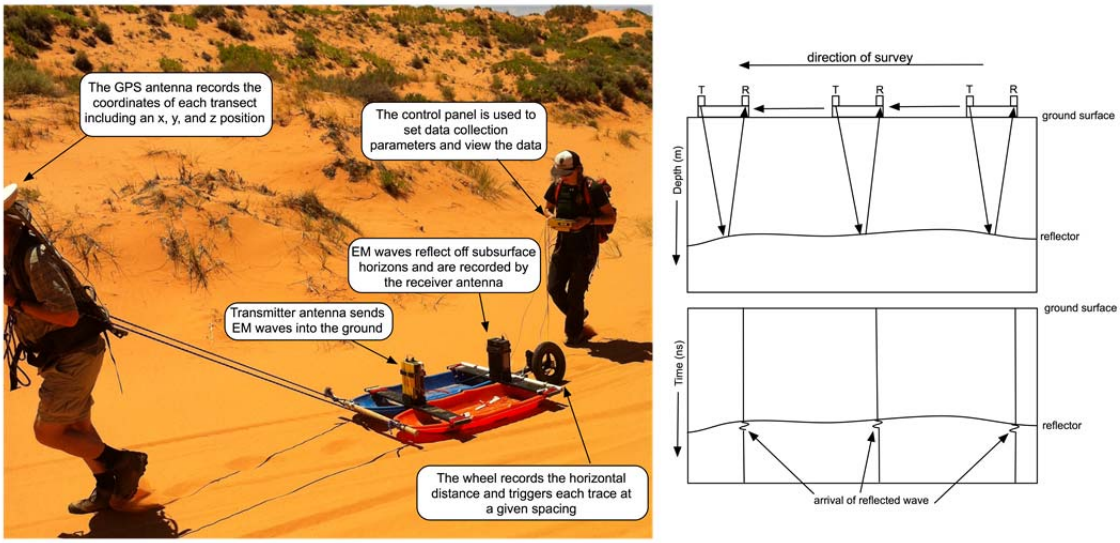

Figure 10: Ground-penetrating radar (GPR) was used to image the subsurface and define the sand-bedrock interface. GPR works by emitting an EM signal from a transmitter antenna. This energy is reflected off of horizons in the subsurface where there is a change in dielectric properties. The time it takes for the wave to return to the receiver antenna is recorded. The apparatus used here consisted of two sleds that were either pulled by hand or by an OHV. UTM coordinate positions were recorded using a GPS antenna, and a wheel was used to record the horizontal position and to trigger traces at a given spacing.

Previous work at CPSD shows that 100-MHz GPR is able to achieve 20-meter depth penetration in the star dune region of the Lower Dune Field (Wilkins et al., 2003). Both the Navajo Sandstone and the sediment derived from the Navajo Sandstone at CPSD are composed of well sorted, primarily quartz sand, which makes them ideal candidates for GPR surveys.

3.2.2 Field Methods

I used 50-MHz and 100-MHz antennas with a 400-V transmitter to image the dune-bedrock interface as well as any structural controls within the bedrock. These low frequencies allowed the optimal balance between penetration and resolution of the EM signal in order to maximize the likelihood that the dune-bedrock interface was imaged.

These frequencies should be able to achieve a vertical resolution of 1.5 m and 0.3 m, respectively.

Antennas and the transmitter and receiver units were housed on a two-sled or four-sled apparatus that was pulled either by hand (Figure 11A) or by an OHV (Figure 11C) depending on the steepness and density of vegetative cover along the transect. A control unit was attached to the receiver and a wheel was attached to the back of the apparatus to measure horizontal distance and trigger traces at a given spacing. For 50-MHz-data collection, the trace spacing was set at 0.5 meters, and for 100-MHz collection, the spacing was set at 0.25 meters. In order to correct for topography and link the radar transects to UTM coordinates, I used a GPS unit linked to a base station. The GPS antenna was attached to either the person pulling the sled apparatus or the OHV and the offset between the antenna and the GPR receiver was noted. GPS coordinates were linked to the GPR data via calibration of the GPR and GPS clocks. Depth to bedrock or other indicated radar horizons was verified in several locations using a hand auger (Figure 11B).

I collected data for 11 transects in the south dune field, 10 transects in the west dune field and central core, and three transects in the north dune field. Transects in the north dune field experienced high attenuation and were not useful for analysis. The location of transects presented here are shown in Figure 12. Most of these transects were oriented west-east, but at least one south-north transect was completed for each section of the dune field in order to trace reflectors between transects.

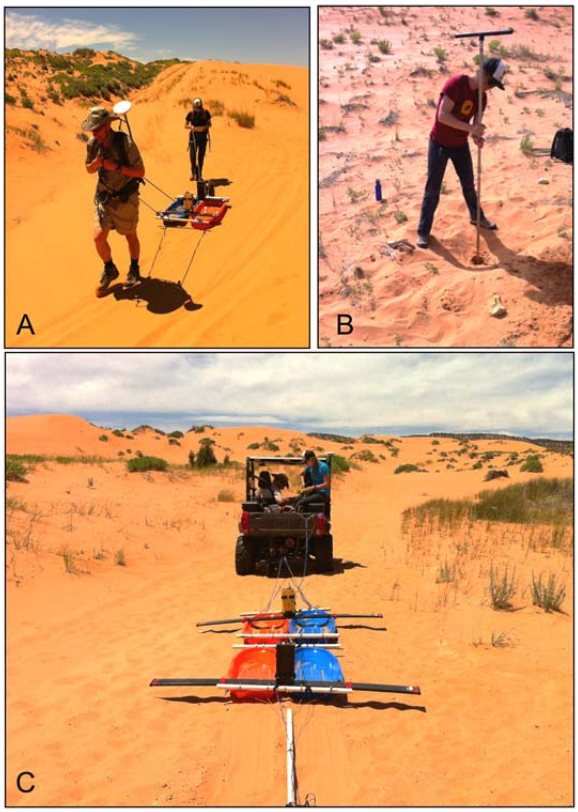

Figure 11: GPR field methods included dragging antennae on a sled apparatus either by hand (A) or using an OHV (C). Both 50 MHz (A) and 100 MHz (C) antennae were used. Depth to bedrock was determined using hand-augering techniques (B).

3.2.3 Processing Methods

GPR data were processed using the following techniques:

1) Raw data files were converted to .segy file type.
2) .segy files were imported to ProMAX seismic processing software. Here, the data were processed using a bandpass filter, time-zero correction, and phase-shift 2D migration. Automatic-gain-control (AGC) was applied to increase the visibility of data at greater depths. Data without the AGC correction more clearly shows the location of the strongest reflectors. Data are shown both with and without the AGC correction.

3) Corrected .segy files were imported into MATLAB where each transect was corrected for topography and plotted. Conversion from travel time to approximate depth was based on a velocity of 0.11 m/ns. This velocity was determined to be ideal for this particular substrate using migration velocity analysis. This technique uses experimental velocities until ideal focusing is achieved.

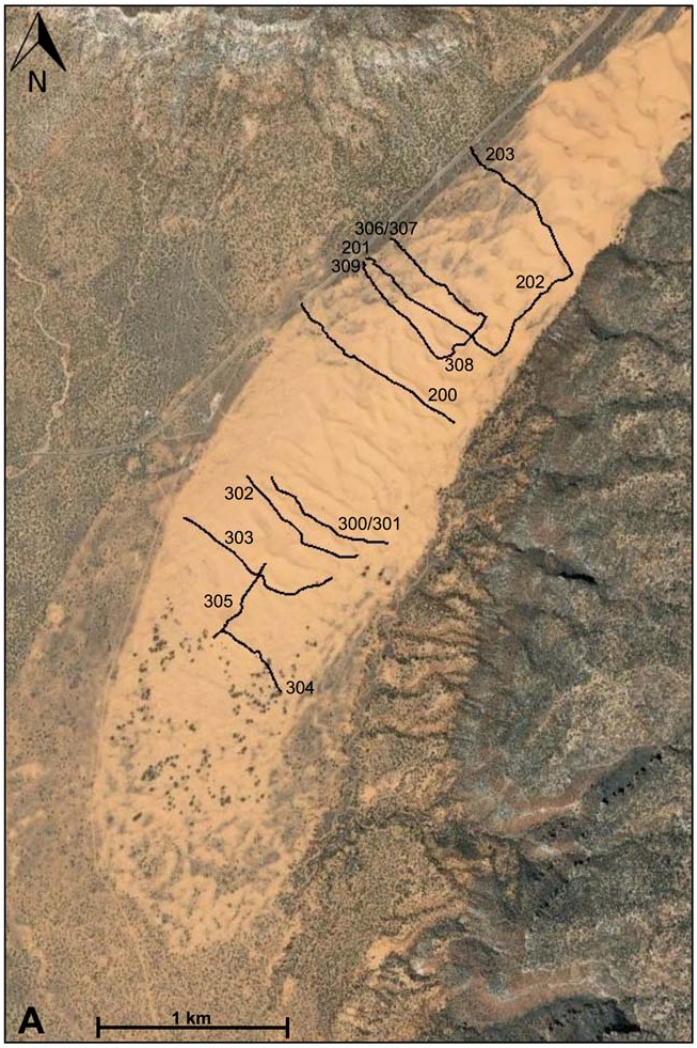

Figure 12: GPR transect locations presented in this research. Transects were generally oriented NW-SE, perpendicular to the strike of hypothesized fault traces, in order to image any offset in the bedrock caused by faulting.

CHAPTER FOUR: RESULTS

4.1 TLS-Derived Digital Elevation Models

Using TLS acquisition methods, I created 1-meter-resolution (1-m) and 5-meter-resolution (5-m) resolution DEMs for the Lower Dune Field (Figure 13A/C). Visually, the 5-m DEM appears to be more accurate as the 1-m DEM shows more prevalent noise indicated by the blocky texture where data points are absent, whereas the 5-m DEM shows a more continuous, realistic surface. Both DEMs have missing data in some places, primarily along Sand Wash and in some interdune areas. Both DEMs are an improvement over the 10-meter-resolution NED DEM, and accurately capture all of the dune crests in the Lower Dune Field.

4.2 Detrended Underlying Topography

Using the methods described in Section 3.1.4, I detrended the DEM of the modern dune surface in order to model the underlying antecedent topography. I applied a hillshade with a 45° sun angle out of the northwest in order to identify topographic features (Figure 13B/D), and also extracted topographic profiles from both the modern dune DEM and the detrended model (Figure 14). Observations of the detrended model are described below.

4.2.1 Detrended DEMs

Detrended DEMs at both 1-m and 5-m resolution are shown in Figure 13 and a 3D visualization of the 5-m-resolution detrended surface is shown in Figure 15. Both detrended models indicate a sharp break, or scarp, along the western edge of the dune

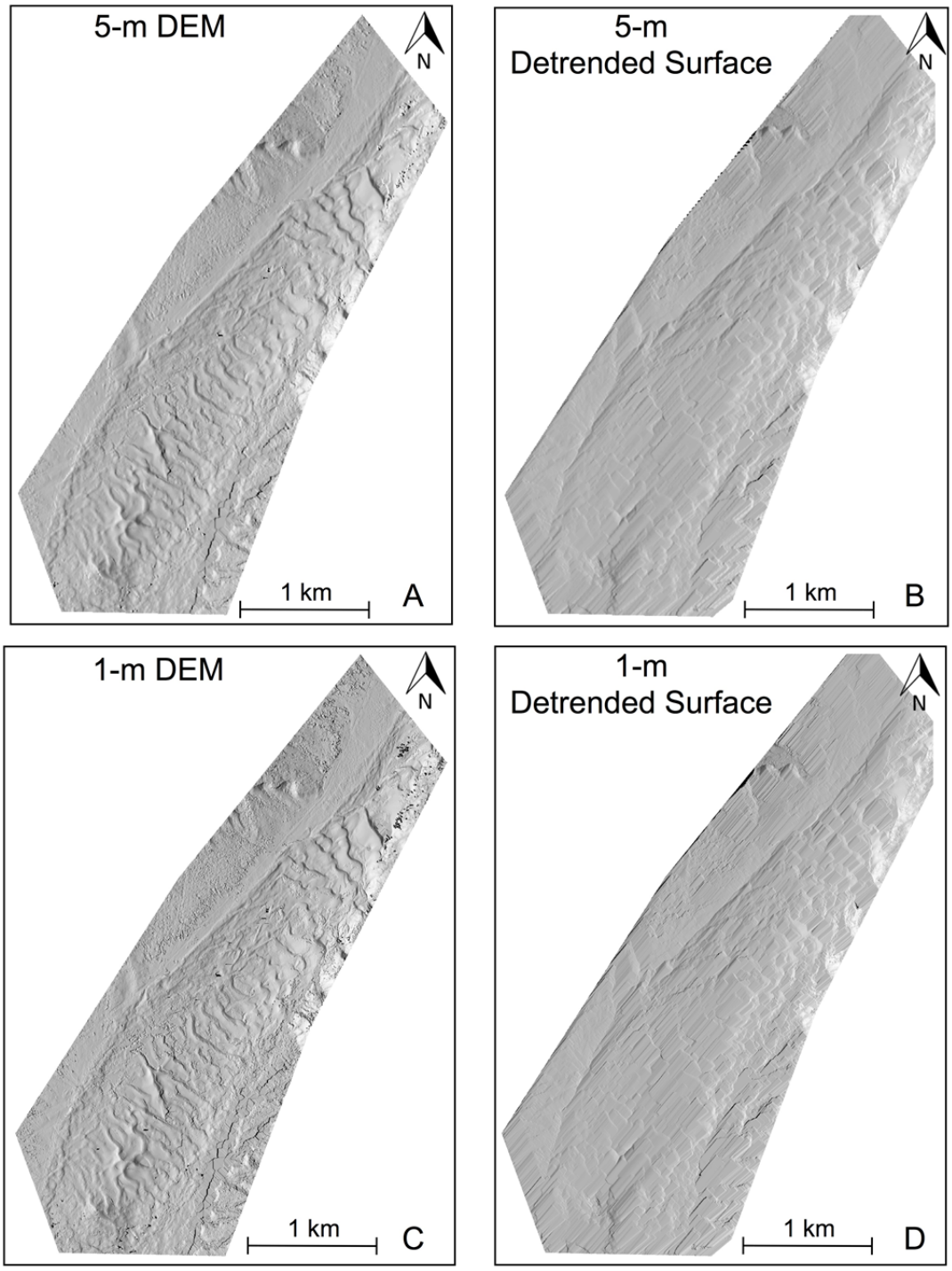

Figure 13: 1-m and 5-m resolution bare-earth TLS-derived DEMs (A and C). These DEMs were used to create detrended surfaces (B and D) that represent the antecedent, underlying topography on which the dunes formed. Visual assessment shows that neither the 1-m or 5-m DEM is a perfect representation of the actual surface, but all dune crests and most interdune areas are well represented. Some inaccuracies exist where the vegetation filter did not adequately remove all vegetation.

field. This offset decreases to the south and exists in three segments with breaks that step to the west as you move from north to south. The surface gradient between the scarp and the active core of the dune field varies from north to south. At the southwest margin there is a quick break that transitions into a broad, shallow, west-to-east gradient into the active core of the dune field. Along the western margin of the parabolics, there is a series of down-to-the-east breaks or steps. Lastly, along the northwest margin the transition is marked by a single, steep break.

Detrended elevations in the active core of the dune field are 30 – 50 meters lower than on the margins of the dune field with the exception of a topographic high near First Dune in the south dune field. This knob is incorrectly located just north of First Dune; the cause of this discrepancy is discussed in Section 5.7. This topographic high has a steep eastern slope but more gradual slopes to the north, south, and west. The lowest elevation in the detrended model is 150 meters west of and 10 – 25 meters lower in elevation than the modern Sand Wash channel (Figure 14 – W1, W2, W3), indicating that the channel is perched in this part of the dune field.

4.2.2 Topographic Profiles

Topographic profiles in Figure 14 illustrate the difference between the dune surface and the detrended surface model (i.e., antecedent topography). Profiles W1, W2, and W3 run west to east from the western margin of the dune field to Sand Wash. These profiles indicate the presence of steps in the underlying topography along the western margin beneath the modern marginal parabolics (Qemp on Figure 3). The steps increase in number, but decrease in offset, as you move from north to south along the western margin. Along this margin the sand cover is thin, ranging from 1-6 meters. However, in

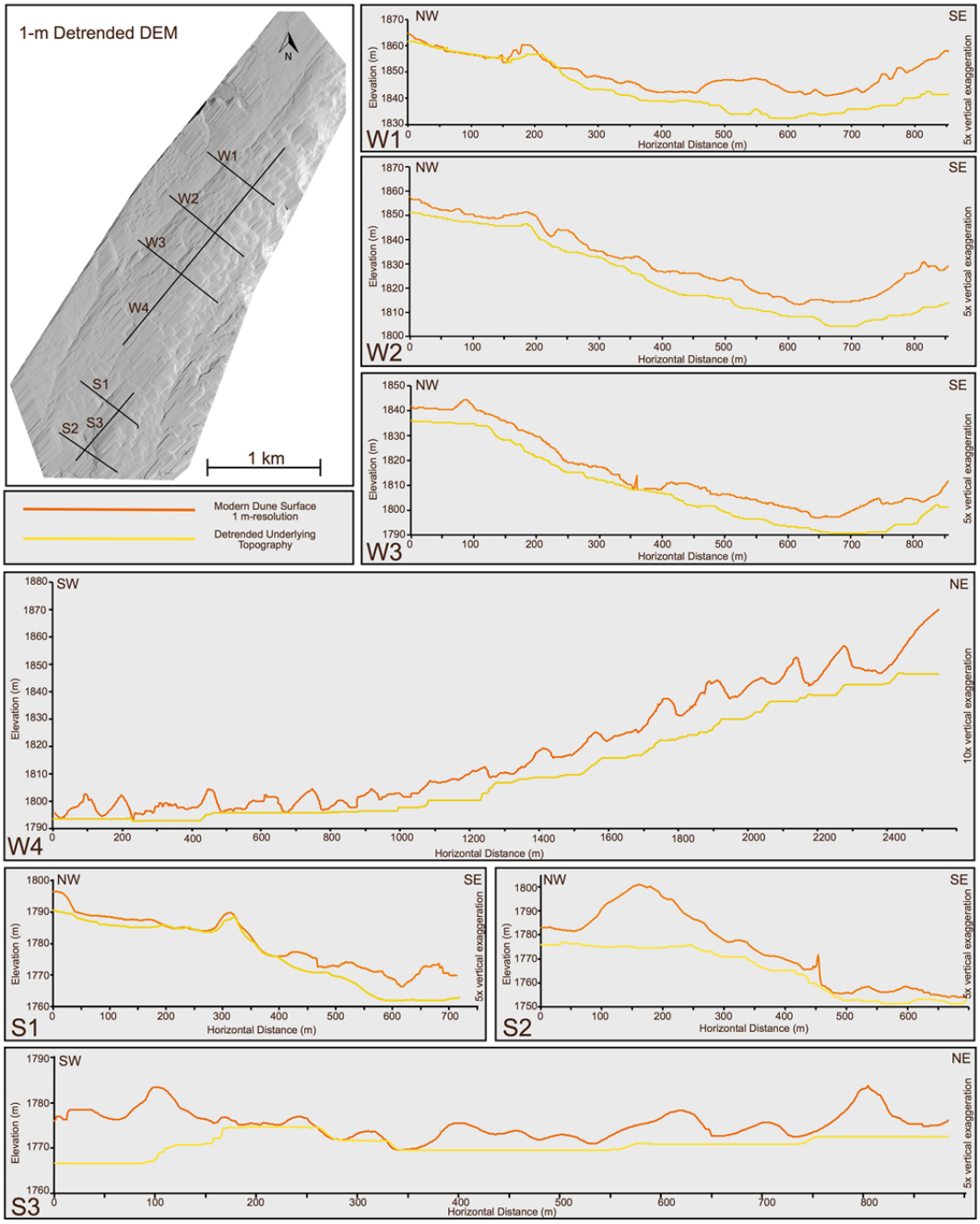

Figure 14: Comparison of the dune surface and the detrended underlying topography. Elevations were extracted from the 1-m DEM and the 1-m detrended surface in potential fault zones. Note that the slope of the detrended surface decreases as you move from north to south and that sand thickness generally increases to the north and east.

the central core of the dune field the sand cover is thicker and increases from

approximately 10 meters in the south to over 20 meters in the north. This increase in sand

thickness to the north is also seen in profile W4. It is interesting to note that these profiles show the lowest point in both the dune and underlying topography is west of the northern reach of Sand Wash, indicating a perched drainage system.

Profile W4 (Figure 14) is a longitudinal profile through the central core of the dune field. This profile shows that the underlying topography slopes to the south with an abrupt change in gradient at 1,300 meters. Here, the gradient changes from 3.6% to the north to 0.53% to the south. The trend of this shallower gradient continues in profile S3. The steeper part of the profile shows several small steps, each with an offset of approximately 5 – 8 meters.

Profiles S1 and S2 extend from west to east across the star dune and First Dune, respectively. Both profiles reveal a steep decrease in the underlying topography just east of these large dunes. Profile S1 indicates very thin sand cover west of the star dune with sand thickness increasing to the east. Profile S2 reveals very shallow sand to the west of First Dune, with increasing thickness on top of First Dune and to the east. Profile S3 suggests that the north-south trend of underlying topography in this southern part of the dune field is generally flat, but with an anomalous topographic high immediately north of First Dune.

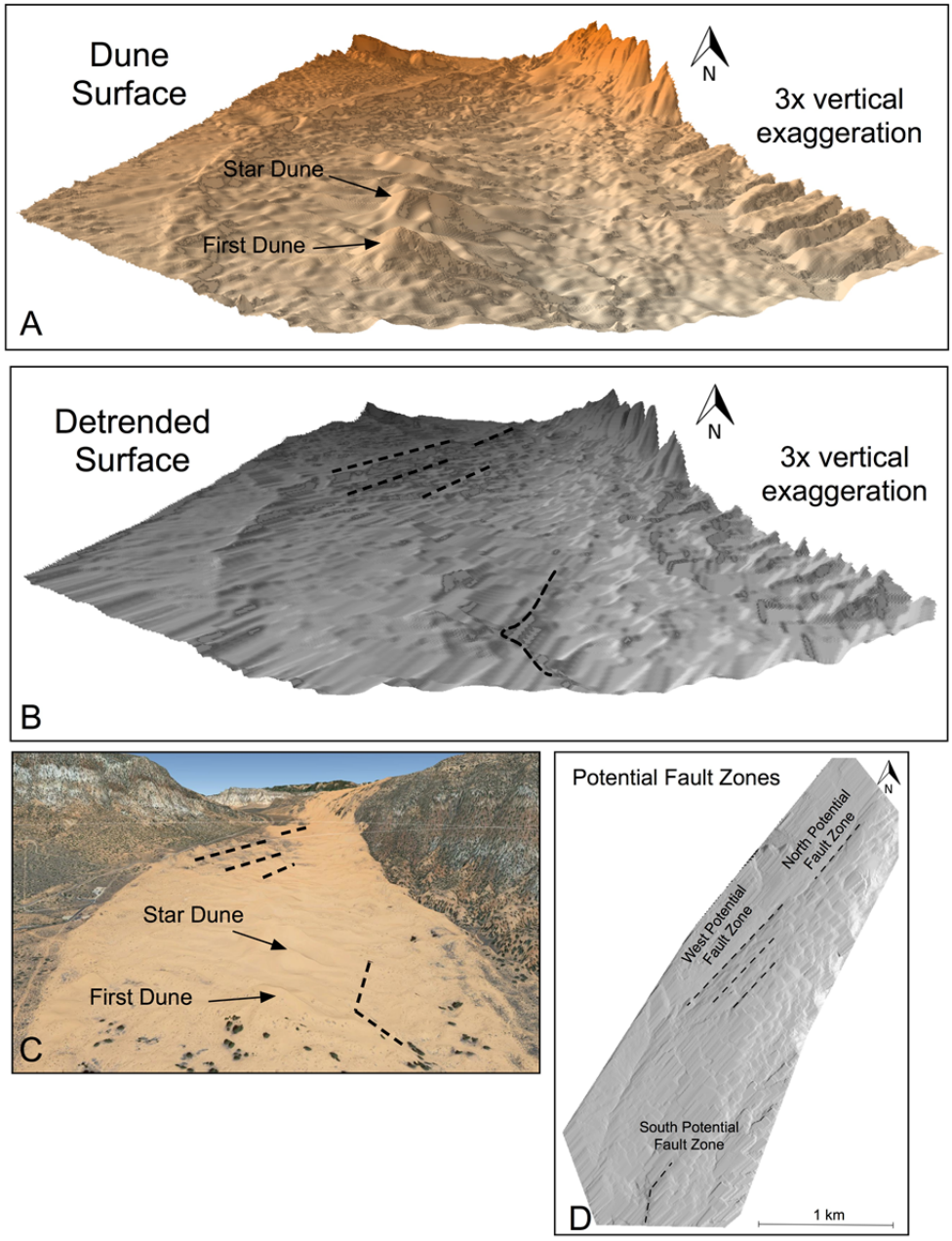

Figure 15: 3D visualization of the dune surface, the detrended surface, and potential fault zones. (A) The current dune surface, based on the 5-m DEM, with 3 x vertical exaggeration. (B) The 5-m detrended surface, with 3 x vertical exaggeration, shows that the dunes are housed in a valley with a steep western side. Several scarp-like features are present, and are denoted with dotted black lines. (C) The location of scarp-like features on a Google Earth imagery show that the marginal parabolic dunes may rest on series of scarps. There is also scarp-like feature just east of the star dune and First Dune. (D) Potential fault zones were identified based on the presence of scarp-like features. GPR surveys were focused in these areas.

4.3 Subsurface Imagery

I used GPR to better resolve and test the accuracy of the detrended model described above. To this end, I identified three target areas based on the detrended model (Figures 13 and 15), and the resulting GPR imagery is discussed below for each target.

4.3.1 South Dune Field

Processed GPR images and interpretations for this part of the dune field are shown in Figures 16 – 20. Locations of the transects are shown in Figure 12. Lines 304 (Figure 16) and 305 (Figure 17) indicate that First Dune is a topographic feature consisting primarily of a bedrock knob with less than 5 meters of sand cover on the eastern, southern, and northern flanks, and approximately 5 meters of sand cover at the top of the knob. To the north of First Dune, the bedrock surface slopes gently up to the north, and W-E transects (Figures 18 – 20) display thin sand cover in interdune areas with a relatively smooth bedrock surface sloping down to the east.

During this GPR field excursion, auger holes were not collected in this part of the dune field. Prior augering by Clement et al. (2006) reveals that, in interdune areas, sand cover is thin and the water table is intermittently perched and corresponds with the sand-bedrock interface. I assume that my transects, located in close proximity to those of this previous study, should show similar depth to bedrock and the water table.

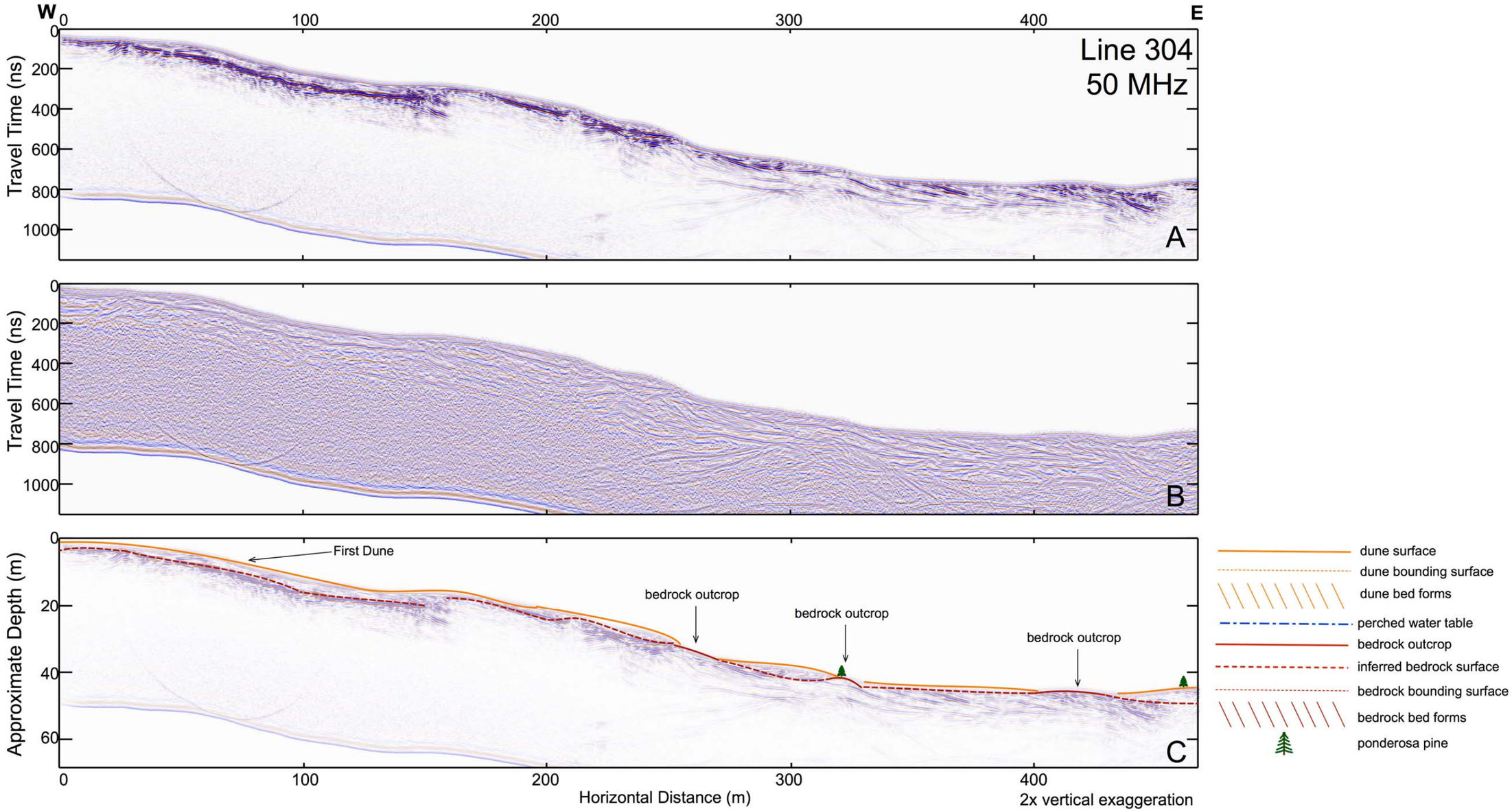

Figure 16: Processed and interpreted GPR data for Line 304 (see Figure 12) along the eastern flank of First Dune. (A) Migrated data; (B) Migrated data with AGC applied; (C) Interpretation for Line 304 shows that First Dune is a topographic feature comprised primarily of bedrock with sand cover that is less than 5 meters thick. It was hypothesized that the topographic offset of this feature was structurally controlled, but no faults were identified. Instead, this bedrock knob is likely an erosional feature.

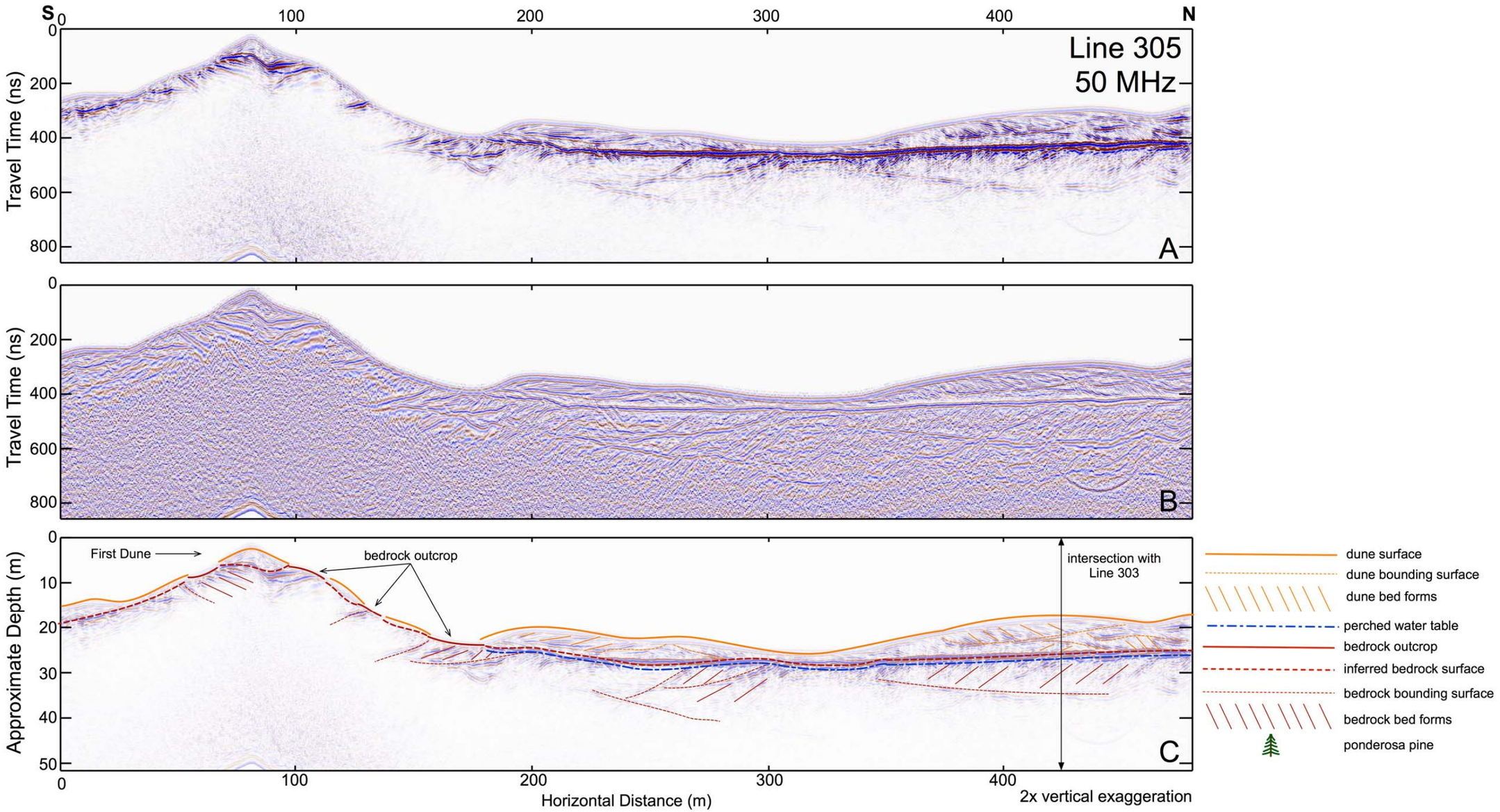

Figure 17: Processed and interpreted GPR data for Line 305 (see Figure 12), a S-N transect that reaches from the south flank of First Dune to the base of the star dune; (A) Migrated data; (B) Migrated data with AGC applied; (C) Interpretation for Line 305 shows that First Dune is a topographic feature comprised primarily of bedrock with sand cover that is less than 5 meters thick. It was hypothesized that the topographic offset of this feature was structurally controlled, but no faults were identified. Instead, this bedrock knob is likely an erosional feature. North of First Dune, the bedrock slopes gradually up to the north. Large bed forms and bounding surfaces are visible within the bedrock. Although depth to the water table was not verified using hang augering in this part of the dune field, Clement et al., 2006 show that there is a perched water table that coincides with the bedrock surface in some places. A perched water table at the dune-bedrock interface may be responsible for the especially strong, flat reflector and may mask any small variations in the bedrock surface.

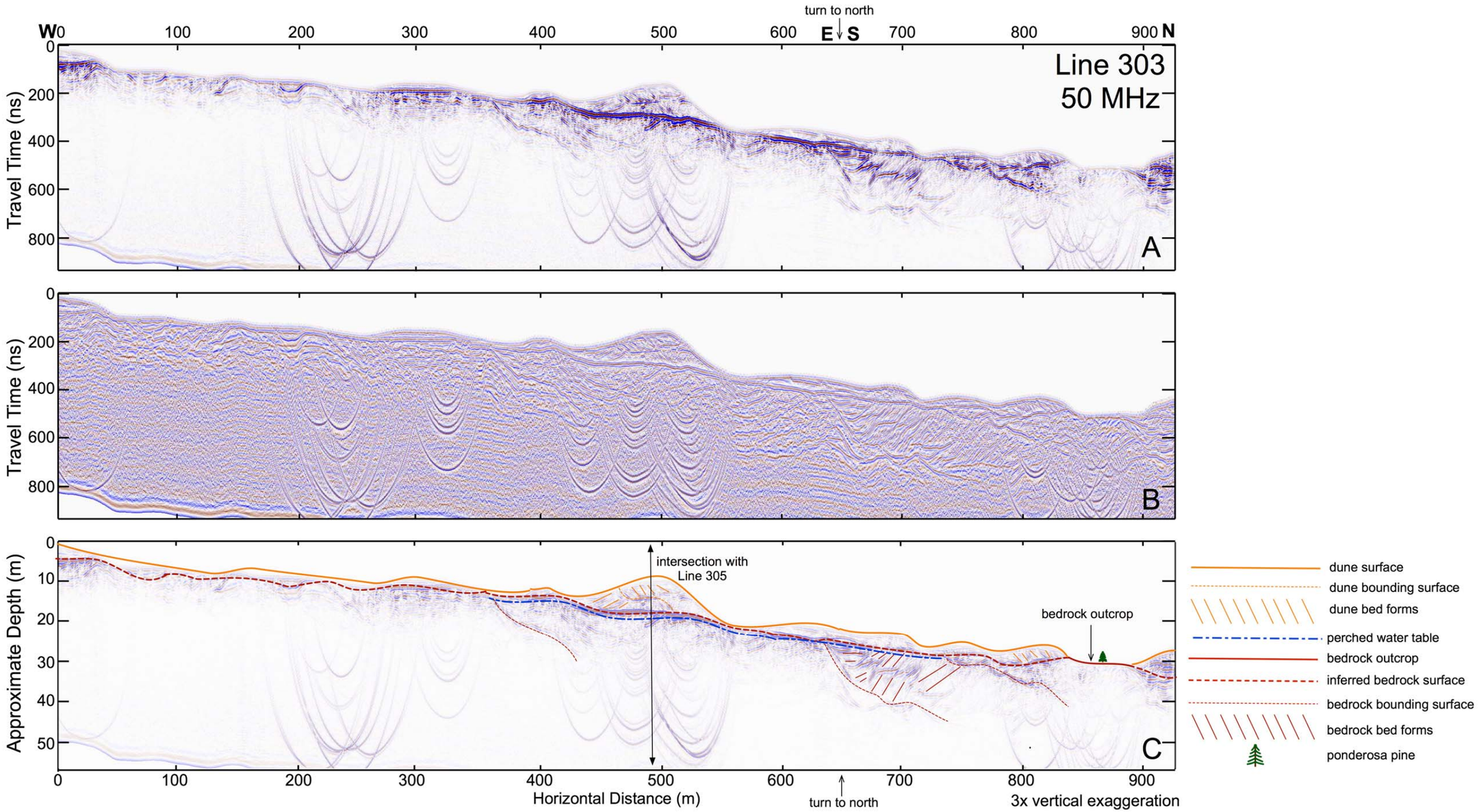

Figure 18: Processed and interpreted GPR data for Line 303 (see Figure 12), a W-E transect that turns to the north at 650 meters. (A) Migrated data; (B) Migrated data with AGC applied; (C) Interpretation for Line 303 shows that in interdune areas there is thin (less than 5 meters) sand cover and that the bedrock generally slopes down to the east. Where the transect turns to the north, bounding surfaces and bed forms become visible within the bedrock.

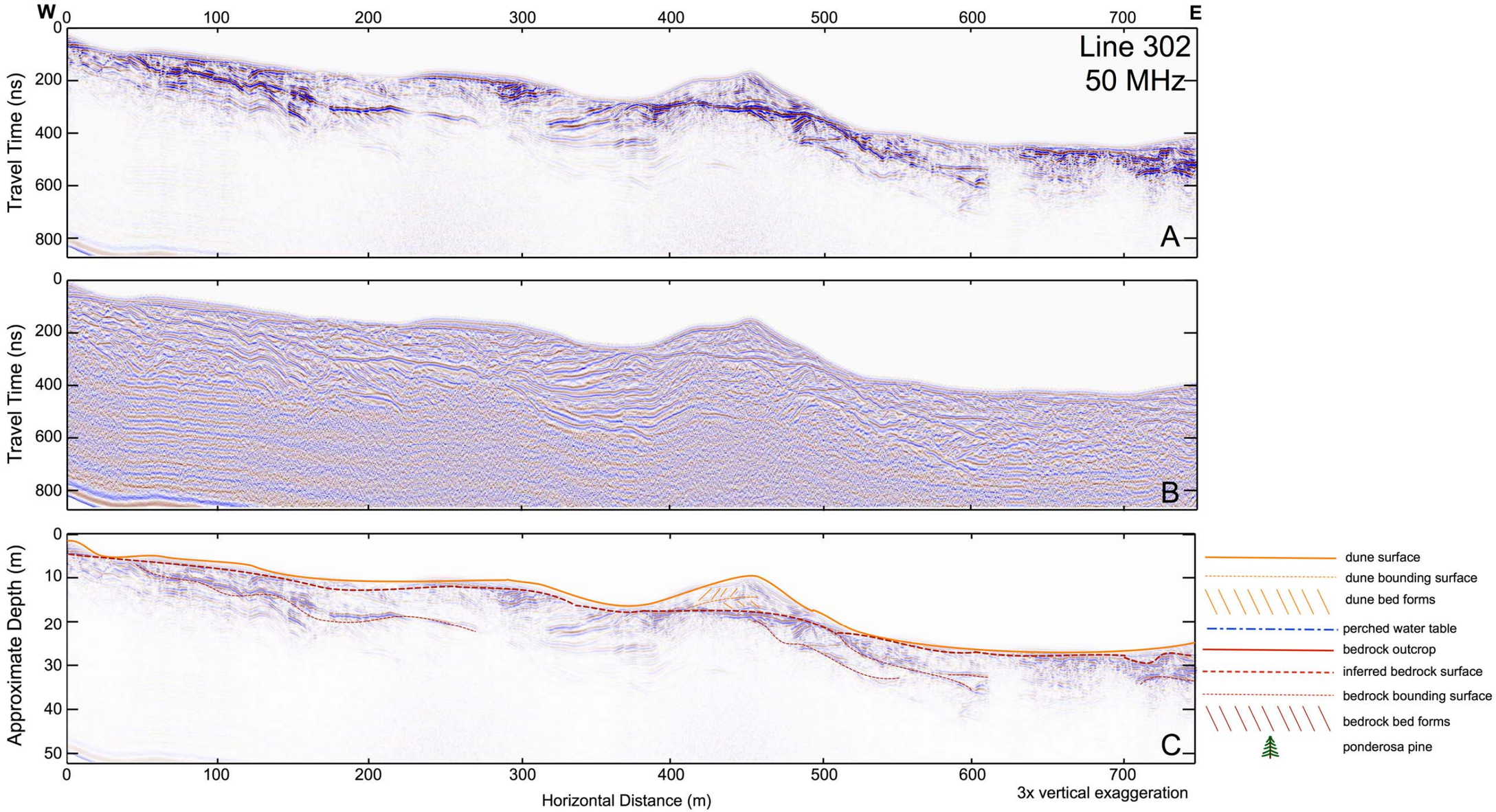

Figure 19: Processed and interpreted GPR data for Line 302 (see Figure 12), a W-E transect that is primarily in interdune areas. (A) Migrated data; (B) Migrated data with AGC applied; (C) Interpretation for Line 302 shows that in interdune areas there is thin (less than 5 meters) sand cover and that the bedrock generally slopes down to the east.

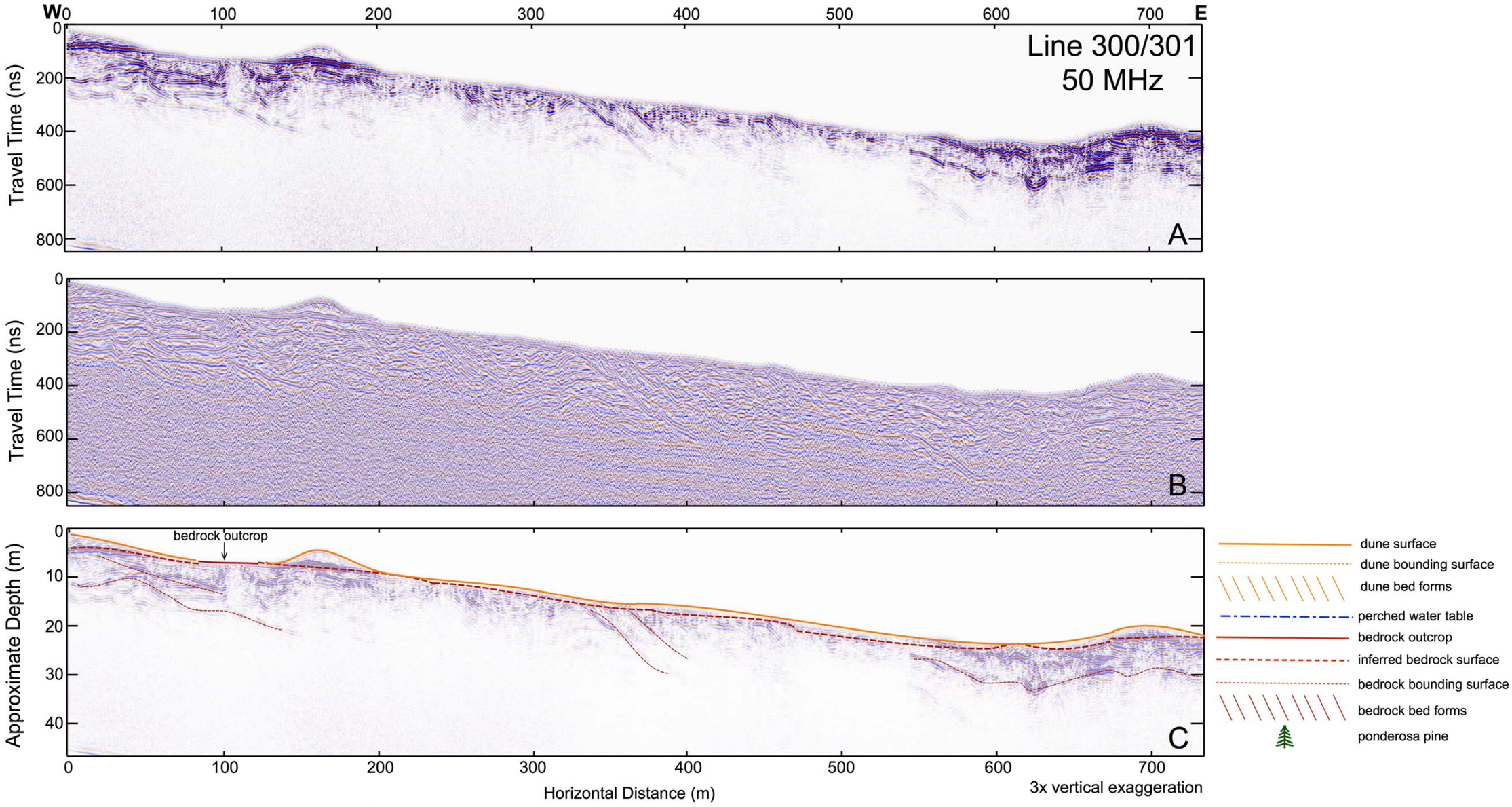

Figure 20: Processed and interpreted GPR data for Line 300/301 (See Figure 12). (A) Migrated data; (B) Migrated data with AGC applied; (C) Interpretation for Line 300/301 shows that in interdune areas there is thin (less than 5 meters) sand cover and that the bedrock general slopes down to the east.

4.3.2 West Dune Field and Central Core

Processed GPR images and interpretations for this part of the dune field are shown in Figures 21 – 27. For locations of these transects refer to Figure 12. Figures 21 – 25 report W-E transects, and Figures 26 and 27 are S-N transects in the central core of the active dune field. Penetration of the EM signal in the west dune field is not as deep as in the south dune field, and the data are generally more chaotic and difficult to interpret. Interpretations of the bedrock surface are based on auger cores and the assumption that the strongest reflector should be the sand-bedrock interface. However, it is important to note that, because of the somewhat chaotic nature and apparent offset of reflectors, tracing the bedrock surface from the limited auger hole data is not always possible. Thus, much of the interpretation is based on a best-guess approach.

The W-E transects reveal generally shallow sand (characterized by dune topography and visible bed forms) on top of a series of shallow, offset reflectors that result in a series of steps that decrease in elevation as you move from west to east. The EM signal is attenuated in some places between these steps, and penetration of the wave is limited to less than 20 meters. The stepping reflector drops off abruptly toward the eastern edge of each transect at approximately the center of the dune field.

East of this drop, a flat to hummocky reflector extends to the eastern margin of the transects. Reflectors beneath this surface are generally sub-horizontal and undulating, and penetration is deeper than to the west. The S-N transects (Figures 26 and 27) clearly exhibit a strong, continuous reflector that coincides with the interdune areas at the base of the dunes. This reflector is smooth, generally dips to the south, and is underlain by weaker sub-horizontal, undulating reflectors. Unlike the subsurface imaged immediately

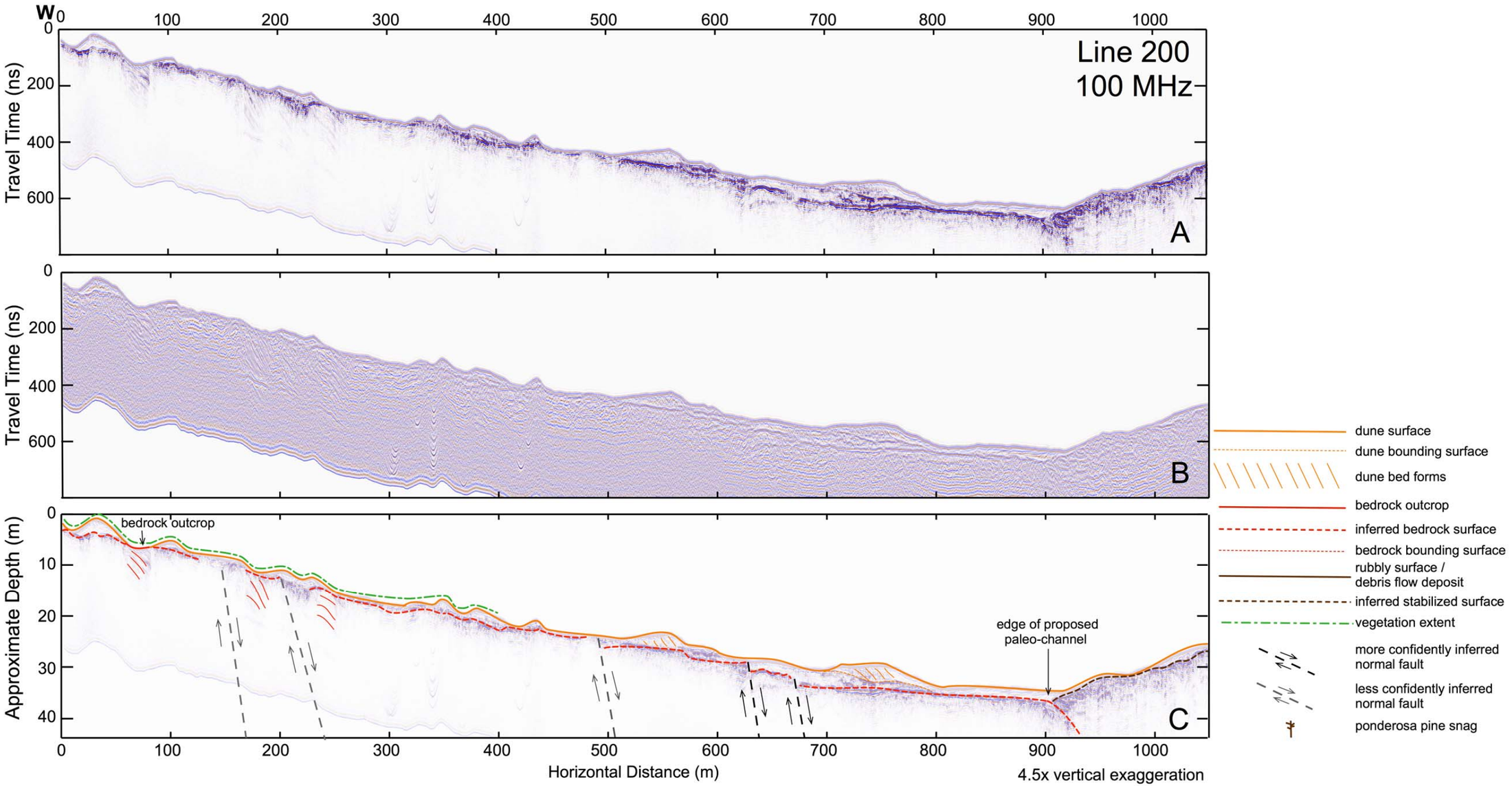

Figure 21: Processed and interpreted GPR data for Line 200 (see Figure 12). (A) Migrated data; (B) Migrated data with AGC applied; (C) Interpretation for Line 200 shows a series of antithetic faults that have an apparent dip of approximately 39° to the east. Bedrock outcrops in the far west part of the transect and shows the contact between the upper "white" sandstone and middle "brown" sandstone of the Navajo Formation. Fault interpretations are based on offset in the bedrock and lack of bedrock reflectors between obvious bedrock reflectors. The bedrock drops off dramatically at 900 meters; this represents the western edge of the proposed paleo-channel. The sediments filling the paleo-channel onlap onto the bedrock at this point.

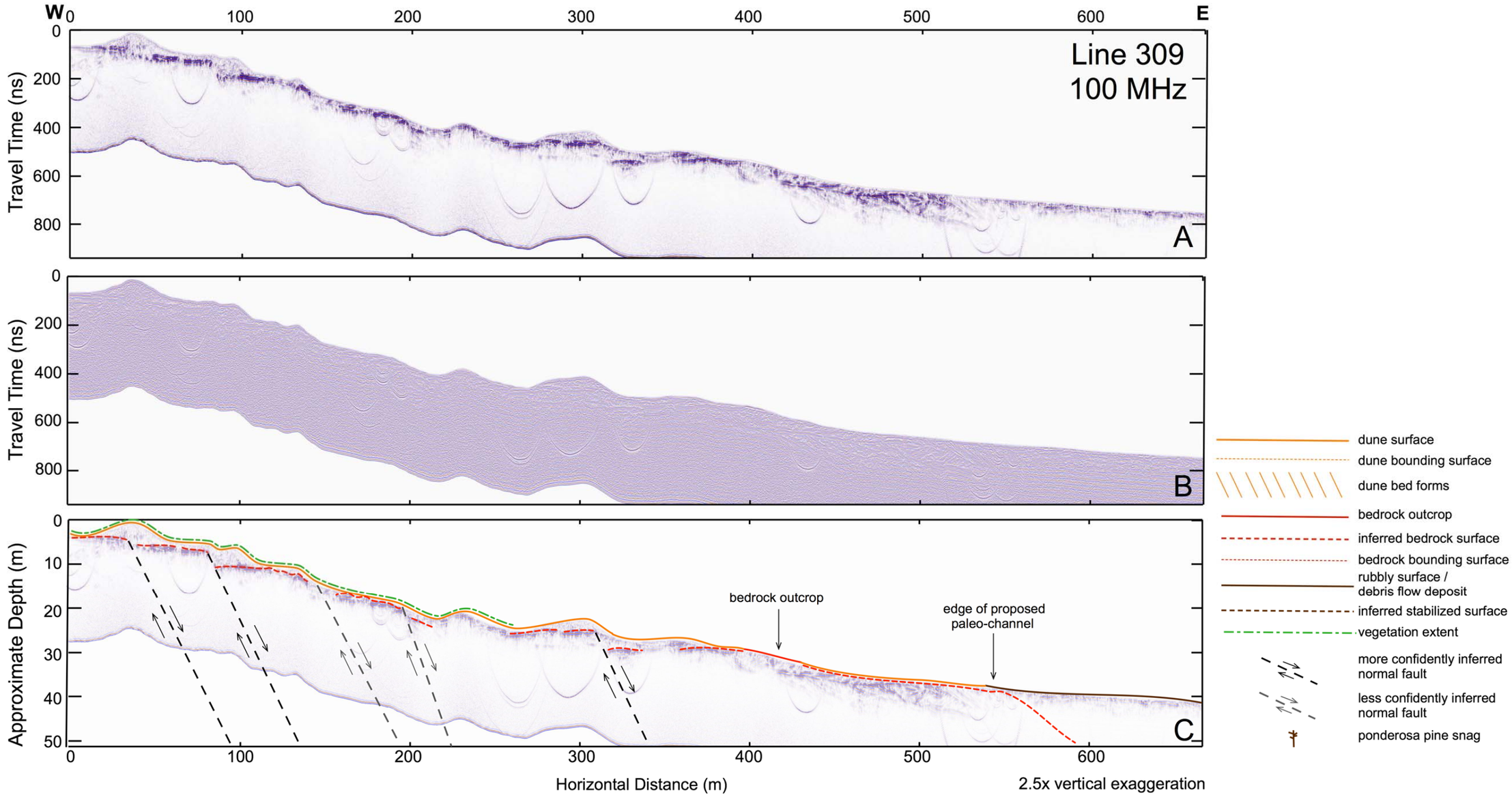

Figure 22: Processed and interpreted GPR data for Line 309 (see Figure 12). (A) Migrated data; (B) Migrated data with AGC applied; (C) Interpretation for Line 309 shows a series of antithetic faults that have an apparent dip of approximately 30° to the east. Fault interpretations are based on offset of the bedrock surface. The bedrock drops off at approximately 550 meters; this represents the western edge of the proposed paleo-channel. At easternmost side of the transect, the rubble surface outcrops in an interdune area. This surface represents a stabilized surface that likely formed during the Little Ice Age atop intercalated fluvial, aeolian, and debris flow deposits.

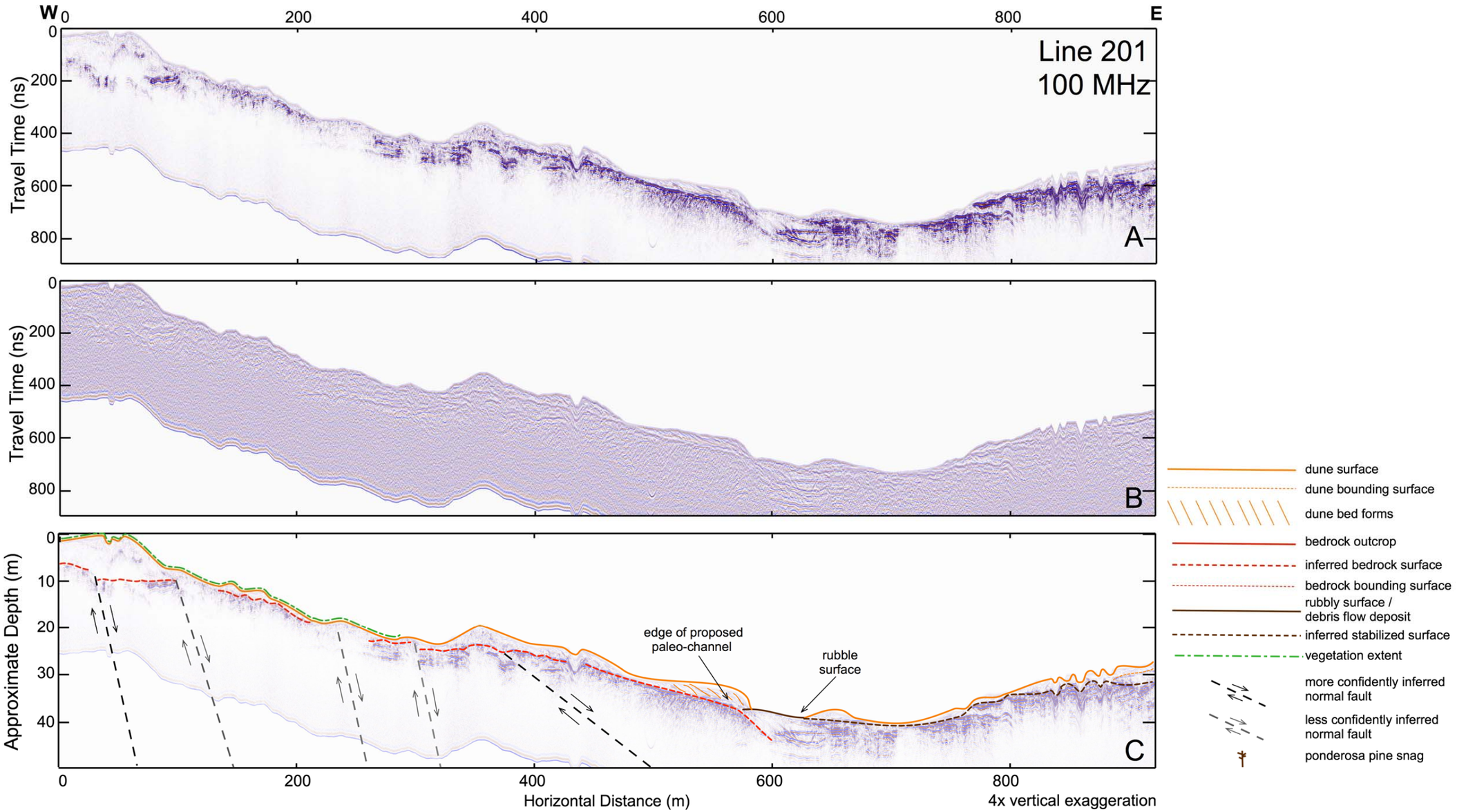

Figure 23: Processed and interpreted GPR data for Line 201 (see Figure 12). (A) Migrated data; (B) Migrated data with AGC applied; (C) Interpretation for Line 309 shows a series of antithetic faults that have an apparent dip of approximately 42° to the east. The bedrock drops off at approximately 575 m; this marks the western edge of the proposed paleo-channel. The rubble surface, which represents a stabilized surface that likely formed during the Little Ice Age, outcrops in an interdune area just east of this drop off. This surface formed on intercalated aeolian, fluvial, and colluvial channel fill sediments.

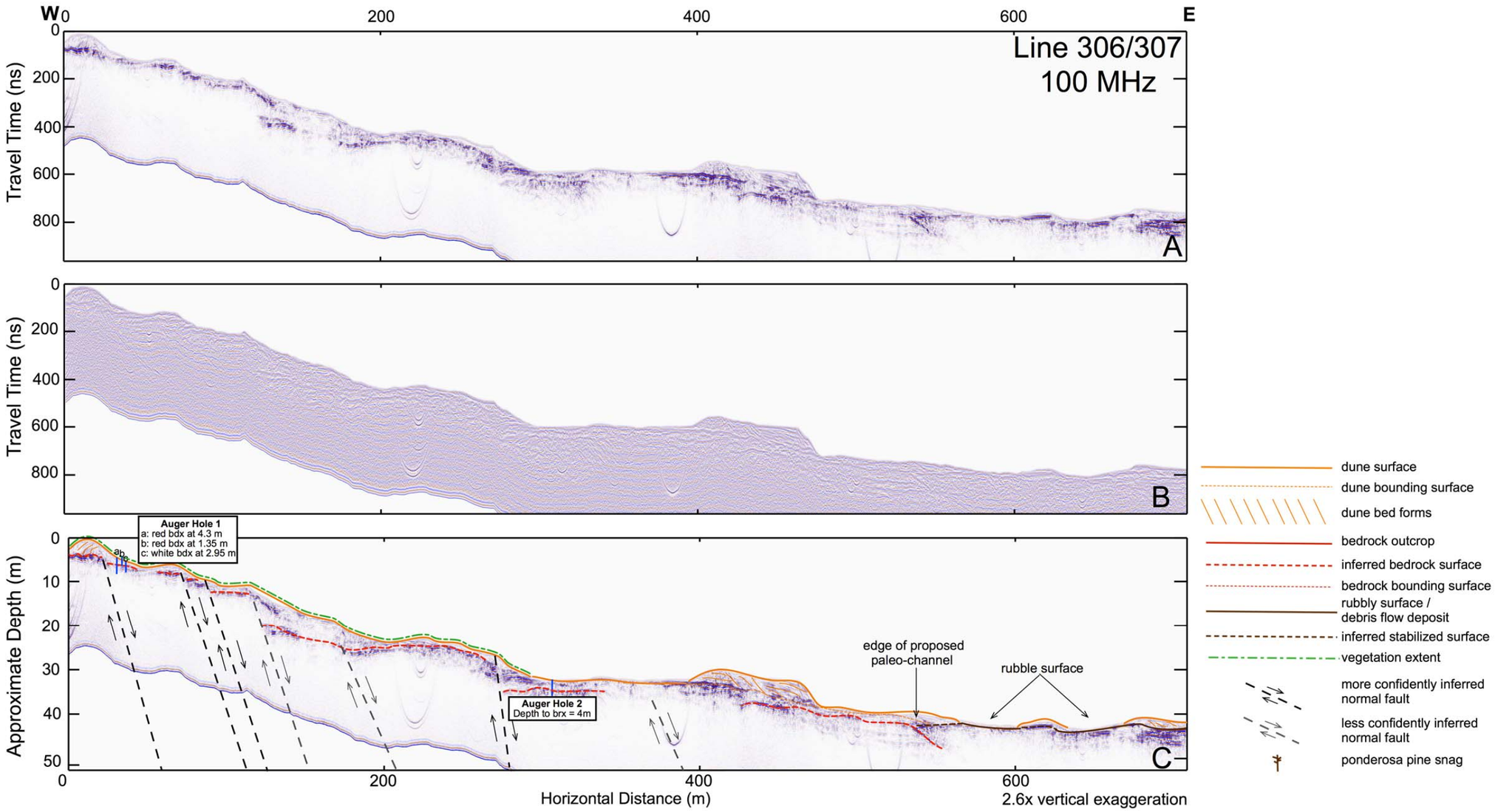

Figure 24: Processed and interpreted GPR data for Line 306/307 (see Figure 12). (A) Migrated data; (B) Migrated data with AGC applied; (C) Interpretation for Line 306/307 shows a series of antithetic faults that have an apparent dip of approximately 40° to the east. Fault interpretations are based on offset of the inferred bedrock surface as well as attenuation between these offset surfaces. Attenuation may occur where there has been accelerated weathering due to brecciation along the fault surface. Auger holes at the western edge of the transect indicate approximate depths of 2 meters to weathered bedrock and 4 meters to unweathered bedrock. An auger hole at 210 meters shows a depth of 4 meters to weathered bedrock. The bedrock drops off at 525 meters; this marks the western edge of the proposed paleo-channel. The rubble surface that outcrops in the eastern part of the transect and onlaps onto the bedrock represents a stabilized surface that likely formed during the Little Ice Age on top of a series of intercalated aeolian, fluvial, and colluvial channel fill sediments.

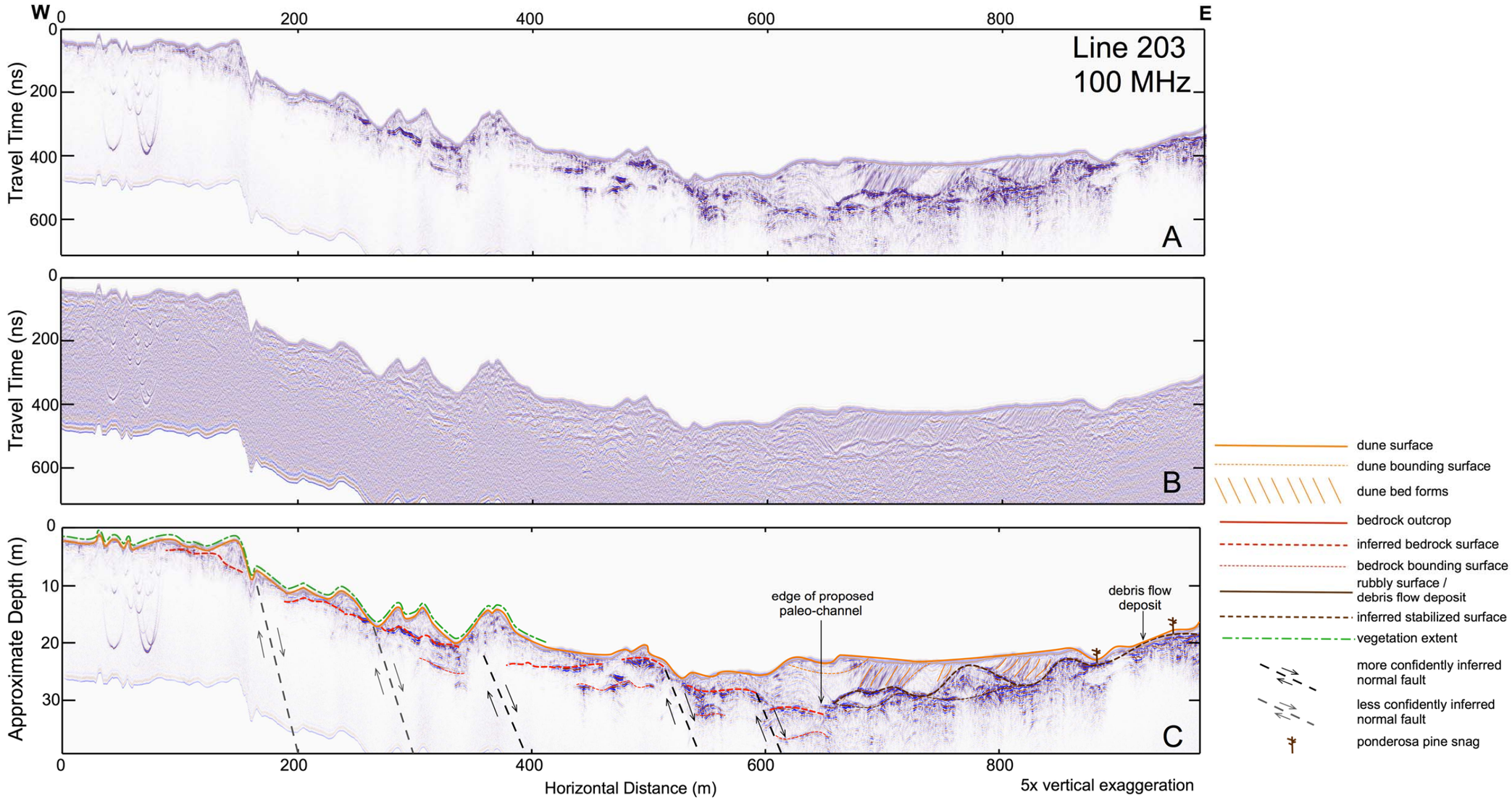

Figure 25: Processed and interpreted GPR data for Line 203 (see Figure 12). (A) Migrated data; (B) Migrated data with AGC applied; (C) Interpretation for Line 203 shows a series of antithetic faults that have an apparent dip of approximately 35° to the east. Fault interpretations are based on offset of the bedrock surface and internal bedrock reflectors as well as attenuation between these offset surfaces. Attenuation may occur where there has been accelerated weathering due to brecciation along the fault plane. Bedrock drops off at approximately 650 meters; this represents the western edge of the proposed paleo-channel. At the easternmost side of the transect, a debris flow deposit is visible at the surface and appears to bury at least two ponderosa snags. The base of the snags coincides with the inferred stabilized surface that formed during the Little Ice Age on top of a series of intercalated aeolian, fluvial, and colluvial sediments. The burial of the snags by debris flow deposits here and in other parts of the dune field indicates that these flows may have been responsible for the death of ponderosas that were established during the early Little Ice Age. It is also important to note that this transect shows much thicker active sand dunes in the core of the dune field than do transects further south.

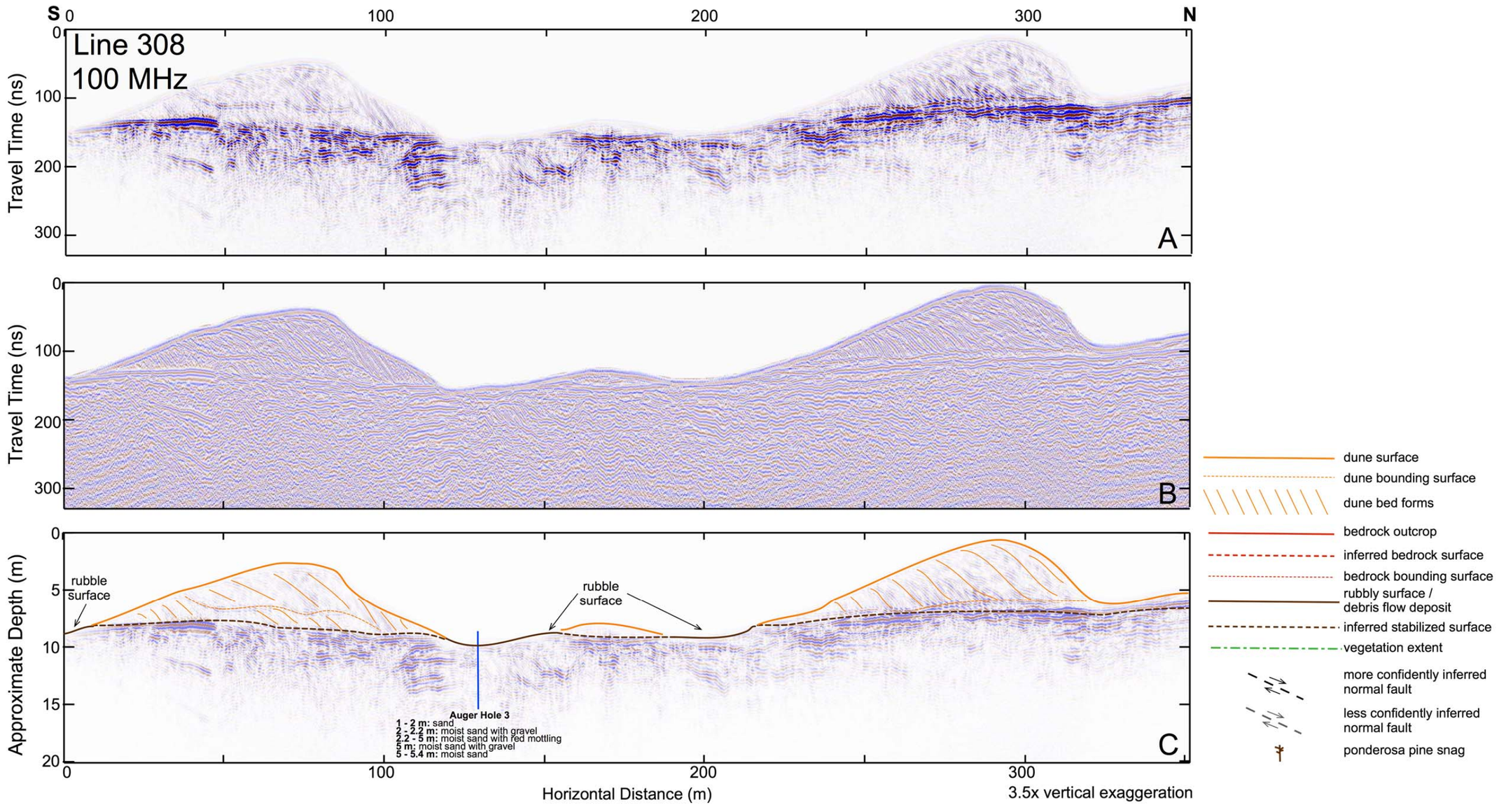

Figure 26: Processed and interpreted GPR data for Line 308 (see Figure 12). (A) Migrated data; (B) Migrated data with AGC applied; (C) Interpretation for Line 308 shows a continuous, south-dipping surface beneath the large transverse dunes in the core of the dune field. This surface is exposed in an interdune area at 125 meters as a dark, rubble surface. Augering into this surface reveals moist sand to at least 5.4 meters, with several layers of gravelly sand. These gravelly sand layers may cause the strong, sub-horizontal reflectors seen below the rubbly surface. This sandy deposit continues to a depth of at least 20 meters below the interdune surface, and likely represents a series of intercalated aeolian, fluvial, and colluvial sediments that filled the proposed paleo-channel. The top of these sediments represents a stabilized surface that likely formed during the Little Ice Age.

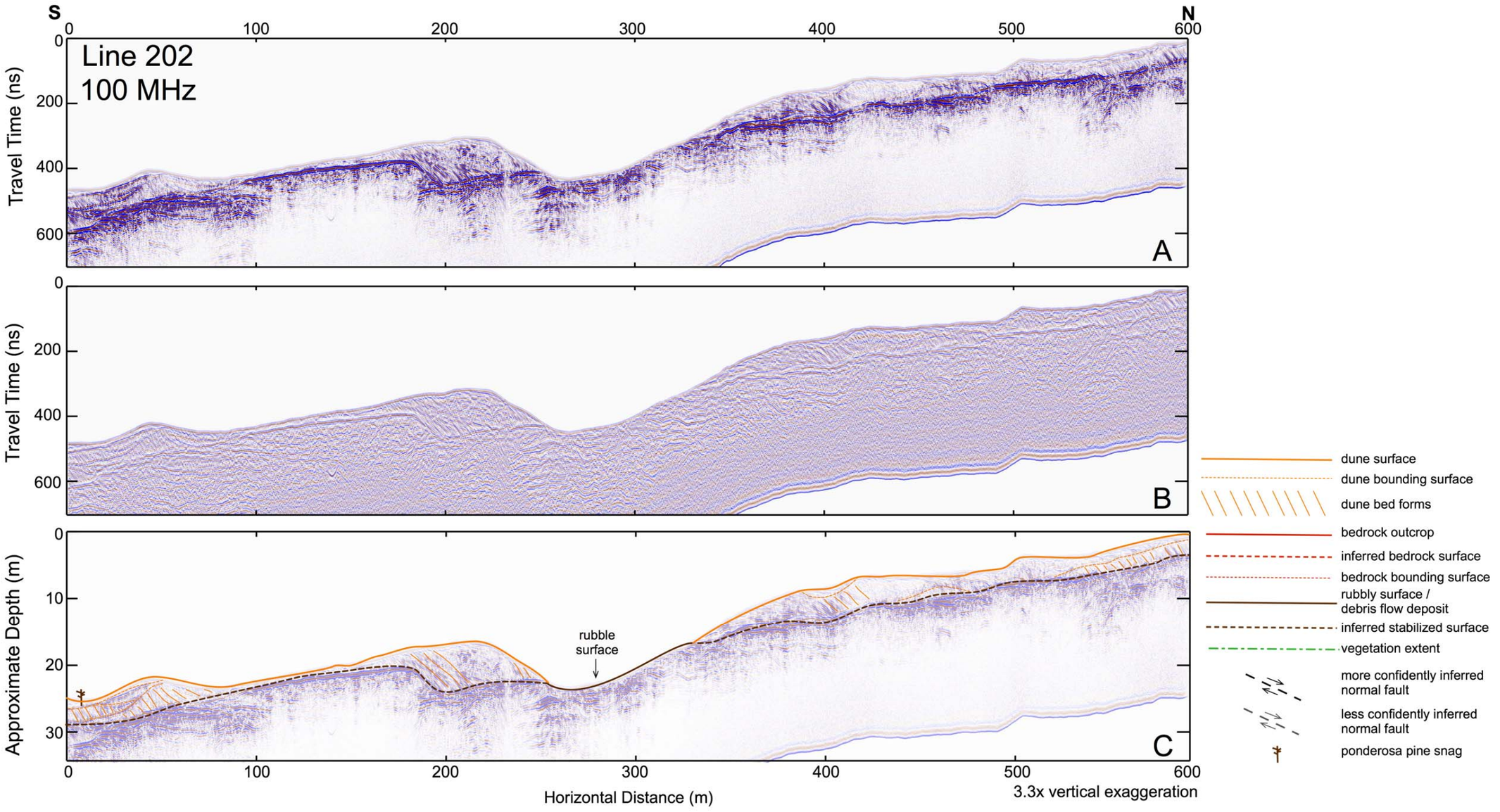

Figure 27: Processed and interpreted GPR data for Line 202 (see Figure 12). (A) Migrated data; (B) Migrated data with AGC applied; (C) Interpretation for Line 202 shows a continuous, south-dipping surface beneath the large transverse dunes in the core of the dune field. This surface is exposed in an interdune area from 250 – 320 meters as a dark, rubbly surface. This rubble surface represents a stabilized surface that likely formed during the Little Ice Age atop a series of intercalated aeolian, fluvial, and colluvial sediments that filled the proposed paleo-channel. At the southernmost end of the transect, a partially exposed ponderosa pine snag appears to be growing on a dune bounding surface.

to the west, the reflectors here are not chaotic and surfaces can easily be traced across the transect.

Two auger holes were used to determine depth to bedrock in the west dune field and one was used in the central core. Auger Holes 1a, 1b, and 1c (Figure 24) are located in the parabolics just east of the road, and show depths to weathered bedrock of approximately 2 meters and a depth to unweathered bedrock of approximately 4 meters. Differences between depths at the three holes probably occur because of variations in weathering patterns and the dipping nature of the reflector in this location. Auger Hole 2 (Figure 24) is located approximately 150 meters east of Auger Hole 1, near the boundary between the vegetated parabolics and the central core of the dune field, and reveals a depth to bedrock of 4 meters. Auger Hole 3 (Figure 26) is located in an interdune area in the central core of the dune field. This interdune area is characterized by the rubble surface seen in many interdune areas in this part of the dune field. The auger hole did not intersect bedrock within 5.4 meters of the surface. The substrate consisted primarily of moist sand, with lenses of sandy gravel.

4.3.3 North Dune Field

Based on the detrended surface model, I predicted that the paleotopography of the northern part of the dune field would be similar to that found along the western margin. Understanding paleotopography here is of particular importance because if there are antithetic faults, this is approximately where they would intersect the main trace of the Sevier.

Unfortunately, GPR was not able to add to our understanding of paleotopography in the north because of high attenuation of the EM signal, likely resulting from the

presence of silt or clay in the stabilized surface and debris flow deposits that form the substrate. Because the attenuation in these transects is so severe, the data are not presented here. The implications of this attenuation are discussed in Section 5.3.

CHAPTER FIVE: DISCUSSION

5.1 Paleotopography of South Dune Field

The paleotopography of the South Dune Field is distinct from that to the north and is characterized by generally thin sand cover in interdune areas, an intermittently elevated water table, a gradual decrease in elevation from west to east, and an anomalous bedrock knob. Although a perched water table was not directly observed, previous GPR surveys and augering, and the permeability contrast between the sand and underlying bedrock, indicate that such an occurrence is likely. Both the detrended surface model and GPR images support this interpretation, with the GPR providing a more accurate and detailed depiction of the bedrock knob and location of the intermittent water table surface. These features provide context for understanding the local wind regime, the depositional nature of the star dune and First Dune, paleodrainage, and the presence of atypical vegetation.

5.1.1 Bedrock Knob

Wilkins et al. (2003) suggest that the star dune likely formed as a result of a highly modified local wind regime affecting migrating transverse dune limbs. Those authors attribute this modified wind flow pattern to obstruction by an observed bedrock knob that forms the core of First Dune. Although the detrended model shows this knob exists just north of First Dune, GPR supports field observations that show that the bedrock knob actually forms the core of First Dune (Figures 16 and 17). The disparity between these methods is discussed in Section 5.7. Both methods, however, show that the detrended knob is asymmetrical, with a steeper eastern flank. I initially hypothesized that

this knob has a structural origin, but the GPR data do not show offset within the bedrock, indicating that this is instead an erosional feature.

5.1.1.1 Effect on Wind and Sediment Dynamics

First Dune and the star dune are among the largest dunes in the Lower Dune Field. The paleotopography of the southern dune field reveals that, despite their proximity and similarity in size, these two dunes formed as a result of very different sediment and wind dynamics.

Chase (2009) separates dunes into two types, accumulating dunes and migrating dunes, in order to guide interpretation of sediment OSL ages. Migrating dunes are those that constantly recycle sediment as they move downwind, such as the transverse and barchanoid ridges that dominate the active core of the CPSD. Accumulating or topographic dunes form when sediment moves from a high energy to low energy environment, thus accumulating sediment over time.

At the CPSD, the star dune likely forms as winds from the southwest interact with the bedrock knob, thus altering the unidirectional wind into a multidirectional regime that loses energy on the lee side of the knob. Wilkins et al. (2003) suggest that the degree to which First Dune has enveloped the bedrock knob may control when downwind transverse dunes merge to form a single star dune. Whereas the star dune is classified as an accumulating dune, First Dune is not really a dune at all. The bulk of First Dune is actually bedrock rather than accumulated sand. GPR images show that the flanks of First Dune have only a thin sand cover (Figures 16 and 17) and only the top 5 meters of the 20-meter tall topographic feature is comprised of aeolian sand (Figure 17).

5.1.1.2 Implications for Future OSL Dating

Understanding these wind and sedimentation dynamics is important for future utilization of OSL dating. I suggest that the star dune may be an ideal place to collect OSL samples because of its accumulating nature. However, it is important to note that the star dune has transitioned from several transverse dunes to a star dune and back numerous times, and thus some of the older sediments may have been recycled.

5.1.2 Paleodrainage

Modern topography, the detrended surface model, and GPR transects (Figures 16, 17, 18, and 19) indicate that bedrock in this part of the dune field slopes gradually down to the east. In this part of the dune field, Sand Wash is not perched like it is to the north, and the bedrock likely continues to gradually drop in elevation to the east of the extent of our GPR transects. This suggests that in this part of the dune field Sand Wash may not have migrated significantly from its original course, and the Sevier scarp is controlling its location. Therefore, despite my interpretation of the bedrock knob as an erosional feature, it is unlikely that it was formed by Sand Wash.

5.1.3 Perched Water Table

Although I did not directly observe the water table surface in the GPR imagery, based on the permeability contrast between the sand and underlying bedrock, I infer that there is an intermittently perched water table at the sand-bedrock interface (Figure 17). The presence of a this shallow water table is corroborated by additional GPR transects and auger holes collected by Clement et al. (2006) and by the field observations of wet sand at the surface in these areas.

Ford et al. (2010) suggest that anomalously low-elevation ponderosa in this part of the dune field are supported by sufficient effective moisture that is available as a result of southward flow of shallow groundwater within the rooting depth of the trees. Here I suggest that this southward flow, in combination with shallow bedrock and additional flow along the gradient from the west, causes this perched water table both to the east and south of the bedrock knob that sustains the growth of ponderosas at this low elevation.

5.2 Paleotopography of Western Dune Field and the Active Core

5.2.1 Faulting

Interpretations for GPR transects in the west dune field and central core are shown in Figures 21C – 27C. I interpret the stepping paleotopography of western margin to be indicative of a series of shallow, east-dipping normal antithetic faults. The location of faults was determined based on offset of strong bedrock reflectors (Figures 21 – 24), offset of reflectors within the bedrock (Figure 25), and attenuation between obvious bedrock reflectors (Figures 21 – 25). This attenuation may occur in places where there has been increased weathering because of brecciation or infill of fines along the fault plane. Faults interpreted based on clear offset are identified on Figures 21 – 27 as “more confidently inferred” (black dashed lines), whereas faults interpreted based on attenuation and/or alignment with faults in another transect are labeled as “less confidently inferred” (gray dashed lines). Estimated apparent dip ranges from 30° – 42°, but these values should be approached skeptically since clear offset is rare and faults may be imaged obliquely.

The linear dune ridge that forms the western boundary of the parabolics marks the western extent of this fault splay zone. The fault zone continues beneath the

parabolics and into the central core. In all transects, the bedrock drops dramatically at approximately the center of the dune field and is no longer visible in the imagery. It is unclear whether this drop off represents another fault or is an erosional feature. If it is structural in nature, this represents the greatest offset in the fault splay. Because the modern Sand Wash is perched above and outside this part of the dune field, it is proposed that this drop off represents a canyon or arroyo wall of a paleo-channel. If this is the case, the location of the paleo-channel in this part of the dune field is likely controlled by the location of the eastern most antithetic fault.

The western margin fault zone is characterized by four to six steps with thin, largely vegetated sand cover. The range in the number of steps represents lateral changes among individual fault strands that bifurcate and merge, creating a fault splay. This is verified by interpolation between the fault surface traces (Figure 28A), which, when translated to the ground surface (Figure 28B), illustrates an approximately 500-meter wide, anastomosing fault zone with a similar orientation to the antithetic faults mapped north of the Lower Dune Field.

Additional support for the presence of marginal faults comes from the presence of the upper, “white” section of the Navajo Formation within the dune field. As noted in Section 2.2.1.1, the contact between this “white” subunit and the underlying, less resistant “pale red” sandstone is visible along the western margin of the dune field, specifically in the western most outcrop shown on Line 200 (Figure 21). Since the pale red sandstone is less resistant, one might expect the slope below this contact to be shallower. Instead, there is a sharp increase in slope at the western edge of the dune field.

Furthermore, the “white” sandstone outcrops within the central core of the dune field in several places, despite being at a much lower elevation than the contact between the two

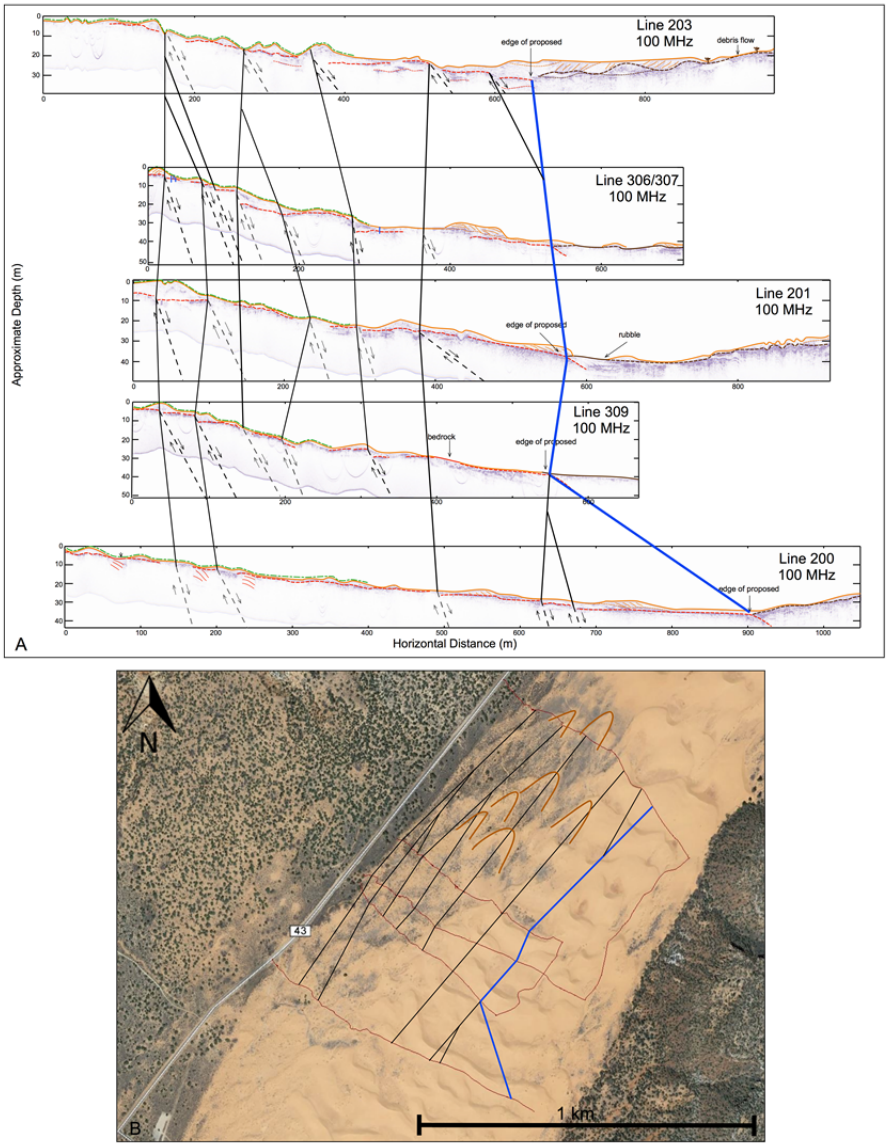

Figure 28: (A) Correlation of fault surfaces between GPR transects. (B) Surface interpretation of GPR transects shows a fault splay zone that is comprised of approximately 4 – 7 anastomosing fault strands that decrease in density as you move from west to east. Apexes of the parabolic dune forms (shown in orange) appear to coincide with the surface traces of the faults, indicating that the faults may be influencing the location of these dunes. The eastern-most fault splay corresponds to the location of the western edge of the proposed paleo-channel, indicating that the antithetic faults, rather than the main Sevier scarp, controls the location of the channel in this part of the dune field. The channel boundary curves to the east as you move to the south, indicating that to the south the location of the channel is controlled by the Sevier scarp.

units. The presence of faults helps to explain the presence of the "white" unit below the contact.

5.2.2 Paleodrainage

It is important to note that the western edge of the paleo-channel appears to shift to the east between Line 309 (Figure 22) and Line 200 (Figure 21). When the channel edge is traced onto the surface (Figure 28B), it becomes apparent that this turn to the east coincides with the transition from perched Sand Wash to the north with incised Sand Wash to the south, as well as the termination of the antithetic faults, since they are not observed in the southern part of the dune field. The location of the northern reach of the proposed paleo-channel was, therefore, controlled by antithetic faults, whereas the location of the southern reach of the paleo-channel was and still is controlled by the main Sevier trace.

5.2.3 Antecedent Surfaces

Figures 26 and 27 present interpretations for S-N trending GPR transects in the central core of the dune field. The dark, rubble surface that outcrops in many interdune areas in this part of the dune field is present in both of these transects. Auger Hole 3 (Figure 26) records a substrate beneath this surface consisting primarily of moist sand with lenses of sandy gravel that correspond with the sub-horizontal reflectors seen beneath the surface. The surface appears to be continuous beneath the dunes and likely represents the stable, Little Ice Age (LIA; AD 1440 – 1850) surface identified by Ford et al. (2010) in the north dune field. W-E oriented GPR transects (Figures 21 – 25) indicate that the stabilized surface onlaps onto bedrock at the edge of the proposed paleo-channel. In contrast to the faulted bedrock topography underlying the parabolic dunes to the west,

this stabilized surface forms the paleotopography on which the most active of the modern dunes formed.

I interpret this thick sand unit to represent channel fill consisting of intercalated fluvial, aeolian, and colluvial sediments deposited in the paleo-channel. The sediments may represent prior periods of aeolian activity, fluvial sands from paleo-Sand Wash, alluvial fan sediments and debris-flow deposits from canyons to the east, or a combination of some or all of these. GPR imagery of this substrate does not exhibit clear bedforms, suggesting that previous episodes of aeolian activity may not have been continuous across the extent of the dune field, or aeolian activity was primarily in the form of sand sheets.

During the LIA, the surface in the dune field stabilized as a result of a cooler climate with higher effective moisture. Ford et al. (2010) recorded this stabilized surface as an exhumed soil near the northern end of the central core of the dune field; this is likely the extension of that surface, or a similar surface from an earlier or contemporary episode of stability. Ford et al. (2010) also show that ponderosa were established in this part of the dune field during the LIA. GPR transects show that these trees, now partially exposed snags, grew on both the stabilized intercalated surface (Figure 25) and on dune bounding surfaces (Figure 27).

GPR imagery also traces the extent of mud and duff layers that outcrop in many interdune areas. These outcrops vary across the dune field; some are primarily sandy sheetflood deposits, while others contain larger sandstone clasts or cobbles and organic duff debris (Figure 29). In many places, these deposits appear to bury ponderosa snags and roots have been observed in several of the deposits. The presence of these deposits

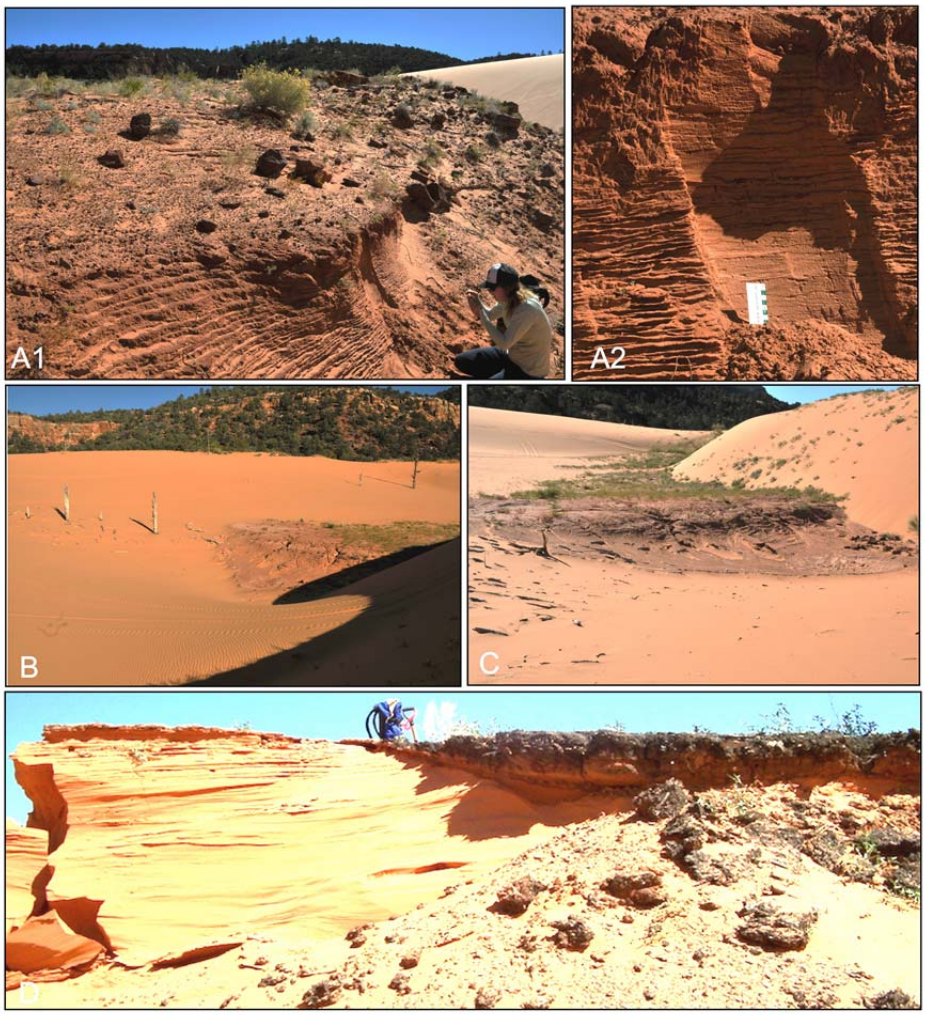

Figure 29: Debris flow, sheet flood, and soil deposits are found in many interdune areas. (A) Sandy sheet flood deposits covered with angular clasts. (B) Muddy deposit appears to bury partially exposed snags. (C) Muddy deposit with duff appears to be a debris flow deposit that buried ponderosa snags. (D) A Little Ice Age (LIA) soil was identified by Ford et al. (2010). Aeolian deposits beneath the soil date back to at least 4,000 years BP. These deposits form a continuous horizon beneath much of the core of the dune field and likely represent a stabilized surface, at least part of which formed during the Little Ice Age, that formed atop a series of intercalated aeolian, fluvial, and colluvial sediments. Further survey of these deposits is crucial to understanding the Holocene history of the dune field.

and their thicknesses vary across the central core of the dune field, and in some places show a hummocky surface (Figure 25). I interpret these deposits as debris flows sourced from the canyons to the east. A radiocarbon date from organic material in a duff layer above the LIA soil recorded by Wilkins et al. (2005) suggests that the soil formed in

470+/-50 BP, and the overlying duff was deposited in 200+/-40 BP (Ford et al., 2010), indicating the period of stability during the early LIA was followed by a period of debris flows during the middle-late LIA. Further dating of these deposits is required to determine whether or not the timing of these debris flows was contemporaneous. Based on the observation that many of these deposits appear to bury snags (Figures 25 and 29C), I propose that these debris flows may have been responsible for the death of some ponderosa during the middle of the LIA, rather than being inundated by aeolian activity as suggested by Ford et al. (2010).

It is also important to note that the stabilized LIA surface is present in interdune areas in the central and northern parts of the active core, but not in the southern. The transition between where the unit is visible and where it becomes absent occurs at approximately the same longitudinal position where slope in the detrended surface changes, where the sand apron intersects with the active dune field, and where Sand Wash transitions from being perched to the north to being incised to the south (Figure 30). This suggests that the dissected sand apron may be related to the sediments on which the LIA surface formed. Further investigation of the processes that formed these units is necessary to understand their paleoclimatic and geomorphic significance. The LIA surface has not been observed in the southern part of the dune field near First Dune and the star dune, but it is unclear if this part of the dune field remained active during the LIA or the stabilized surface is simply not preserved.

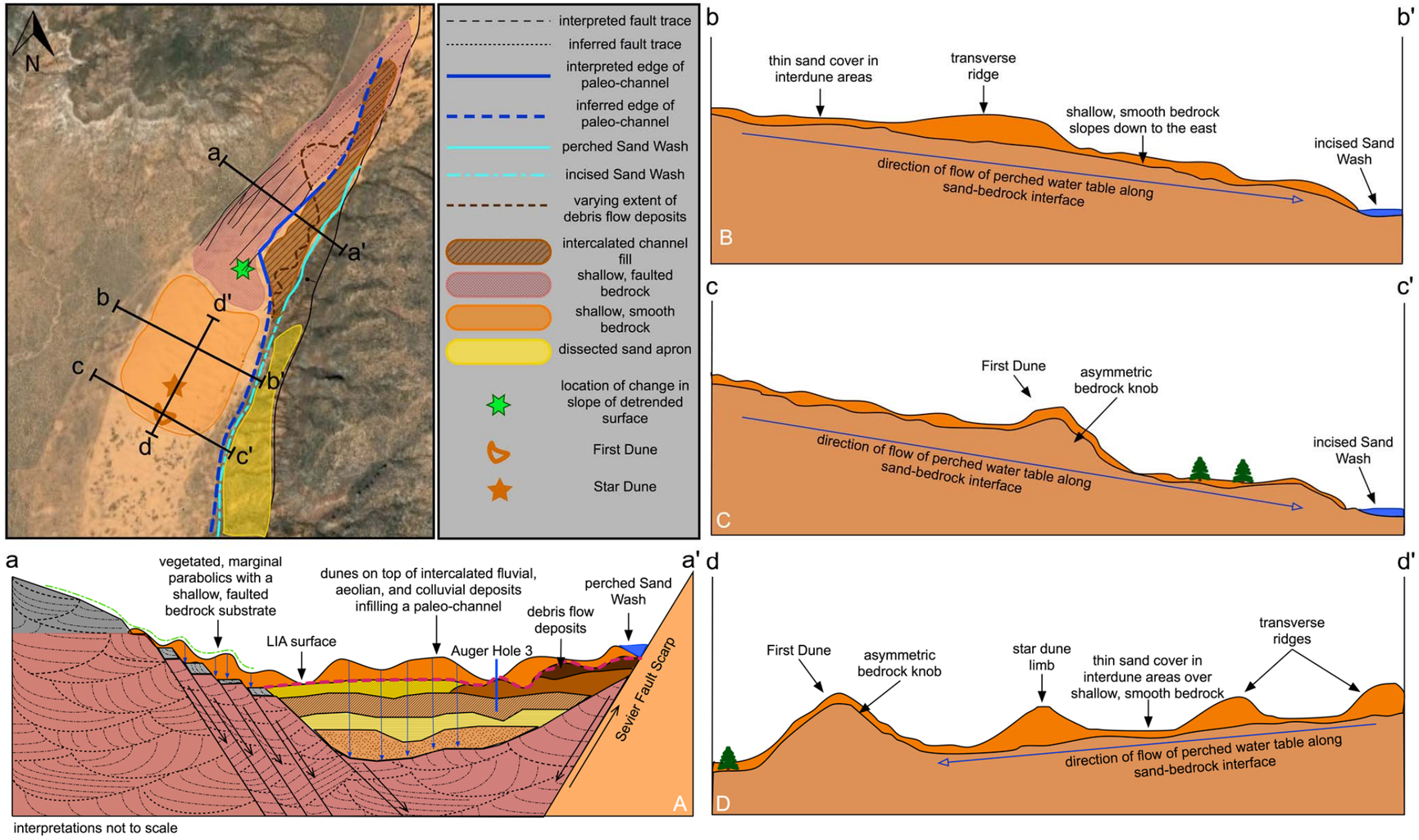

Figure 30: **Summary of paleosurfaces on which current dunes formed. These surfaces vary across the dune field and affect the resulting dune morphologies and activity. The southern dune field is underlain by shallow, smooth bedrock that slopes down to the south and east. The central core of the dune field is underlain by intercalated channel fill that acts as a secondary sediment source. The west dune field is underlain by shallow, faulted topography that limits sediment supply and increases plant available moisture. The north dune field is underlain by a combination of faulted bedrock and ubiquitous debris flow deposits that attenuate GPR signals. It is of interest to note that the transition from the perched northern reach Sand Wash to the incised southern reach, the change in longitudinal slope of the detrended surface, and the western turn of the proposed paleo-channel all occur at approximately the same place in the dune field. (A) A hypothetical cross section across the western dune field and central core shows the variation in the paleotopography and substrate. Blue arrows represent the depth to which precipitation can easily percolate. The high drainage efficiency of the central core causes interdune sediments to be drier, and thus more susceptible to recycling as a secondary sediment source. The lower drainage capacity of the substrate in the western dune field may increase effective plant available moisture, aiding in the stabilization of these dunes. (B) The bedrock beneath the south dune field generally slopes down to the southeast and is characterized by thin sand cover. (C) Beneath First Dune, there is an anomalous bedrock knob with a steeper eastern flank. (D) The bedrock beneath the south dune field generally slopes to the southeast (with the exception of the bedrock knob beneath First Dune). There is likely intermittent flow of water along a perched water table at the sand bedrock interface that allows water to move down gradient to the south east and support ponderosa in the south part of the dune field.**

5.3 Paleotopography of North Dune Field

Based on the detrended surface model, I predicted that the paleotopography of the northern part of the dune field would be similar to that found along the western margin. Understanding paleotopography here is of particular importance because if there are antithetic faults, this is approximately where they would intersect the Sevier. Unfortunately, GPR was not able to add to our understanding of paleotopography here because of high attenuation of the EM signal, likely resulting from the presence of silt or clay in the stabilized surface and debris flow deposits that form the substrate.

North of Line 304 (Figure 12), several W-E transects were conducted, but only a meter or two of penetration was achieved. This can be attributed to the abundance of outcropping muddy layers in this part of the dune field. These muddy layers are likely related to the stabilized surface discussed in Section 5.1.3, and are the cause of the high attenuation. The increased presence of attenuating muds and clays in this part of the dune field may indicate that there were more debris flows in this part of the dune field.

Even further north, between the road and the Sevier scarp, the sand among the sagebrush scrub has a distinctive gray color that can be attributed to broken down organic material. This fine-grained organic material may contribute to the high attenuation we see in these transects. Clay and silt sourced from the Lower Sinawava Member of the Temple Cap Formation, which occurs as a mudstone to silty sandstone along the cliffs of Esplin Point to the west, may also have moved into this area via slope transport contributing to the attenuation.

5.4 Sediment Source

The sediment source for the CPSD has been identified as sand that has been reworked and deposited in the washes in the Vermillion Cliffs west of the dune field (Wilkins and Ford, 2007) or from mixed alluvial and aeolian sands on the Moccasin Terrace to the southwest (Gregory, 1950; Ford et al., 2010). Although I do not refute that these upwind sources provide the bulk of sediment supply to dune field, here I suggest that the sandy, intercalated channel fill deposits that form the substrate beneath the central core of the active dune field provide a secondary sand source. This surface outcrops extensively in interdune areas in the central core of the dune field, and it seems reasonable that these unvegetated sands may be remobilized during low-moisture periods. Remobilization potential may be enhanced by the ability of this thick sand unit to efficiently drain any moisture it receives. This secondary source would help explain the continued mobility of the dunes throughout the last several decades despite the lack of obvious sediment influxes from upwind sources.

5.5 Using Paleotopography to Understand Boundary Conditions

5.5.1 Sediment Supply

Topographic profiles shown in Figure 15, as well as GPR transects in the western part of the dune field (Figures 21 – 27) show that in the active core of the dune field (Qetd on Figure 3), sand cover increases to the north and east. In the southern part of the dune field, sand depth is generally thinner than it is in the north and in many places is less than three meters thick. Wilkins and Ford (2007) show that between 1960 and 1997 dunes in the Lower Dune Field increased in both length and spacing, indicating a coeval increase in storage capacity. They suggest that this increase in sediment storage

represents an earlier sediment influx event, possibly caused by a late nineteenth-century drought, working its way through the system. The general increase in sediment depth from south to north supports this hypothesis.

Beneath the parabolics along the western margin of the dune field, sand thickness does not change from north to south and is generally much thinner than in the central core of the dune field. Hugenholtz et al. (2008) propose that sediment supply is the primary control on parabolic dune formation through feedbacks with vegetative cover. Parabolic dunes form and become stabilized when erosion-resistant substrates are encountered, limiting sediment supply and thus dune activity. Under sediment-supply-limited conditions, vegetation cover expands thus stabilizing the dunes. Based on this model, I suggest that the limited sediment supply, vegetation growth potential, and resulting parabolic dune forms in the western part of the dune field are a result of the lack of an additional, erodible substrate sand source such as is available in the central core of the dune field. Whereas dunes in the central core of the dune field are able to incorporate sand from the underlying sandy substrate as a secondary source, the parabolics on the western margin encounter bedrock and are thus supply limited.

Additionally, the high permeability of the underlying substrate in the central core of the dune field allows it to effectively drain any moisture it receives, limiting the potential for vegetation growth on this surface. This is in contrast to the chaotic, faulted bedrock substrate beneath the parabolics, which likely has a lower permeability than the intercalated channel fill sediments in the central core. The increased surface area of the faulted bedrock probably increases weathering depths, as was observed in Auger Hole 1 (Figure 24), and this weathered substrate, in combination with lower permeability of

unweathered bedrock beneath, provides higher effective moisture that supports the earlier noted dense plant growth.

Another compelling observation that can be made in the west dune field is that the apexes of the well-defined parabolic dunes appear to correspond to the location of the antithetic fault traces (Figure 28). It is unclear what the mechanism behind this sort of relationship might be, but it suggests that the topographic scarp features may directly influence the location of individual parabolics.

5.5.2 Areal Limits

Areal limits is a dune-field-scale boundary condition defined by the geomorphic container in which the dune pattern develops (Ewing and Kocurek, 2010). Ewing and Kocurek (2010) show that areal limits affect patterning by limiting dune-dune interactions that can occur in a given area, and have modeled dune pattern response to changing dune field size. These models predict that dune fields experience maximum possible spacing when the dune field width to dune field stream-wise length ratio is 1:5, and that dune field length may have a stronger control on patterning than cross-dune field width.

The Lower Dune Field of the CPSD has a width to length ratio of almost exactly 1:5, with the average width at 1.1 km and a length of approximately 5 km from the southern part of the stabilized sand sheet (unit Qes on Figure 3) to where the dunes begin their climb up the Sevier scarp. The graben defined by the Sevier escarpment to the east and topography related to antithetic fault scarps on the western margin restrict the width of the dune field and thus define the extent of the geomorphic container for the CPSD.

Because the width to length ratio of the dune field is 1:5, it is likely that the CPSD are at or approaching a steady state in which dune-crest spacing and lengths are at a maximum.

5.5.3 Localized Wind Regimes

The topography surrounding the CPSD enhances wind flow in the active core of the dune field. This occurs as a result of a funneling effect as wind is forced into a more confined cross-valley width. Such an effect may help explain why the dunes in the active core and upwind parts of the dune field are more active than other parts of the dune field.

Additionally, topography within the dune field can cause local deviation from this valley-scale flow. As discussed in Section 5.2.1, the bedrock knob that forms the core of First Dune plays a large role in modifying the local wind flow pattern in the southern part of the dune field. As discussed earlier, this bedrock knob is asymmetrical, with a steeper east side. By defining the shape and size of this feature, it may be possible for future studies to model the modified wind regime that is responsible for formation of the star dune, and explore further how the wind regime is modified due to inundation by First Dune.

Other local variations in the wind flow occur along the eastern margin of the dune field where echo dunes form against the Sevier escarpment. Echo dunes occur when the wind direction is perpendicular to a topographic obstacle, creating a localized vortex on the downwind side of the dune between the slip face and the obstacle (Ford et al., 2010). Because the main wind regime at the CPSD interacts obliquely with the Sevier scarp, there must be some modification of the wind regime that allows the formation of these echo dunes.

5.6 Using Paleotopography to Understand Paleoclimate

The paleotopography for the central core of the dune field is defined by the stabilized LIA surface and the debris flow deposits that overlay parts of that surface. This provides context for further exploring climate of the western Colorado Plateau during the LIA, as well as defining a boundary for pre-LIA sediments. Although this work does not investigate pre-LIA climate signals, I suggest that the dissected sand apron east of Sand Wash in the southern part of the dune field is an ideal place to investigate these signals in future studies. OSL dates from elsewhere in the dune field show that there has been aeolian activity at the CPSD back to at least 4,000 years B.P. (Ford et al., 2010), but further work is needed to unravel this history.

What this work does add to our understanding of paleoclimate at the CPSD, and the western Colorado Plateau in general, is that the stabilized LIA surface is laterally extensive across the western and northern dune field, as evidenced by continuous reflectors in the GPR imagery. This stabilized surface resulted from a cooler and drier climate and supported vegetation, likely creating a positive feedback that further limited sediment availability and diminished aeolian transport. Studies of arroyo incision and aggradation in nearby drainages (Ely, 1997; Hereford, 2002; Summa-Nelson and Rittenour, 2011) support this interpretation of a cool, dry climate, although it is likely that the effective moisture of the dune field and surrounding region actually increased because of decreased evaporation. Further examination of the stabilized LIA surface, debris flow deposits, and underlying pre-LIA sediments, would reveal the effect this climate had on landscape evolution within the dune field.

The mechanism for large-volume debris flows during the LIA may be related to the flushing of debris out of side canyons during large storm events in a time that was otherwise drier than present. Studies by Ely (1997), Harden et al. (2010), Harvey et al. (2011), and others have used slackwater deposits and cut-fill cycles to link flood events to climate cycles on the Colorado Plateau. However, the temporal resolution of these chronologies is relatively coarse, and understanding the timing of debris flow events in the dune field may help to clarify the details of these cycles.

An alternative theory for the source of these deposits is that, rather than being sourced from the canyons to the east, these deposits may represent catastrophic events such as draining of dune-dammed lakes in, or north of, the Lower Dune Field. Such catastrophic events would make sense because many of these deposits partially bury ponderosa snags, indicating that they were coeval, and inundation may be responsible for the death of trees in this part of the dune field.

5.7 Comparison of Detrended Surface and Subsurface Imagery

I tested the accuracy of the detrended surface model by comparing topographic profiles along GPR transects to the interpreted GPR images. Topographic profile comparisons for select transects are shown in Figure 31 and differences between the detrended surface and interpreted bedrock or stabilized LIA surfaces (i.e., antecedent topography) are shown in Table 1.

In the south dune field, the mean difference between the detrended surface and interpreted bedrock surface ranges from 1.6 – 7.6 meters (Table 1), with the greatest differences occurring in transects that cross First Dune (Figure 31A), and lesser differences occurring to the north of First Dune (Figure 31B). In the west dune field, the

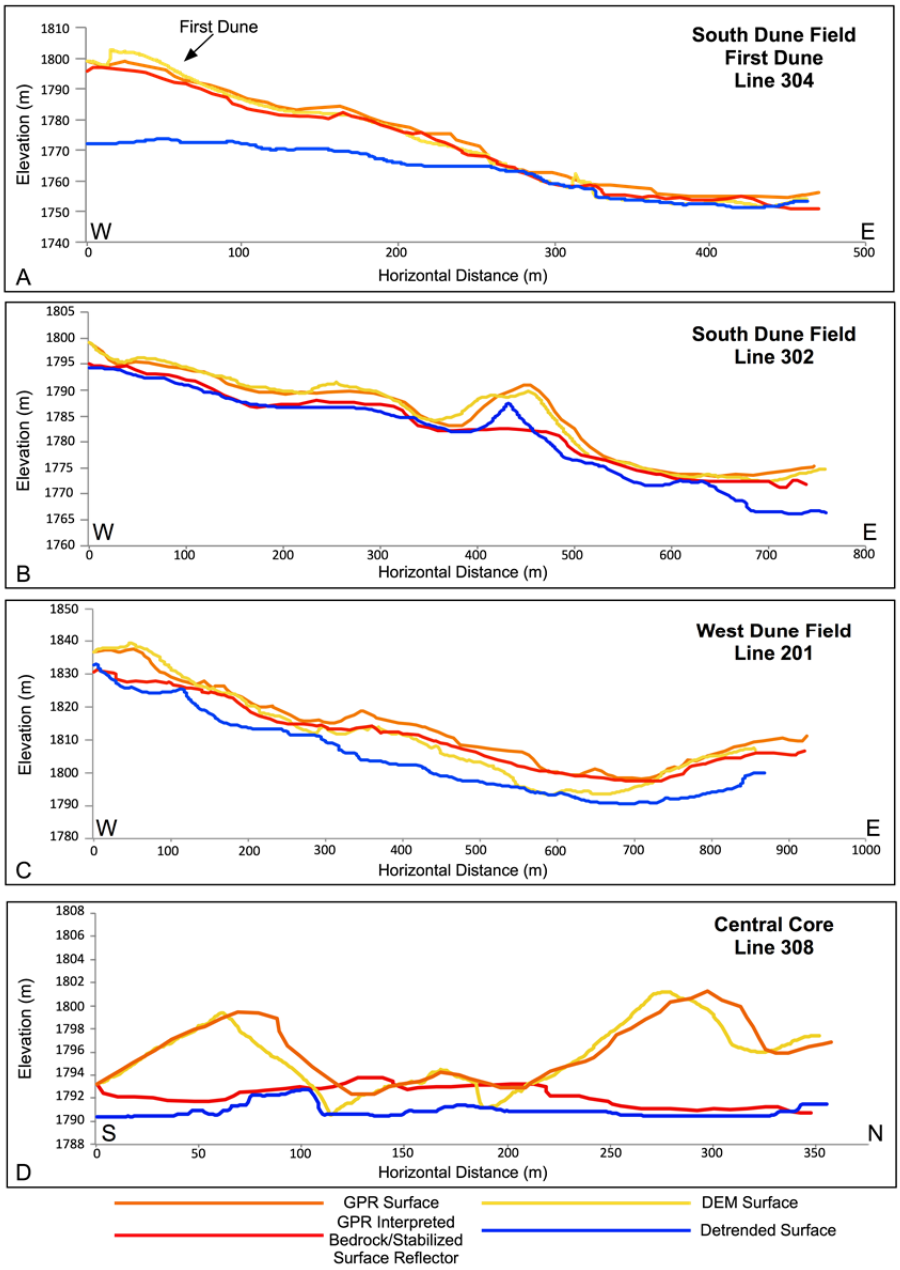

Figure 31: Comparison of the detrended surface and interpreted GPR imagery shows that the antecedent topography shows similar trends for both methods. In general, the detrended surface is slightly lower in elevation than the actual antecedent topography. Agreement is generally closest in the south dune field (B), with the exception of the area immediately surrounding First Dune (A). This inaccuracy occurs because the detrending method assumes that the antecedent surface is below dune base, and First Dune formed on top of an anomalous bedrock knob. Offset between the surfaces in the west dune field (C) is variable, likely as a result of noise in the DEM caused by errors in the vegetation height filter. In the central core of the dune field, (D), the detrended surface is similar to that of the stabilized LIA surface, showing that the detrended surface predicts the surface on which the most recent period of dune activity formed, rather than the bedrock.

mean difference ranges from 5.0 – 9.9 meters (Table 1 and Figure 31C) and in the central core of the dune field mean differences range from 0.9 – 1.7 meters (Table 1 and Figure 31D).

The detrended surface beneath First Dune (Figure 31A) is an exception to the relatively high accuracy (less than 3.6 meters mean difference) seen throughout the rest of the south dune field (Figure 31B and Table 1). The detrended model places the detrended surface up to 27.4 meters below the crest of First Dune (Table 1). However, field observations, validated by GPR data, show that bedrock actually outcrops near the crest of First Dune. This discrepancy between the detrended model and field observations occurs because the model assumes that the bedrock surface is at or below dune base. This assumption is accurate for most dunes at the CPSD, but because First Dune is actually a cover sand overlying the top of a topographically anomalous bedrock knob (making the name First "Dune" a bit of a misnomer), it is a special case.

Table 1: Comparison of Detrended Surface and Interpreted GPR Reflector Surface Elevations

	GPR Line Number	Mean Difference (m)	Standard Deviation (m)	Maximum Difference (m)	Minimum Difference (m)
South Dune Field	304	7.6	7.3	23.9	0.0
	305	7.1	9.8	27.4	0.0
	303	1.9	1.2	4.4	0.0
	302	1.6	1.5	6.5	0.0
	300/301	3.6	1.5	7.7	0.0
West Dune Field	200	7.1	2.5	16.8	1.3
	309	7.1	1.8	10.2	2.6
	201	6.4	2.6	10.6	0.0
	306/307	5.0	2.5	9.0	0.3
	203	9.9	4.0	18.0	2.7
Central Core	308	1.4	0.9	3.5	0.0
	202	8.1	3.0	14.8	2.5

Other than in the First Dune region of the dune field, the largest discrepancies between the detrended surface and the interpreted GPR paleosurface occur in the west dune field (Table 1). This part of the dune field is the most highly vegetated, and therefore inaccuracies in the DEM surface resulting from imperfect height filtering techniques are likely highest here. These inaccuracies may cause local noise in the elevation data that is reflected in the detrended surface. This is confirmed by comparison of the DEM surface elevations with the GPR surface elevations (Table 2), which shows that the west dune field indeed has the highest mean difference values for these surface elevations. This noise in the west dune field surface, in combination with the somewhat chaotic nature of the underlying bedrock is likely responsible for these higher discrepancies.

Table 2: Comparison of DEM Ground Surface and GPR Ground Surface Elevations

	GPR Line Number	Mean Difference (m)	Standard Deviation (m)	Maximum Difference (m)	Minimum Difference (m)*
South Dune Field	304	2.0	1.2	4.7	0
	305	1.2	0.8	4.4	0
	303	1.2	1.1	5.0	0
	302	0.8	0.7	3.0	0
	300/301	2.3	1.3	4.9	0
West Dune Field	200	3.0	1.5	6.9	0
	309	3.2	1.7	6.9	0
	201	3.3	2.4	10.6	0
	306/307	7.3	2.5	12.7	0
	203	4.0	2.5	10.6	0
Central Core	308	0.9	1.0	3.7	0
	202	1.7	1.3	5.7	0

*Initial elevations for GPR profiles were based on the DEM elevation – therefore, all transects show a minimum difference of 0 meters.

Other small errors in the detrended surface model are common. It should be noted that the GPR interpretations of underlying surfaces are not necessarily representative of

"true" surfaces, since their depth depends on an empirical, estimated velocity. Additionally, discrepancies could be the result of differences in accuracy and resolution. The GPS for the GPR unit, the source for our elevation measurements, has a vertical field accuracy of +/-30 cm. The accuracy of the horizontal position depends on continuous contact by the wheel attached to the sled apparatus with the ground surface, and can be compromised when steep topography or thick vegetation is encountered. Also, the DEMs are gridded to 1-m and 5-m resolutions, respectively; this is representative of their resolution and not their accuracy—further discussion of accuracy will be presented in Section 5.8.1.

5.8 Limitations

5.8.1 Accuracy of DEMs

Despite best efforts to image all interdune areas with the TLS, some areas were not well captured and therefore the DEMs may not accurately represent the elevation in these areas. This problem is especially problematic where the scanner was not able to see into Sand Wash and some interdune areas on the east side of the dune field. Additional error in the DEMs comes from imperfect performance of the vegetation height filter. A low-pass smoothing filter helps remove some of this noise caused by vegetation, but it is unclear what its effect is on overall accuracy.

A comparison of DEM and GPR surface elevations is shown in Table 2. The mean difference in these surface elevations ranges from 0.8 meters in the south dune field to 7.3 meters in the west dune field (Table 2). One might expect that, because these data were collected over two months apart (TLS in March, 2014 and GPR in June, 2014), surface elevation variation should be the greatest in the active south dune field and

central core as a result of seasonal changes and lowest in the west dune field where dunes are more stable. Instead, these data show the opposite trend; elevations are most similar in the south dune field and central core and vary the most in the west dune field. This discrepancy likely occurs because of imperfect vegetation height filtering techniques in the densely-vegetated west dune field that create noise in the DEM. In order to truly quantify the accuracy of DEMs created from TLS at this scale, a grid of GPS transects should be acquired at the same time as the TLS data and compared to the same transects extracted from the TLS-derived DEM.

5.8.2 Accuracy of GPR

The accuracy of GPR imagery interpretation depends on the accuracy of the GPS and horizontal measurement wheel, the GPR frequency, and the estimated velocity of the EM waves in the substrate. The frequencies used here, 50 MHz and 100 MHz, should be able to achieve a vertical resolution of 0.7 m and 0.35 m, respectively, so it is important to note that features smaller than these may not be represented in the imagery. Also important to note is that the estimated single velocity of 0.11 m/ns is an estimate; velocity is an averaged value for both the sand and the bedrock, but it is likely that EM travels at different speeds through these different mediums. This may affect the interpreted depth at which features are identified below the surface. Lastly, the GPS used to record the GPR transects has a vertical field accuracy of +/- 30 cm, which may also influence the depth at which features are identified. The processing applied to the GPR data also applies a smoothing function to the elevation data, which helps eliminate random GPS errors, but may also affect the overall accuracy of the transect locations.

5.9 Future Work

5.9.1 Expand Geophysical Survey

The GPR survey described in this work utilized low frequency antennas to maximize the likelihood of imaging the bedrock surface beneath the dunes. Despite using these low frequencies, we were not able to image the bedrock east of the central core of the dune field beneath the channel fill deposits. Additional geophysical techniques such as seismic or gravity may be useful in imaging to the necessary depth in these areas, and an expanded survey of the Sand Wash area may allow us to connect the bedrock surface beneath the dune field to where it intersects the Sevier. Imaging to this depth would help test the hypothesis I propose here of a deeper, incised paleo-channel that is located to the west of its current location in the central core of the dune field.

5.9.2 Observation and Dating of LIA Surface and Debris Flow Deposits

Here I propose that the stabilized LIA surface defined by Wilkins et al. (2005) and overlying debris-flow deposits comprise the paleosurface on which the transverse and barchanoid ridge dunes in the active core of the dune field formed. In order to resolve whether the surface and underlying deposits are contemporaneous or diachronous across the dune field, they need to be surveyed, mapped, and dated. This could be accomplished through examination of trenches dug in the sand-apron unit on the eastern side of the dune field, or through coring where the surface outcrops in the interdune areas. Ages could then be linked to climate chronologies and cycles of flooding that have already been established for the Colorado Plateau (Ely, 1997; Salzer and Kipfmueller, 2005; Harden et al., 2010; Harvey et al., 2011; Summa-Nelson and Rittenour, 2011).

5.9.3 Future Applications of Boundary Conditions

The fault scarps on the western margin of the dune field provide limits for the geomorphic container in which the dune field has developed and provide the boundary condition of areal limits. Understanding how the idea of areal limits applies to the CPSD could be expanded through modeling efforts based on methods by Ewing and Kocurek (2010). The information discussed here could also be applied to other newly recognized boundary conditions such as sediment source geometry (Ewing, 2009; Ewing and Kocurek, 2010).

5.9.4 TLS Methods

TLS was an effective method for creating a DEM with high accuracy and resolution to create a detrended surface model. TLS-derived DEMs have the potential to be applied to numerous other applications. DEMs created without applying the vegetation height filter could be used to determine surface roughness caused by vegetation and dune forms, which may be useful for modeling pattern formation. Additionally, repeat collection of TLS data could be used to track changes in vegetation cover, dune patterning, and interdune deflation over time. Although TLS was not ideal for picking up all interdune areas, we were able to image all dune crests, and therefore should be able to track their motion over time. Before such a repeat project is completed, however, an accuracy assessment of the TLS-derived DEMs should be completed. This could be done by collecting GPS elevation transects in a grid across the scanned surface within a day or two of TLS scanning (to minimize changes to the dunes), and comparing the GPS transects to identical transects that are extracted from the TLS-derived DEM.

CHAPTER 6: CONCLUSIONS

6.1 Antecedent Topography of the CPSD

Based on the TLS-derived detrended surface and GPR subsurface imagery, I propose that, as hypothesized, the CPSD are housed in a north-south-trending graben. This graben is bounded on the east by the Sevier scarp, and on the west by a series of previously unrecognized antithetic faults, and creates a highly-localized topographic basin, which in turn provided the "accommodation space" for sediment deposition and preservation in the central core of the dune field. The presence of this graben creates variability in the paleotopography and substrate characteristics across the dune field that corresponds to variations in morphology and patterning (Figure 30). These relationships show that understanding the geomorphic context of preexisting topography is crucial for accurate interpretation of paleoclimatic signals.

6.2 Paleotopography and Its Effect on Dune Morphology

The current episode of dune activity formed on a surface with variable topographic and substrate characteristics (Figure 30). The southern dune field rests on a shallow bedrock surface that slopes gently down to the east and south (Figure 30B/D). This surface is generally smooth, with an anomalous bedrock knob that marks the edge of a sharp drop in topography down to the east (Figure 30C). This shallow, sloping bedrock is likely responsible for the perched water table in this part of the dune field that makes it possible for continued growth and establishment of stands of ponderosa in the stabilized dunes further south. The history of this surface is unclear, since there is no evidence for

LIA stabilization in this part of the dune field. It is possible that this part of the dune field remained active during the LIA or that stabilization is simply not preserved due to the lack of accommodation space as is available in the central core to the north.

Paleotopography in the active core of the dune field generally slopes down to the south, with an abrupt decrease in gradient at approximately half the longitudinal length of the dune field. This surface is characterized by thick, intercalated channel-fill sediments capped in places by debris-flow deposits (Figure 30A). The surface of these deposits represents a stabilized surface that formed during the LIA as a result of a cooler climate and higher effective moisture corresponding with the establishment of stands of ponderosa. It is unclear what depositional process is responsible for the 15 – 20+-meter-thick sand unit below the stabilized surface, but it is proposed to be a combination of aeolian, colluvial, and fluvial sediment fill that was deposited in a paleo-channel.

The paleotopography of the western margin of the dune field is characterized by a series of bedrock steps created by offset of east-dipping antithetic faults (Figure 30A). The largest of these steps, with a drop of over 15 meters to the east, occurs approximately 200 meters east of the boundary between the parabolics and the active central core. This drop is likely erosional, but influenced by structural controls, and may represent the western bank of the proposed paleo-channel. Beyond this point, the bedrock surface is no longer visible in GPR imagery, and it is unclear where the bedrock intersects with the Sevier scarp. This channel and the surrounding bedrock topography may represent the paleotopography of the landscape prior to initial aeolian activity.

The thick, intercalated channel fill present in the proposed paleo-channel likely act as an additional source of sand for the central core of the dune field. The transport

potential of these sediments is probably increased by their ability to efficiently drain surface moisture (Figure 30A). In contrast, the substrate beneath the parabolics is comprised of shallow, weathered bedrock. The presence of a shallow, erosion-resistant substrate causes this part of the dune field to be sediment starved, leading to an increased potential for stabilizing vegetation to be established. This potential may be compounded by the lower drainage capacity of the bedrock substrate, increasing near-surface plant-available moisture. Unlike the south dune field, which also has a shallow bedrock substrate, the antithetic faults in this part of the dune field cause the fractured bedrock surface to be somewhat chaotic in nature, increasing weathering and soil development potential (Figure 30A).

6.3 The Story So Far

The Holocene history of the dune field is still largely unresolved. Evidence suggests that the bedrock surface beneath the central core of the dune field contains an arroyo-like feature, presumably representing a paleo-channel and the oldest paleo-surface on which dunes may have formed. A structural control for the wash is proposed, based on the presence of both the Sevier scarp in the south and newly identified antithetic faults in the north, but age of incision of the wash is unknown. Constraining this age in the future may be useful for providing a minimum age for offset of the antithetic faults.

Timing of incision and subsequent infill of the channel is unclear. Based on stratigraphic and chronometric analysis of other washes in the region (Hereford, 2002; Summa-Nelson and Rittenour, 2011), it appears similar local channels have undergone multiple phases of aggradation and incision since the last glacial, and it is therefore probable that this wash has a similarly complex history. Luminescence dates from upper

pre-LIA aeolian sediments suggest that aeolian activity has been at least intermittently present in the dune field for at least 4,000 years (Ford et al., 2010), but reconstructing a better-resolved alluvial and aeolian history will require many more such dates.

The LIA is defined here as a period of stability at the CPSD, allowing establishment of ponderosa in the central core of the dune field for at least 200 years, and establishment of ponderosa in the southern dune field that continues through the present. Ponderosa in the central core of the dune field were not able to survive through the second half of the LIA; their mortality resulted from inundation by debris flows and/or renewed aeolian activity. Careful analysis of the LIA surface, related debris flow deposits, and the dendrochronological record is needed to produce a decadal-scale climate history for this part of the LIA.

Since the termination of the LIA at the end of the 19th century, aeolian activity has resumed in the central core of the dune field. Pulses of sediment released and made available during the droughts of the 19th and 20th centuries, in combination with sediment provided by the sandy substrate, provide sources for the increasingly voluminous downwind dunes in the active core of the dune field.

It is unclear what the west dune field was like during the LIA, but encroachment of vegetation along this margin has diminished sediment availability. In the southern dune field, reduced availability of sediment over the last several decades has decreased sediment availability upwind of the active core of the dune field. The active core of the dune field likely remains active as a result of the additional sandy substrate source material and topographically enhanced wind flow.

6.4 Using TLS to Create a Detrended Model

Ground-based LiDAR is an effective tool for creating high-resolution DEMs for dune fields on the scale of the CPSD. This method is a viable alternative to prohibitively expensive and scheduling constrained ALSM LiDAR for relatively small-scale dune fields. With a small field team of 5 people, I was able to collect the necessary data for a 5 km^2 area in only three days. With more time, there is potential to collect high-density data for a much larger area. This technique could also be applied to create repeat imagery in order to track changes in dune migration, vegetation cover, interdune deflation, sediment storage capacity, and patterning over time. Although the resulting DEMs are not a perfect representation of the dune field surface as a result of missing data and imperfect filtering techniques, they still proved more than adequate for creating a detrended surface model of the underlying topography. Although accuracy is lower in some interdune areas, dune crests are well represented in the DEMs, demonstrating that these DEMs are ideal for examining temporal changes in patterning.

REFERENCES

Anderson, R.E., and Christenson, G.E., 1989, Quaternary faults, folds, and selected volcanic features in the Cedar City 1degx2deg quadrangle, Utah: Utah Geological and Mineral Survey Miscellaneous Publication 89-6, p. 1-29.

Baker, G. S., Jordan, T. E., and Pardy, J., 2007, An introduction to ground-penetrating radar (GPR): Special Paper - Geological Society of America, v. 432, p. 1-18.

Barchyn, T.E., and Hugenholtz, C.H., 2012, Aeolian dune field geomorphology modulates the stabilization rate imposed by climate: Journal of Geophysical Research, v. 117, June, p. 1-16, doi: 10.1029/2011JF002274.

Barchyn, T.E., and Hugenholtz, C.H., 2013, Reactivation of supply-limited dune fields from blowouts: A conceptual framework for state characterization: Geomorphology, v. 201, p. 172–182, doi: 10.1016/j.geomorph.2013.06.019.

Betancourt, J. L., 1990, Late Quaternary biogeography of the Colorado Plateau *in* Betancourt J. L., Van Devender T. R. and Martin P. S., eds., Packrat middens — the last 40,000 years of biotic change, University of Arizona Press, Tucson, AZ.

Bishop, M. A., 2013, Dune field development, interactions and boundary conditions for crescentic and stellate megadunes of the Al Liwa Basin, the Empty Quarter: Earth Surface Processes and Landforms, v. 38, no. 2, p. 183–191, doi: 10.1002/esp.3318.

Botha, G.A., Bristow, C.S., Porat, N., Duller, G., Armitage, S.J., Roberts, H.M., Clarke, B.M., Kota, M.W., and Schoeman, P., 2003, Evidence for dune reactivation from GPR profiles on the Maputaland coastal plain, South Africa, *in* Bristow, C.S. and Jol, H.M., eds., Ground Penetrating Radar in Sediments: Geological Society Special Publication 211, London, The Geological Society, p. 29-45.

Bristow, C.S., and Jol, H.M., 2003, An introduction to ground penetrating radar (GPR) in sediments, *in* Bristow, C.S. and Jol, H.M., eds., Ground Penetrating Radar in Sediments: Geological Society Special Publication 211, London, The Geological Society, p. 1-7.

Brumbaugh, D.S., 2008, Seismicity and active faulting of the Kanab-Fredonia area of the southern Colorado Plateau: Journal of Geophysical Research, v. 113, p. 1-9, doi: 10.1029/2007JB005278.

Chase, B.M., 2009, Evaluating the use of dune sediments as a proxy for palaeo-aridity: A southern African case study: Earth-Science Reviews, v. 93, no. 1-2, p. 31–45, doi: 10.1016/j.earscirev.2008.12.004.

Chase, B.M., and Brewer, S., 2009, Last Glacial Maximum dune activity in the Kalahari Desert of southern Africa: observations and simulations: Quaternary Science Reviews, v. 28, no. 3-4, p. 301–307, doi: 10.1016/j.quascirev.2008.10.008.

Clement, W.P., Wilkins, D.E., and Ford, R.L., 2006, Using Ground Penetrating Radar to Image Terrestrial Analogs of Martian Aeolian Deposition: The Coral Pink Sand Dunes, Kanab, Utah: EOS Transactions American Geophysical Union, v. 87, doi: 10.1029/2002JE002015.

Cooke, R., Warren, A., and Goudie, A., 1993, Desert geomorphology, UCL Press, London, p. 374-386.

Derickson, D., Kocurek, G., Ewing, R.C., and Bristow, C., 2008, Origin of a complex and spatially diverse dune-field pattern, Algodones, southeastern California: Geomorphology, v. 99, no. 1-4, p. 186–204, doi: 10.1016/j.geomorph.2007.10.016.

Ellwein, A.L., Mahan, S. A., and McFadden, L.D., 2011, New optically stimulated luminescence ages provide evidence of MIS3 and MIS2 eolian activity on Black Mesa, northeastern Arizona, USA: Quaternary Research, v. 75, no. 3, p. 395–398, doi: 10.1016/j.yqres.2010.12.002.

Ely, L.L., 1997, Response of extreme floods in the southwestern United States to climatic variations in the late Holocene: Geomorphology, v. 19, no. 3-4, p. 175–201, doi: 10.1016/S0169-555X(97)00014-7.

Ewing, R.C., Peyet, A., Kocurek, G., Mohrig, D., and Eastwood, E., 2008, Three-dimensional characterization and morphological dynamics of gypsum sand dunes at White Sands National Monument using airborne LiDAR: Planetary Dunes Workshop: A Record of Climate Change, Lunary and Planetary Institute, Houston, LPI contribution No.1403.

Ewing, R.C., 2009, Aeolian dune-field boundary conditions and interactions related to dune-field pattern formation on Earth and Mars: The University of Texas at Austin, Dissertation, p. 1-106.

Ewing, R.C., and Kocurek, G., 2010, Aeolian dune-field pattern boundary conditions: Geomorphology, v. 114, no. 3, p. 175–187, doi: 10.1016/j.geomorph.2009.06.015.

Feagin, R.A., Williams, A.M., Popescu, S., Stukey, J., and Washington-Allen, R.A., 2014, The use of terrestrial laser scanning (TLS) in dune ecosystems: The lessons learned: Journal of Coastal Research, v. 293, p. 111–119, doi: 10.2112/JCOASTRES-D-11-00223.1.

Ford, R.L., Gillman, S.L., Wilkins, D.E., Clement, W.P., and Nicoll, K., 2010, Geology and Geomorphology of Coral Pink Sand Dunes State Park, Utah, *in* Sprinkel, D.A., Chidsey Jr., T.C., and Anderson, P.B. eds., Geology of Utah's Parks and Monuments, Utah Geological Association, p. 379–406.

Ford, R.L., Wilkins, D.E., and Clement, W.P., 2001, Geomorphic and GPR evidence for structural influence on dunefield formation, Coral Pink sand dunes, Utah: Abstracts with Programs - Geological Society of America, v. 33.6, no. 437, p. 6–7.

Forman, S.L., Marín, L., Gomez, J., and Pierson, J., 2008, Late Quaternary eolian sand depositional record for southwestern Kansas: Landscape sensitivity to droughts: Palaeogeography, Palaeoclimatology, Palaeoecology, v. 265, no. 1-2, p. 107–120, doi: 10.1016/j.palaeo.2008.04.028.

Gregory, H.E., 1950, Geology and Geography of the Zion Park Region, Utah and Arizona: U. S. Geological Survey Professional Paper, v. 220, p. 1-207.

Grissino-Mayer, H.D., and Swetnam, T.W., 2000, Century-scale climate forcing of fire regimes in the American Southwest: The Holocene, v. 10, p. 213–220, doi: 10.1191/095968300668451235.

Harden, T., Macklin, M.G., and Baker, V.R., 2010, Holocene flood histories in south-western USA: Earth Surface Processes and Landforms, v. 716, no. April, p. 707-716, doi: 10.1002/esp.1983.

Harvey, J.E., Pederson, J.L., and Rittenour, T.M., 2011, Exploring relations between arroyo cycles and canyon paleoflood records in Buckskin Wash, Utah: Reconciling scientific paradigms: Geological Society of America Bulletin, v. 123, no. 11-12, p. 2266–2276, doi: 10.1130/B30374.1.

Havholm, K.G., Bergstrom, N.D., Jol, H.M., and Running, G.L., IV, 2003, GPR survey of a Holocene aeolian/fluvial/lacustrine succession, Lauder Sandhills, Manitoba, Canada, *in* Bristow, C.S. and Jol, H.M., eds., Ground Penetrating Radar in Sediments: Geological Society Special Publication 211, London, The Geological Society, p. 47-53.

Hayden, J.M., 2013, Geologic Map of the Yellowjacket Canyon Quadrangle, Kane County, Utah, and Mohave County, Arizona: Utah Geological Survey, Map 256DM, doi: 10.1029/2007JB005278.

Hayden, A., and Rittenour, T.M., 2011, Linking the Holocene fluvial history of the upper Escalante River, S. Utah to regional records using OSL and radiocarbon: Abstracts with Programs - Geological Society of America, v. 43, no. 4, p. 7.

Hereford, R., 2002, Valley-fill alluviation during the Little Ice Age (ca. AD 1400–1880), Paria River basin and southern Colorado Plateau, United States: Geological Society of America Bulletin, v. 114, no. 12, p. 1550–1563.

Hugenholtz, C.H., and Barchyn, T.E., 2010, Spatial analysis of sand dunes with a new global topographic dataset: new approaches and opportunities: Earth Surface Processes and Landforms, v. 35, no. 8, p. 986–992, doi: 10.1002/esp.2013.

Hugenholtz, C.H., Wolfe, S.A., and Moorman, B.J., 2008, Effects of sand supply on the morphodynamics and stratigraphy of active parabolic dunes, Bigstick Sand Hills, southwestern Saskatchewan, Geological Survey of Canada Contribution 20060654: Canadian Journal of Earth Sciences, v. 45, p. 321–335, doi: 10.1139/E08-001.

Jewell, P.W., and Nicoll, K., 2011, Wind regimes and aeolian transport in the Great Basin, U.S.A.: Geomorphology, v. 129, no. 1-2, p. 1–13, doi: 10.1016/j.geomorph.2011.01.005.

Jol, H.M. and Bristow, C.S., 2003, GPR in sediments: advice on data collection, basic processing and interpretation, a good practice guide, *in* Bristow, C.S. and Jol, H.M., eds., Ground Penetrating Radar in Sediments: Geological Society Special Publication 211, London, The Geological Society, p. 9-27.

Kocurek, G., 2003, Limits on extreme eolian systems: Sahara of Mauritania and Jurassic Navajo Sandstone examples, *in* Chan, M. A., and Archer, A. W., eds., Extreme depositional environments: Mega end members in geologic time: Geological Society of America Special Paper 370: Boulder, CO, Geological Society of America, p. 44-53.

Kocurek, G., Carr, M., Ewing, R., Havholm, K.G., Nagar, Y.C., and Singhvi, A.K., 2007, White Sands Dune Field, New Mexico: Age, dune dynamics and recent accumulations: Sedimentary Geology, v. 197, no. 3-4, p. 313–331, doi: 10.1016/j.sedgeo.2006.10.006.

Kocurek, G., and Ewing, R.C., 2005, Aeolian dune field self-organization – implications for the formation of simple versus complex dune-field patterns: Geomorphology, v. 72, no. 1-4, p. 94–105, doi: 10.1016/j.geomorph.2005.05.005.

Lancaster, N., 1995, Geomorphology of desert dunes: London, Routledge, 290 p.

Lancaster, N., and McCarley-Holder, G., 2013, Decadal-scale evolution of a small dune field: Keeler Dunes, California 1944–2010: Geomorphology, v. 180-181, p. 281–291, doi: 10.1016/j.geomorph.2012.10.017.

Lund, W. R., Knudsen, T. R., & Vice, G. S., 2008, Paleoseismic reconnaissance of the Sevier fault, Kane and Garfield Counties, Utah: Utah Geological Survey Special Study 122, 31 p.

Moller, I. and Anthony, D., 2003, GPR study of sedimentary structures within a transgressive coastal barrier along the Danish North Sea coast, *in* Bristow, C.S. and Jol, H.M., eds., Ground Penetrating Radar in Sediments: Geological Society Special Publication 211, London, The Geological Society, p. 55-65.

Montreuil, A. L., Bullard, J., & Chandler, J., 2013, Detecting seasonal variations in embryo dune morphology using a terrestrial laser scanner, *in* Proceedings 12th international coastal symposium (Plymouth, England), no. 65, p. 1313-1318, doi: 10.2112/SI65-222.1.

Nield, J.M., and Wiggs, G.F.S., 2011, The application of terrestrial laser scanning to aeolian saltation cloud measurement and its response to changing surface moisture: Earth Surface Processes and Landforms, v. 36, no. 2, p. 273–278, doi: 10.1002/esp.2102.

Nield, J.M., Wiggs, G.F.S., and Squirrell, R.S., 2011, Aeolian sand strip mobility and protodune development on a drying beach: examining surface moisture and surface roughness patterns measured by terrestrial laser scanning: Earth Surface Processes and Landforms, v. 36, no. 4, p. 513–522, doi: 10.1002/esp.2071.

Rango, A., Chopping, M., Ritchie, J., Havstad, K., and Kustas, W., 2000, Morphological characteristics of shrub coppice dunes in desert grasslands of southern New Mexico derived from scanning LIDAR: v. 44, no. January, p. 26–44.

Reiss, S., Reicherter, K.R., and Reuther, C.-D., 2003, Visualization and characterization of active normal faults and associated sediments by high-resolution GPR, *in* Bristow, C.S. and Jol, H.M., eds., Ground Penetrating Radar in Sediments: Geological Society Special Publication 211, London, The Geological Society, p. 247-255.

Salzer, M.W., and Kipfmueller, K.F., 2005, Reconstructed temperature and precipitation on a millennial timescale from tree-rings in the southern Colorado Plateau, U.S.A.: Climatic Change, v. 70, p. 465–487, doi: 10.1007/s10584-005-5922-3.

Saye, S.E., van der Wal, D., Pye, K., and Blott, S.J., 2005, Beach-dune morphological relationships and erosion/accretion: An investigation at five sites in England and Wales using LIDAR data: Geomorphology, v. 72, p. 128–155, doi: 10.1016/j.geomorph.2005.05.007.

Stockdon, H.F., Doran, K.S., and Sallenger, A.H., 2009, Extraction of lidar-based dune-crest elevations for use in examining the vulnerability of beaches to inundation during hurricanes: Journal of Coastal Research, Special Issue no. 53, p. 59–65, doi: 10.2112/SI53-007.1.

Summa-Nelson, M.C., and Rittenour, T.M., 2011, Investigating arroyo cut-fill cycles and their link to Holocene climate change along Kanab Creek, southern Utah: Abstracts with Programs - Geological Society of America, v. 43, no. 4.

Thomas, D.S.G., 2013, Reconstructing paleoenvironments and palaeoclimates in drylands: what can landform analysis contribute? Earth Surface Processes and Landforms, v. 38, no. 1, p. 3–16, doi: 10.1002/esp.3190.

Thomas, D.S.G., and Wiggs, G.F.S., 2008, Aeolian system responses to global change : challenges of scale, process and temporal integration: Earth Surface Processes and Landforms, v. 33, p. 1396–1418, doi: 10.1002/esp.

Wannamaker, P. E., Bartley, J. M., Sheehan, A. F., Jones, C. H., Lowry, A. R., Dumitru, T. A., . . . Wolfe, J. A., 2001, Great Basin-Colorado Plateau transition in central Utah: An interface between active extension and stable interior, 38 p.

Werner, B.T., 1995, Eolian dunes: Computer simulations and attractor interpretation: Geology, v. 23, no. 12, p. 1107–1110.

Werner, B.T., and Kocurek, G., 1999, Bedform spacing from defect dynamics: Geology, v. 27, no. 8, p. 727–730.

Wilkins, D.E., and Ford, R.L., 2007, Nearest neighbor methods applied to dune field organization: The Coral Pink Sand Dunes, Kane County, Utah, USA: Geomorphology, v. 83, no. 1-2, p. 48–57.

Wilkins, D., Ford, R.L., and Clement, W., 2003, GPR and GIS use in documenting a distinctive mode of star dune development: Congress of the International Union for Quaternary Research, no. 85.

Wilkins, D.E., Ford, R.L., Clement, W.P., and Nicoll, K., 2005, Little Ice Age behavior of the Coral Pink Sand Dunes, Kane County, Utah: Geological Society of America 2005 Annual Meeting Abstracts with Program, v. 37, p. 426.

Wolfe, S.A., and Hugenholtz, C.H., 2009, Barchan dunes stabilized under recent climate warming on the northern Great Plains: Geology, v. 37, no. 11, p. 1039–1042, doi: 10.1130/G30334A.1.

Woolard, J.W., and Colby, J.D., 2002, Spatial characterization, resolution, and volumetric change of coastal dunes using airborne LIDAR: Cape Hatteras, North Carolina: Geomorphology, v. 48, p. 269–287, doi: 10.1016/S0169-555X(02)00185-X.

Wright, D.K., Forman, S.L., Waters, M.R., and Ravesloot, J.C., 2011, Holocene eolian activation as a proxy for broad-scale landscape change on the Gila River Indian Community, Arizona: Quaternary Research, v. 76, no. 1, p. 10–21, doi: 10.1016/j.yqres.2011.04.008.

Yang, X., Scuderi, L., Liu, T., Paillou, P., Li, H., Dong, J., Zhu, B., Jiang, W., Jochems, A., and Weissmann, G., 2011, Formation of the highest sand dunes on Earth: Geomorphology, v. 135, no. 1-2, p. 108–116, doi: 10.1016/j.geomorph.2011.08.008.